Development of an integrated experimental and numerical methodology for the performance analysis of multiple hybrid electric architectures over different driving cycles



Doctoral Dissertation
Doctoral Program in Energy Engineering (33rd Cycle)

# Development of an integrated experimental and numerical methodology for the performance analysis of multiple hybrid electric architectures over different driving cycles

**Giuseppe Di Pierro**
* * * * * *

**Supervisor**
Prof. Federico Millo

**Doctoral Examination Committee:**
Prof. A.B. , Referee, University of….
Prof. C.D. , Referee, University of…
Prof. E.F. , Referee, University of….
Prof. G.H. , Referee, University of…
Prof. I.J. , Referee, University of….

Politecnico di Torino
April 30, 2020

I hereby declare that, the contents and organization of this dissertation constitute my own original work and does not compromise in any way the rights of third parties, including those relating to the security of personal data.

.....

Giuseppe Di Pierro

Turin, April 30, 2020

# Summary

In response to rising concerns about road transportation and its climate impacts, the electrification of modern powertrains plays a crucial role as a key measure to reduce pollutant and greenhouse gas emissions. Worldwide governments are conveying their efforts in the run for a sustainable transportation system that is required to be as much as clean and efficient as possible under various driving conditions. Hence, the so-called real-world emissions are under the microscope, since they are measured outside of a controlled testing environment. In this scenario, the fast pace of innovation along with the increasing complexity represents a new challenge for OEMs. Therefore, development and validation of these new powertrain concepts is receiving more and more importance.

In this regard, a research activity has been carried out in collaboration between Politecnico di Torino and FEV Italia, within their facilities in Piedmont, Italy. The aim of this collaboration is to provide a "virtual test rig" capable to evaluate the performance of various electrified powertrains over a wide range of different real driving scenarios. The proposed integrated and standardized methodology wants to bridge the gap between testing and modelling of hybrid electric vehicles (HEVs), reducing the testing effort in terms of time and cost. The experimental campaign relies on a limited set of dedicated tests: standstill starts, accelerations, constant speed driving and different type of decelerations; carried out to collect data for the reverse engineering of the powertrain and for vehicle simulation. Most important, components characterization is based on a customized and non-invasive powertrain instrumentation.

On the simulation side, a comprehensive 0D map-based model was developed and calibrated according to the aforementioned test campaign, with particular

focus on the Energy Management System (EMS) reverse engineering. The simulation platform is able to simulate several hybrid architectures with high flexibility, also in real driving scenarios. The methodology was applied to 3 different electrified vehicles available on the market, with increasing complexity order, such as a 48V mild-hybrid (MHEV) Diesel P0 architecture, a P0-P2 gasoline Plug-in hybrid (PHEV) architecture and a P2 Diesel PHEV architecture.

As a result, the virtual test rig is used to evaluate the energy split, $CO_2$ emissions and fuel consumption on different driving cycles and Real Driving Emissions (RDE) tests, allowing the universal vehicle model to be adopted in the predevelopment phase of new powertrains.

# Acknowledgment

Firstly, I would like to express my sincere gratitude to my advisor Prof. Federico Millo for the continuous support, for his motivation, and immense knowledge. Besides my advisor, I would like to thank FEV Italy for sponsoring my PhD scholarship; my sincere thanks goes to Dr. Fabio Mallamo, Ing. Alessandro Perazzo and Ing. Mauro Scassa and all my co-workers of the FEV testing, benchmarking and simulation teams for their valuable advice and assistance.

I wish to thank the JRC's Sustainable Transport Unit for the close collaboration and expertise shared throughout the different research activities carried out either in FEV and JRC's facilities.

Finally, my gratitude goes to my fellow lab-mates, the entire e3 research group for helping and inspiring me along the PhD journey.

*To my family and my soul mate*

*For their relentless love and support*

# Contents


1. Introduction ..... 1

1.1 Regulation Framework ..... 1
1.2 The European Automotive Market ..... 3
1.3 The Experimental and Numerical Approach ..... 7

2. The Integrated Methodology ..... 9

2.1 HEV testing: a complex picture ..... 10
2.2 Case study ..... 11

2.2.1 Vehicle 1 Test Case ..... 11
2.2.2 Vehicle 2 Test Case ..... 13
2.2.3 Vehicle 3 Test Case ..... 15

2.3 Vehicle Instrumentation: a non-invasive approach ..... 17

2.3.1 Electrical side instrumentation ..... 19
2.3.2 Additional instrumentation ..... 23

2.4 Test Procedure ..... 28

2.4.1 Standard Driving Cycles ..... 29
2.4.2 Characterization Tests ..... 33

2.5 Analysis of the Experimental Campaign ..... 37

2.5.1 Vehicle 1 Analysis ..... 37
2.5.2 Vehicle 2 Analysis ..... 43
2.5.3 Vehicle 3 Analysis ..... 53

3. The Comprehensive xEV Model ..... 63

3.1 The Model-based Approach ..... 64
3.2 The comprehensive model ..... 65

3.2.1 Vehicle model ..... 67

3.2.2 Driver model ..... 68
3.2.3 Engine model ..... 70
3.2.4 Transmission Model ..... 71
3.2.5 E-motor model ..... 72
3.2.6 HV Battery model ..... 75
3.2.7 Hybrid Control Unit model ..... 81

4. Results and Discussion ..... 94

4.1 Driving Cycle Simulation ..... 95

4.1.1 Vehicle 1 Simulation ..... 95
4.1.2 Vehicle 2 Simulation ..... 98
4.1.3 Vehicle 3 Simulation ..... 101

4.2 Model Validation ..... 110

4.2.1 Charge Sustaining WLTC ..... 110
4.2.2 Real Driving Emissions Cycle ..... 111

5. Conclusions ..... 116
6. References ..... 119

# List of Tables

Table 1: $CO_2$ emissions reduction comparison between hybrids and BEVs from [32] ..... 5
Table 2: Vehicle 1 - Vehicle and powertrain main specifications ..... 13
Table 3: Vehicle 2 - Vehicle and powertrain main specifications ..... 15
Table 4: Vehicle 3 - Vehicle and powertrain main specifications ..... 17
Table 5: Vehicle Road Loads and Test Mass ..... 29
Table 6: Summary of the characteristics of NEDC and WLTC class 3b ..... 31
Table 7: RDE Characteristic for Vehicle 3 ..... 33
Table 8: Performance tests: standing-start and elasticity operating conditions ..... 34
Table 9: Critical Missions: operating conditions ..... 36
Table 10: Modified Coulomb Counting Method coefficients ..... 54

# List of Figures

Figure 1: Historical average CO2 emission values, targets, and annual reduction rates of new passenger cars in the European Union [8] ..... 2
Figure 2: Global passenger car $CO_2$ emissions and fuel consumption, normalized to NEDC [12] ..... 2
Figure 3: Passenger cars market share in EU, for Diesel (left) and HEV (right), until 2018 [26] ..... 3
Figure 4: Passenger cars market share in EU, for PHEV (left) and BEV (right), from 2012 [26] ..... 3
Figure 5: Development of drive systems (EU28 New car sales 2017–2030) – PWC [28] ..... 4
Figure 6: Volume scenarios for electrified drives in different global regions – Schaeffler [29] ..... 5
Figure 7: Different hybrid architectures and their functionalities (top) and possible combination of architecture, topology, and transmission (bottom) [29] ... 7
Figure 8: Workflow of the presented methodology ..... 8
Figure 9: Vehicle 1 - Powertrain Layout ..... 12
Figure 10: Vehicle 2- EV Mode ..... 14
Figure 11: Vehicle 2- Load Point Shift/Torque Assist (left) and Series, HEV Mode ..... 14
Figure 12: Vehicle 3- Load Point Shift/Torque Assist, HEV Mode ..... 16
Figure 13: Vehicle 3- EV Mode ..... 16
Figure 14: Schematic of Vehicle Installation (left) [49] and real top view (right) on a Chassis-Dynamometer ..... 18
Figure 15: Schematic of Emissions-Measurement Dilution System[51] ..... 19
Figure 16: Shunt installation on the DC/DC HV side ..... 20
Figure 17: Vehicle 1 - Powertrain layout with instrumentation details ..... 22
Figure 18: Vehicle 2 - Powertrain layout with instrumentation details ..... 22

Figure 19: Vehicle 3 - Powertrain layout with instrumentation details .....23
Figure 20: Engine Main cooling circuit – layout and instrumentation .....24
Figure 21: HV system cooling circuit – layout and instrumentation .....24
Figure 22: Thermocouples for measurement of the HV Battery Surface Temperature (left) and Engine coolant radiator inlet/outlet .....25
Figure 23: SAE J1962 Vehicle Connector, Type A schematic [58] (left) and on a car[59] .....25
Figure 24: CAN logging from different Control Modules (CM) .....26
Figure 25: On-board Measurement Chain via ETAS Inca [64] .....27
Figure 26: Example of vehicle instrumentation and dyno installation.....28
Figure 27: NEDC (top) and WLTC Class 3b (bottom) speed profile .....32
Figure 28: FEV RDE Route definition (top) and speed/altitude profile (bottom): phase 1 (urban) blue, phase 2 (rural) green and phase 3 (highway) purple .....33
Figure 29: Performance Tests - Standing-start 0-100 km/h for low (a) and high (b) battery initial SOC; Elasticity test 80-120 km/h maneuver for high SOC and high power request (c), mid SOC and low power request (d) [76]. .....35
Figure 30: Critical Mission tests: (a) Steady-State driving, (b) Active Braking and (c) Sailing [78] .....37
Figure 31. Measurements for 0 – 100km/h performance test at low SOC (top) high SOC (bottom).....39
Figure 32. 2nd gear elasticity test measurements at high SOC for high power requests (top) and low SOC for low power requests (bottom) .....40
Figure 33. 6th gear elasticity test measurements at high SOC for high power requests (top) and high SOC for low power requests (bottom) .....41
Figure 34: Steady State driving on the chassis dyno at different vehicle speeds .....42
Figure 35: BSG (left) and 48V Battery (right) operating points recorded during testing .....43
Figure 36: ICE and BSG full load torque (left) and power (right) for Vehicle 1 .....43
Figure 37. Main measurements for 0–100km/h test at 50% (left) and 100% (right) accelerator pedal, in EV Mode (solid line) and Hybrid Mode (dashed line) .....45
Figure 38. Main measurements for 40–80km/h Elasticity test in EV Mode (left) and 60–100km/h Elasticity test in Hybrid Mode at low SOC (right), at 100% accelerator (solid line) and 50% accelerator (dashed line) .....46

Figure 39. Main measurements for 30km/h (left) and 120km/h (right) Steady State driving in Hybrid Mode ..... 48
Figure 40. Main measurements for Active Braking from 100km/h, in EV Mode (solid line) and Hybrid Mode (dashed line) ..... 49
Figure 41. EM and ICE measurements for Active Braking from 120km/h, at 50% brake (solid line) and 75% brake (dashed line) ..... 49
Figure 42: EM and ICE measurements for 50-30km/h Sailing test in EV mode (solid line) and Hybrid mode (dashed line) ..... 50
Figure 43: EM and ICE measurements for 100-80km/h Sailing test at high SOC, in Hybrid Mode (solid line) and EV Mode (dashed line) ..... 50
Figure 44: P2 EM (left) and HV Battery (right) operating points recorded during testing ..... 51
Figure 45: Hybrid Mode activation map: threshold vehicle speed function of torque at wheels (a) and battery SOC (b) ..... 52
Figure 46: Driving Mode split operating points as a function of vehicle speed (left) or speed times acceleration (right) and torque requested at the wheels..... 52
Figure 47: ICE Power generated versus vehicle speed during Load Point Shift in Hybrid Mode, for each gear: battery charging (top) and boosting (bottom) ..... 53
Figure 48: Modified Coulomb Counting Method application for HV Battery SOC estimation over three NEDC cycles ..... 54
Figure 49: NEDC TA procedure simulation: HV Battery energy and voltage and vehicle speed (top) and driving mode split (bottom) ..... 55
Figure 50.Main measurements for 40–80km/h kick-down Elasticity test in EV Mode ..... 56
Figure 51: Powertrain torque (top), speed and gear (central ) and vehicle speed with accelerator pedal position (bottom) during a constant driving test ..... 57
Figure 52: Hybrid Mode switch characterization by constant speed driving.. 57
Figure 53: Main signals recorded during active braking test ..... 58
Figure 54: Brake blending ratio: regenerative (PWT) over total braking power ..... 59
Figure 55. P2 EM (left) and HV Battery (right) operating points recorded during testing ..... 60
Figure 56: Hybrid Mode Request: threshold vehicle speed function of torque at wheels and battery SOC (left) and threshold power at the wheels function of speed times acceleration and battery SOC (right) ..... 60
Figure 57: Driving Mode split operating points as a function of vehicle speed (left) or speed times acceleration (right) and torque requested at the wheels..... 61

Figure 58: EM absorbed toque (top) and ICE generated torque (bottom) versus torque requested at the wheels during Load Point Shift operations in Hybrid Mode ..... 62
Figure 59: Time to market evolution for engine project[83] ..... 64
Figure 60. Hybrid architecture nomenclature based on electric machine position for different parallel hybrid configurations [91] ..... 66
Figure 61. Simulation model top layer ..... 66
Figure 62: Vehicle model main layer ..... 67
Figure 63: Driver model main layer ..... 69
Figure 64: Engine physical model top layer ..... 71
Figure 65: Physical transmission model ..... 72
Figure 66: Motor physical model ..... 73
Figure 67: Efficiency maps for BSG (top-left), HSG (top-right) and Ems (bottom) of the three test cases ..... 75
Figure 68: E-motor speed calculation ..... 75
Figure 69: Open circuit voltage and internal resistance sub-system ..... 76
Figure 70: Battery equivalent model ..... 77
Figure 71: Battery model output voltage correlation before (left) and after (right) maps correction ..... 78
Figure 72: HV battery cell OCV for LTO (left), LiPo (center) and Li-NMC (right) technology ..... 78
Figure 73: HV battery cell internal resistance for LiPo (left) and Li-NMC in charge (center) and discharge (right) ..... 79
Figure 74: HV battery SOC calculation ..... 79
Figure 75: HV battery power limit maps during discharge (top) and charge (bottom), both in Continuous (left) and Peak (right) operations ..... 81
Figure 76: HCU model - layout switch ..... 82
Figure 77: Hybrid control unit schematic representation ..... 83
Figure 78: Driving Mode Selection block ..... 83
Figure 79: Torque Manager State – Hybrid mode decompositions ..... 84
Figure 80: Torque Manager State – Extended Hybrid Mode decomposition ..... 85
Figure 81: Parallel hybrid operating mode decomposition ..... 86
Figure 82: P0 hybrid operating mode decomposition ..... 88
Figure 83: BSG Drive torque calculation ..... 89
Figure 84: Rules for the hybrid mode request ..... 91
Figure 85: Rules for the E-drive request ..... 92
Figure 86: Vehicle 2 E-Drive or Parallel input layer ..... 93
Figure 87: Vehicle 3 ICE charge torque request layer ..... 93

Figure 88: Vehicle1 $CO_2$ flow rate [g/s] calibrated map and WLTC ICE operating points (black) ..... 96
Figure 89: Vehicle 1 - Experimental (black dashed) and simulated (red solid) power at the clutch (left), $CO_2$ flow rate (right) with vehicle speed profile (top dotted) over the four WLTC phases ..... 97
Figure 90: Vehicle 1 - Experimental (black dashed) and simulated (red solid) power at the clutch (left), $CO_2$ flow rate (right) with vehicle speed profile (top dotted) over the urban (top) and extra-urban (bottom) NEDC phases ..... 98
Figure 91: Vehicle 1 - WLTC (left) and NEDC (right) experimental (black dashed) and simulated (red solid) cumulated $CO_2$ emissions ..... 98
Figure 92: Vehicle 2 - Experimental (black dashed) and simulated (red solid) results over the mid-SOC NEDC ..... 100
Figure 93: Vehicle 3 - Experimental (black dashed) and simulated (red solid) results over the NEDC Charge Depleting CD ..... 104
Figure 94: Vehicle 3 - Experimental (black dashed) and simulated (red solid) results over the WLTC Charge Depleting CD ..... 105
Figure 95: Vehicle 3 - Experimental (black dashed) and simulated (red solid) results over the NEDC Charge Sustaining CS ..... 106
Figure 96: Vehicle 3 - Experimental (black dashed) and simulated (red solid) results over the WLTC Charge Sustaining CS ..... 107
Figure 97: Vehicle 3 $CO_2$ flow rate [g/s] calibrated cold (left) and hot (right) maps and WLTC ICE operating points (black) ..... 108
Figure 98: Vehicle 3 ICE block and coolant temperature profile along the NEDC (left) and WLTC (right) CS cycle ..... 109
Figure 99: Vehicle 3 instantaneous and cumulated CO2 emissions over the NEDC (top) and WLTC (bottom) cycles ..... 109
Figure 100: Vehicle 2 - Experimental (black dashed) and simulated (red solid) results over the WLTC Charge Sustaining CS ..... 111
Figure 101: Vehicle 3 - Experimental (black dashed) and simulated (red solid) results over the first part of RDE ..... 113
Figure 102: Vehicle 3 - Experimental (black dashed) and simulated (red solid) results over the second part of RDE ..... 114
Figure 103: Vehicle 3 instantaneous and cumulated CO2 emissions over the RDE cycle ..... 115

# Acronyms

| | |
|---|---|
| **4WD** | Four-Wheel Drive |
| **A/C** | Air Conditioning |
| **AC** | Alternate Current |
| **ADMM** | Analogue-Digital MiniModule |
| **AT** | Automatic Transmission |
| **BEV** | Battery Electric Vehicle |
| **BMEP** | Brake Mean Effective Pressure |
| **BSG** | Belt Starter Generator |
| **CAN** | Controller Area Network |
| **CD** | Charge Depleting |
| **CFD** | Computational Fluid Dynamics |
| **CFV** | Constant Flow Venturi |
| **CI** | Compression Ignition |
| **CS** | Charge Sustaining |
| **CVS** | Constant Volume Sample |
| **DC** | Direct Current |
| **DCT** | Dual Clutch Transmission |
| **EC** | European Commission |
| **ECM** | Engine Control Module |
| **EM** | Electric Motor |

| | |
|---|---|
| **EMS** | Energy Management System |
| **EU** | European Union |
| **EUDC** | Extra Urban Driving Cycle |
| **EV** | Electric Vehicle |
| **FCA** | Fiat Chrysler Automotive |
| **FWD** | Front-Wheel Drive |
| **HCU** | Hybrid Control Unit |
| **HEV** | Hybrid Electric Vehicle |
| **HPCU** | Hybrid Power Control Unit |
| **HSG** | Hybrid Starter Generator |
| **HV** | High Voltage |
| **HVAC** | Heating, Ventilation and Air Conditioning |
| **I/O** | Input/output |
| **ICE** | Internal Combustion Engine |
| **IPM** | Internally mounted Permanent Magnet |
| **JLR** | Jaguar Land Rover |
| **JRC** | Joint Research Center |
| **LiPo** | Lithium Polymer |
| **LPS** | Load Point Shift |
| **LTO** | Lithium Titanate Oxide |
| **LV** | Low Voltage |
| **MHEV** | Mild Hybrid Electric Vehicle |
| **MT** | Manual Transmission |
| **NA** | Naturally Aspirated |
| **NEDC** | New European Driving Cycle |
| **NMC** | Nickel-Manganese-Cobalt |
| **NOVC** | Non Off-Vehicle Charging |
| **OBD** | On-Board Diagnostic |
| **OCV** | Open Circuit Voltage |
| **OEM** | Original Equipment Manufacturer |
| **OVC** | Off-Vehicle Charging |

| | |
|---|---|
| **PHEV** | Plug-in Hybrid Electric Vehicle |
| **PM** | Particulate Matter |
| **PMSM** | Permanent Magnet Synchronous Motor |
| **PN** | Particulate Number |
| **PSA** | Peugeot Société Anonyme |
| **PTC** | Positive Temperature Coefficient |
| **PWC** | Price Water Corporation |
| **RDE** | Real Driving Emissions |
| **RL** | Road Load |
| **RMSE** | Root Mean Square Error |
| **RWD** | Rear-Wheel Drive |
| **SOC** | State of Charge |
| **TA** | Type Approval |
| **TCM** | Transmission Control Module |
| **THMM** | Thermo MiniModule |
| **TTW** | Tank-to-Wheel |
| **UDC** | Urban Driving Cycle |
| **UN** | United Nations |
| **VW** | Volkswagen |
| **WLTC** | Worldwide Harmonized Light-duty Test Procedure |

# Chapter 1

# Introduction

## 1.1 Regulation Framework

Climate change is one of the most severely argued scientific issues of the past 20 years. It involves many dimensions and it is believed that transport decarbonization could play a key role in this topic. The transportation sector accounts for 23% of energy-related $CO_2$ emissions; which has led to increasing policy pressure, especially for passenger cars [1]. Currently, one billion cars are driven on the road worldwide, frequently powered by an Internal Combustion Engine (ICE) [2]. By 2050, the urban passenger transport demand could grow 60-70%, causing a 26% increase in $CO_2$ emissions [3]. The fact that transport still heavily relies on fossil fuels has pushed the European Union (EU) to foster relevant policies and incentive schemes for the transition to electro-mobility [4]. In 2015, the European Commission (EC) adopted the Energy Union Package (COM(2015)80), indirectly imposing a certain electrification degree of car fleet and other means of transport [5]. For 2030, new $CO_2$ targets from the EC would require Original Equipment Manufacturers (OEMs) to decrease average emissions by 37.5% from 2021 levels [6]. Moreover, the EU requires 15% of all sales to be either plug-in hybrid or electric (less than 50g/km of $CO_2$) by 2025 and 30% by 2030. "*The framework aims to support a gradual transition from vehicles powered by conventional engines to electric vehicles*", the EC stated in November 2018 [7].

Over the last two decades, significant improvement have been made in $CO_2$ reduction of passenger cars: Figure 1 shows the history of European average $CO_2$ values relative to targets. Since the first $CO_2$ standards introduction in 2008, OEMs successfully outperformed the annual reduction rates until 2015, with an average 3.5% per-year decline. After 2015, an average increase of 0.3% per year in $CO_2$ emissions has been reported; hence, from 2018 to 2021, a fleet-average $CO_2$ emissions decline of about 7.6% per year is required [8,9].

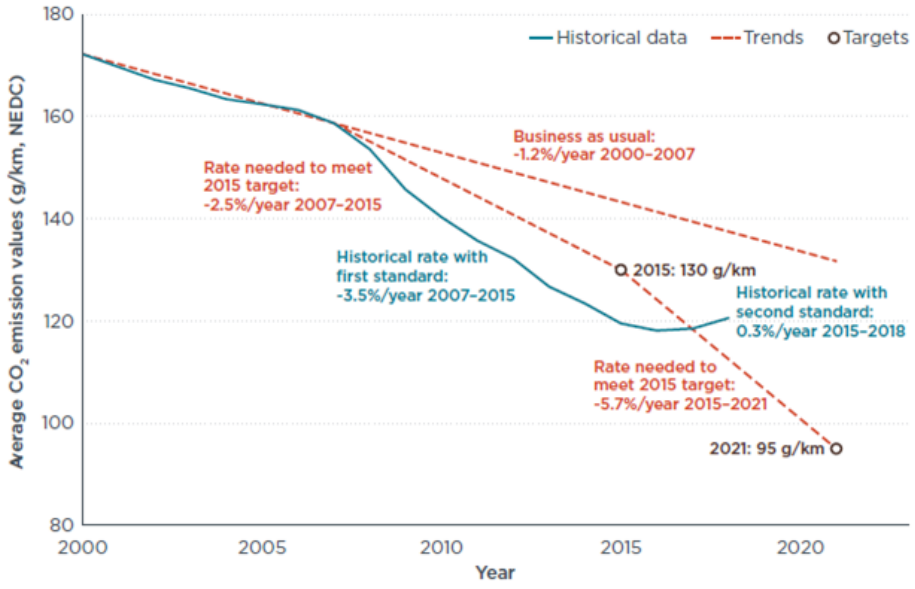


**Figure 1: Historical average CO2 emission values, targets, and annual reduction rates of new passenger cars in the European Union** [8]

On a worldwide scale too, government have introduced regulations with more stringent emission standards, more demanding in terms of fuel consumption and $CO_2$ emission reduction [10]. Figure 2 compares the $CO_2$ passenger car standards of similar regulations around the globe, normalized to the NEDC test cycle. For the principal markets, a great technological effort is foreseen to annually improve fuel economy by 3–6% [11].

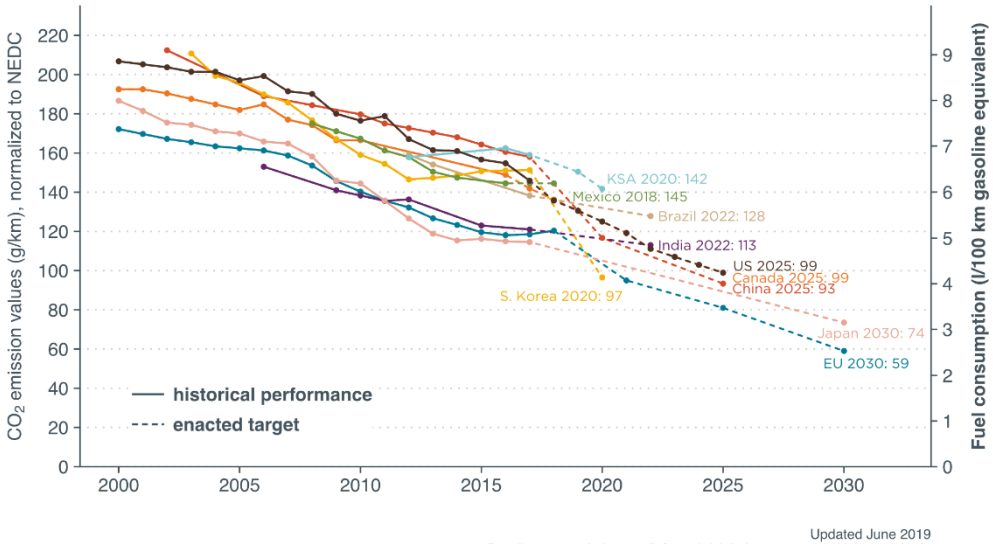


**Figure 2: Global passenger car $CO_2$ emissions and fuel consumption, normalized to NEDC** [12]

As a result, a cleaner and more efficient transport sector is necessary [13–17]. Thus, the major challenge for the ICE-based automotive engineering will focus on maximizing engine efficiency, minimize pollutant emissions, and develop new technologies able to exploit different fuels in transportation systems and power generation as well [18].

## 1.2 The European Automotive Market

In this framework, OEMs have addressed powertrain electrification as an enabler for a substantial emission reduction; however, the electrification process does not only include Battery Electric Vehicles (BEVs), but also ICE-based vehicles such as mild hybrids (MHEVs) [19], full hybrids (HEVs), and plug-in hybrids (PHEVs) [20–23]. Clearly, electrified vehicles play a relevant role in the future of automotive [24]. The recent industry of the automotive field shows a deep plunge of Diesel market share in EU, from 52% in 2008 to 36% in 2018; this is especially true after the '*Dieselgate*' happened in 2015. In this regard, the left plot of Figure 3 shows the diesel share by member state and total EU-28 from 2001 to 2018. On the other side, the total market share of HEVs was 3 % in 2018, after a continuous growth over the last decade. Finland, Ireland, Spain and Sweden give the main contribution to HEV share, as depicted in the right plot of Figure 3. The left side of Figure 4 reports the history of PHEVs share, as of 2012; Sweden has shown a significant growth in sales. As for BEVs, the Netherlands have the highest market share, as shown in the right side of Figure 4. In 2018, PHEVs and BEVs made up about 3 % of new sales in the EU. As a reference, a study [25] shows that a company as BMW will need a market share of about 13 % of PHEV and BEV to meet the 2021 $CO_2$ targets.

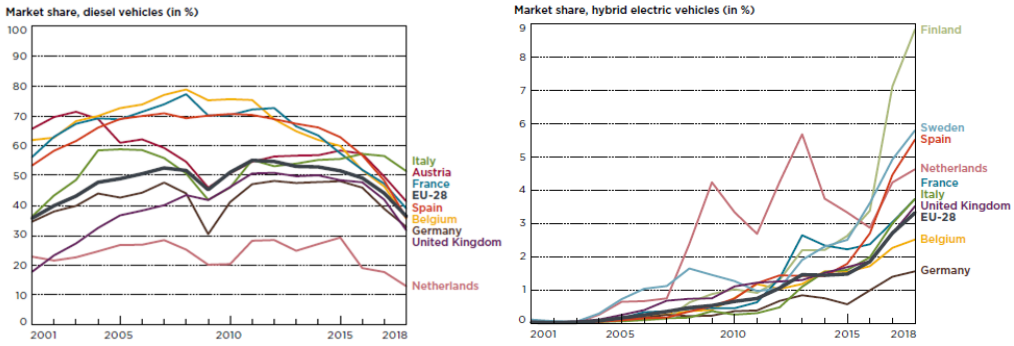


**Figure 3: Passenger cars market share in EU, for Diesel (left) and HEV (right), until 2018** [26]

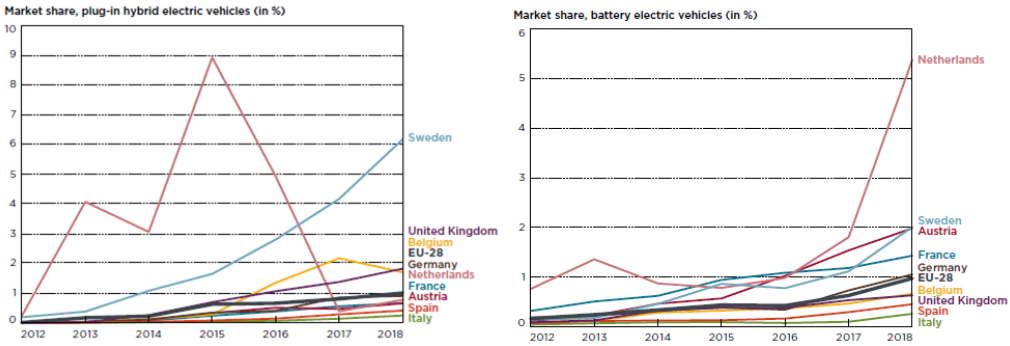


**Figure 4: Passenger cars market share in EU, for PHEV (left) and BEV (right), from 2012** [26]

In line with the EU increasing pressure, *"OEMs are transforming their lineups as they push to launch full-electric and plug-in hybrid cars in the next few*

*years. Automakers looking for positive publicity have made bold promises to electrify their global fleets in the midterm"* [27] reports the Automotive News Europe newspaper; hereafter some statements are listed:

- By 2023, 86 % of all **PSA** Group's models will have an electric or plug-in option;
- By the end of 2022, **FCA** will have launched more than 30 nameplates with electric drivetrains;
- Starting in 2019, every all-new **Volvo** launched will have some form of electrification;
- **Renault** plans to launch eight BEVs and 12 electrified models by 2022;
- The **VW** Group has announced it will launch 25 BEVs by 2020 and plans to sell up to 3 million EVs annually by 2025;
- By 2022, **Ford** will have 16 dedicated BEVs globally;
- Also by 2022, **Daimler** will electrify the entire range of Mercedes cars;
- Every new **JLR** vehicle will be electrified by 2020;
- One-third of all **Maserati** will be electrified by the mid-2020s;

In this scenario, a study from PWC [28] reports that over 95% of the EU new car sales are expected to be partially electrified in 2030. Conventional vehicles share in Europe could drop to less than 5%, while more than 40% of all new car sales would be hybrid, gaining more and more consensus over time, as illustrated in Figure 5.

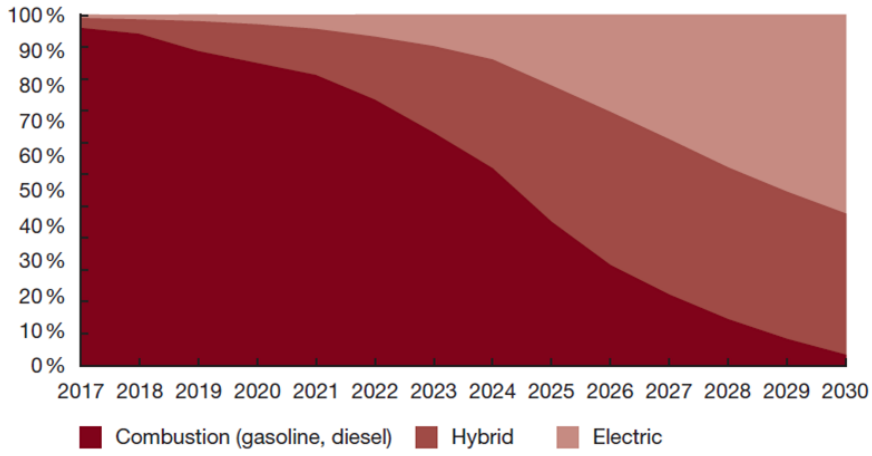


**Figure 5: Development of drive systems (EU28 New car sales 2017–2030) – PWC** [28]

As mentioned earlier, regulation is the main driver rather that the market demand. However, legislation vary substantially across the globe. Figure 6 depicts the automotive market mix forecast for 2020 and 2025, for various regions; by Schaeffler. China and Europe show a similar trends, since fleet emissions are targeted, MHEV (48V) technology is expected to grow in volume. On the other side, Japan and the USA will see the full hybrid (HEV) as the dominant solution, due to the fact that the High Voltage (HV) technology is already well known and vehicle mass [29].

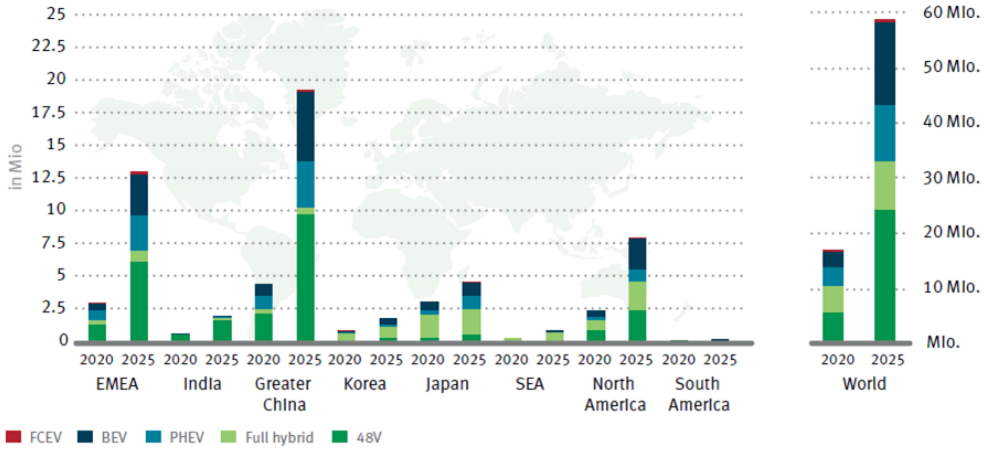


**Figure 6: Volume scenarios for electrified drives in different global regions – Schaeffler** [29]

Unfortunately, every gram of saved $CO_2$ has to be evaluated in terms of costs and time consumed. Nowadays, the general belief is that BEV will ease the automotive struggles as rapidly as possible, however, the scientific community must evaluate whether a full-electric scenario is better than a combined strategy that involves variety of HEVs. Also PHEVs are gaining consensus [30], since they can travel like a BEV in Charge Depleting (CD) mode or like a full HEV, turning the ICE on during Charge Sustaining (CS) mode [31].

Emissions Analytics [32] has published a study based on 95 hybrid vehicles, with an average battery of 1.2 kW ,resulting in a 30% $CO_2$ emissions reduction in comparison with current ICE vehicles. Considering the EU 37.5% $CO_2$ reduction target imposed for post-2021 for passenger cars, current hybrids could account for 75% of that. Fortunately, further development is expected from OEMs [33] For the 95 tested vehicles, the overall $CO_2$ reduction per unit battery size is shown in Table 1. The nearest equivalent ICE-only vehicle is used as term of comparison. This is a so-called Tank-to-Wheel (TTW) analysis that neglects any $CO_2$ emissions related with the battery, electricity and fuel production, which is likely to further support the HEV case. As reported in the table, MHEVs and HEVs provide considerably higher $CO_2$ benefit per unit battery size compared to PHEVs and BEVs. As demonstrated, the extremely large batteries make the BEVs have the lowest efficiency.

**Table 1: $CO_2$ emissions reduction comparison between hybrids and BEVs from** [32]

| Vehicle Type | Average $CO_2$ reduction (g/km) | $CO_2$ reduction per unit battery size (g/km/kWh) |
|---|---|---|
| MHEV | 25 | 73.9 |
| HEV | 65 | 50.5 |
| PHEV | 126 | 12.0 |
| BEV | 210 | 3.5 |

As previously mentioned, hybridization comes under different forms. Powertrains can be classified on the basis of the architecture, topology and functionalities. Nowadays, the degree of hybridization is a very well-known concept (micro, mild, full, and plug-in hybrids, pure electric), and can be categorized based on the possible capabilities. The various architectures, such as parallel, serial, and power-split can be differentiated on the basis of the energy flow. On top of that, if there is a sufficient amount of electrical power is sufficient, the transmission structure is simpler, hence more cost-effective [34]. In addition, combining dedicated transmissions with tailored designs of the combustion engine and electric drives, can result in further benefit in terms of consumption and emissions [35,36].

As for electrified vehicles, the parallel structures can differ according to the position of the electric machine, along the driveline. The top part of Figure 7 shows the possible ways of integrating the electric motor in the powertrain. All architectures allows the basic functions of regenerative braking and boosting, as well as sailing when the ICE is decoupled. However, the P0 and P1 layouts require the ICE to be linked to the crankshaft, while from the P2 onwards, energy recovery and pure electric driving can be performed with the ICE off. Finally, the P4 and P5 architectures offer four-wheel drive (4WD). It can be seen in the bottom part of Figure 7 that the combination of different voltage network and topology results in a total of 16 options. Moreover, the complexity increases sharply if different transmission solutions are considered [29].

To sum up, hybrid vehicles are quite complex electro-mechanical-chemical systems. The adoption of high electric power, high battery energy content and numerous topologies triggers the development of dedicated energy management strategies (EMS) to control the power distribution, optimize drivetrain efficiency and reduce fuel consumption and pollutants emissions [37,38]. Over the last decades, the development of EMSs has gained a lot of attention as one of the key research topics on HEVs [39,40].

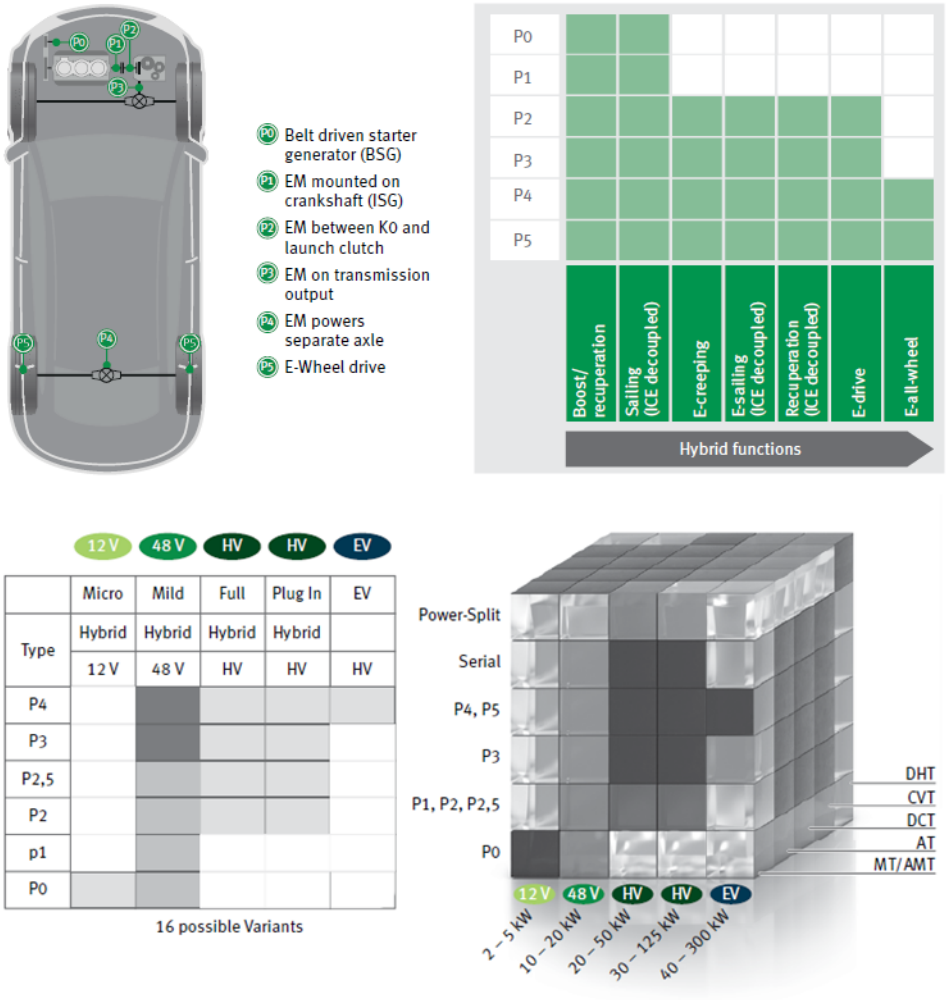


**Figure 7: Different hybrid architectures and their functionalities (top) and possible combination of architecture, topology, and transmission (bottom)** [29]

## 1.3 The Experimental and Numerical Approach

The previous section highlights the wide technological portfolio that currently characterize the automotive industry; as a direct consequence, the powertrain complexity is continuously increasing over time [41,42]. Furthermore, the entire picture gets even more sophisticated considering that the newly introduced powertrain subsystems cooperates with each other to control the vehicle behavior over numerous aspects [43]. Thus, the necessity of a reliable tool which can support the investigation and the further design of electrified powertrains is needed.

In this framework, the presented research activity was developed within the FEV benchmarking and simulation teams, with the aim of extending the internal knowledge and experience when dealing with all forms of electrified vehicles. Figure 8 show the work flow the proposed integrated approach. On one side, the goal is the development of a smart and sustainable methodology for HEVs testing and benchmarking; providing a good compromise between measurements

integrity and degree of complexity, intrusiveness and cost of the performed testing campaign. The experimental campaign relies on a bespoken non-invasive instrumentation effort and on a predefined testing protocol, made of a limited but effective number of tests performed both on the road and in laboratory. On the other side, the results of the testing campaign are used to calibrate a comprehensive HEV model, capable of simulating a wide range of hybrid architectures and technologies along different driving cycles. To this extent, the research project involves some of the most representative electrified vehicles available on the market, as described in Chapter 2, indispensable for the developing the methodology on the experimental and the simulation side. The instrumentation process and the variety of tests will be accurately explained. After the powertrain characterization, the gathered information are fit into the comprehensive 0D map-based HEV model. To this extent, Chapter 3 presents the model structure and its main subsystems, along with the most important mathematical equations that are used to model both the physical and the control aspects. The model is not only capable of assessing the Energy Management System (EMS) behavior for various architectures, but also fuel consumption and $CO_2$ emissions. Finally, the model output are presented in Chapter 4, for the three types of vehicle: a 48V MHEV, a P0-P2 Gasoline PHEV and a P2 Diesel PHEV. Firstly, the calibration process outcomes will be presented, with a focus on the correct detection of the power split, on the proper estimation of the electric energy flow and finally on the calculation of $CO_2$ emissions over the NEDC and WLTC cycles. To conclude, the model validation is carried out for the two PHEVs, which constitutes the more complex test cases, with the aim of assessing the model capabilities of vehicle behavior prediction along the WLTC and the RDE cycles, respectively.

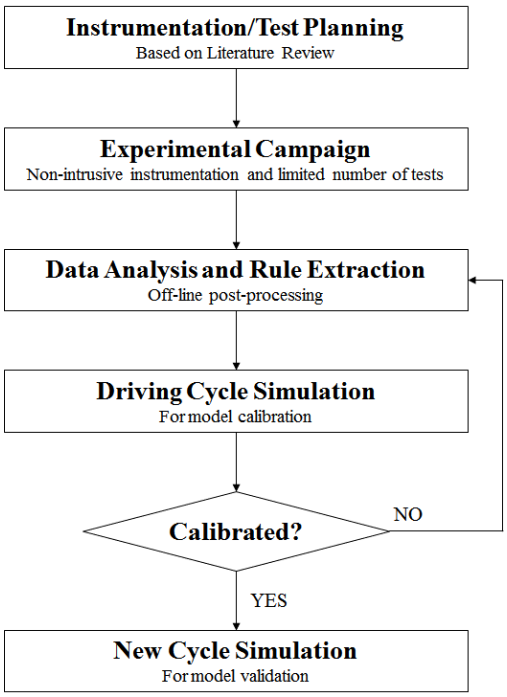


Figure 8: Workflow of the presented methodology

# Chapter 2

# The Integrated Methodology

Part of the work described in this Chapter was previously published in the following publications:

- DiPierro, G., Millo, F., Scassa, M., and Perazzo, A., "An Integrated Methodology for 0D Map-Based Powertrain Modelling Applied to a 48 V Mild-Hybrid Diesel Passenger Car," SAE Technical Paper 2018-01-1659, 2018, https://doi.org/10.4271/2018-01-1659.
- DiPierro, G., Millo, F., Tansini, A., Fontaras, G. et al., "An Integrated Experimental and Numerical Methodology for Plug-In Hybrid Electric Vehicle 0D Modelling," SAE Technical Paper 2019-24-0072, 2019.
- DiPierro, G., Millo, F., Cubito, C., Ciuffo, B. et al., "Analysis of the Impact of the WLTP Procedure on CO2 Emissions of Passenger Cars," SAE Technical Paper 2019-24-0240, 2019, https://doi.org/10.4271/2019-24-0240.
- DiPierro, G., Millo, F., Galvagno, E., Velardocchia, M. et al., " A Reverse Engineering Method for Powertrain Parameters Characterization Applied to a P2 Plug-In Hybrid Electric Vehicle with Automatic Transmission," SAE Technical Paper 2020-37-0021, 2020.

This chapter presents the experimental campaign carried out at FEV Italia facilities on different hybrid powertrain architectures, such as HEV and PHEVs, essential for the development of the integrated methodology. The main activity is the benchmarking of complex electrified vehicles with a standard and smart testing procedure, which avoids a highly intrusive instrumentation and a time and resource consuming testing protocol.

The purpose is the characterization of the powertrain components via working maps, and the reverse engineering of the EMS through a limited number of information derived from the experimental campaign. Thus, the vehicles were

tested both on the road and in laboratory over different missions and driving cycles according to the respective regulation requirements. The need of characterizing the vehicle behavior is indispensable to gather a conspicuous amount of information which will be later used for the calibration and validation of the vehicle model.

## 2.1 HEV testing: a complex picture

As introduced in the first chapter, the degree of complexity of newly developed automotive systems is growing in terms of technological content. In fact, if compared to the past, new powertrains have more subsystems made of innovative and different components, requiring different inputs and outputs. With the introduction of new operating modes and constraints, with the propagation of electronics and mechatronics in hybrid electric vehicles, unique design and integration challenges have raised, thus system integration has become a key task in hybrid vehicle development. [44].

These vehicles depend on advanced electronically controlled systems working together across a wide range of operating conditions to ensure efficient performance, consumption, safety and reliability. Increasing electrical content and complexity coupled with higher on-board power require engineers to continually improve their skills and develop a different approach within the whole powertrain development chain [45].

Testing different HEV solutions available on the market or at concept level could be a crucial activity in different situations, such as components development and calibration or in a merely benchmarking job. As far as testing complex hybrid electric vehicles is concerned, it becomes central to understand how subsystems are composed and how the interaction between them works. Therefore, literature review and data gathering has to be done in order to proceed to vehicle investigation. Afterwards, powertrain instrumentation and test scheduling are carried out.

Considering that hybrid electric vehicles combine components from the traditional internal combustion engine powertrain with electronic drivetrain parts, such as electric motors/generators, one or more battery packs, and various controllers and sensors, engineers now have to deal with a larger portfolio of data output [46]. Hence, this activity aims at fully exploiting the usefulness of an experimental campaign, at vehicle and component level, on the experimental and the simulation side. Vehicle testing establishes a milestone in the proposed methodology and can be used in different ways, as listed below [47]:

- Investigate power generation and its split for motor drives and controls, regenerative braking, boosting, battery charging, etc. Analyze different aspects, such as thermal, electrical, magnetic, etc.
- Evaluate HEV configuration tradeoffs (parallel, serial, or complex)

- Design, test, and verify EMS in terms of control strategies, power management, torque/speed coupling, and vehicle dynamics
- Extract rules implemented in the Hybrid Control Unit
- Acquire $CO_2$ and fuel consumption values throughout real-world driving missions
- Verify pollutants emissions limits such as $NO_x$, CO, THC and PM/PN
- Create the base for vehicle modelling via experimentally-defined operating maps
- Analyze and size HEV and BEV powertrains and components (motors, battery and controllers)
- Analyze the impact of complex and innovative power electronics systems
- Optimizing the power systems in HEVs to increases fuel economy and reduces emissions, while still fulfilling the drivability requirements.

## 2.2 Case study

The development of the experimental methodology and the validation of the simulation platform are based on the test activities carried out on three different hybrid passenger cars with different level of hybridization and powertrain configuration. Since the purpose is to validate a methodology applicable to both HEVs and PHEVs, three different vehicles have been investigated, later addressed with a number for confidential reasons:

- a 48 V Mild-Hybrid (MHEV) P0 Diesel car, Euro 6 compliant, equipped with a six speed Manual Transmission (6-MT), hereafter referred to as Vehicle 1;
- a P0-P2 architecture gasoline Plug-in HEV, Euro 6 compliant, equipped with a six speed Dual-Clutch Transmission (6-DCT), hereafter referred to as Vehicle 2;
- a P2 architecture Diesel Plug-in HEV, Euro 6 compliant, equipped with a nine speed Automatic Transmission (9-AT), hereafter referred to as Vehicle 3;

For the sake of completeness, it is worth to mention that vehicles are listed and tested in an increased complexity order. The author believes this is the best way to test and develop the proposed methodology, since it was created from the scratch and the whole process was a work-in-progress activity.

### 2.2.1 Vehicle 1 Test Case

The first vehicle selected as a case study is a 48V Mild-Hybrid P0 Diesel car (MPV – Multi Purpose Vehicle) in which the main on-board energy source is the ICE. The engine is connected via a pulley to the electric motor/generator (hereafter referred to as BSG, i.e. Belt Starter Generator). The main vehicle characteristics are listed in Table 2. This vehicle relies on a 1.5 liter Compression

Ignition (CI) engine, coupled with a six speed Manual Transmission (6-MT). The P0 configuration (see also Figure 60 for parallel hybrid powertrain topology nomenclature), is made up of a 13kW electric motor/generator linked to the ICE by means of a pulley: the transmission ratio is equal to 3:1. A schematic of the powertrain layout is depicted in Figure 9: for this type of configuration, the AC/DC converter is axially integrated into the electric machine, whereas the DC/DC converter is located between the high-voltage and low-voltage side.

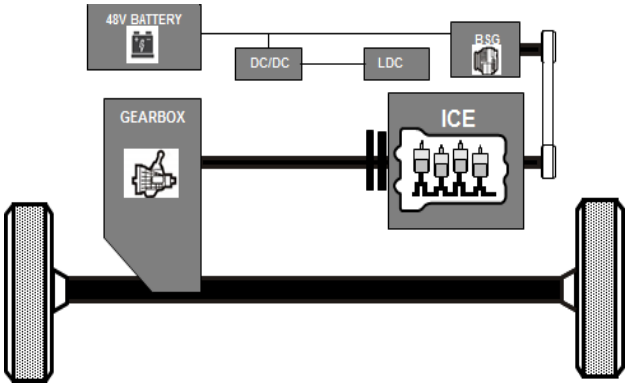


Figure 9: Vehicle 1 - Powertrain Layout

According to the power demanded by the driver and the driving conditions, the can work in two different hybrid modes:

1. **Electric Assist** mode: the BSG works as a motor for torque assist with the ICE turned on. Therefore, the 48V battery is discharged, though supplying the 12V loads at the same time;
2. **Energy Recuperation** mode: the BSG works as a generator absorbing the ICE torque or when the ICE is off during deceleration and braking, supplying simultaneously the 48V battery and the 12V loads.

To this regard, the driver has the only possibility to select a so-called “ECO mode”, which is enabled to be less fuel consuming and less aggressive in terms of drivability. The influence of this mode will also be investigated; even though it cannot be defined as a driving mode. Moreover, the tested 48V MHEV is not capable of pure electric driving. Therefore, the energy management system (EMS) is responsible for switching between Electric Assists and Energy Recuperation based on the driving conditions and on the battery energy content.

Table 2: Vehicle 1 - Vehicle and powertrain main specifications

| Technical Data | |
|---|---|
| **Vehicle** | Curb weight: 1615 kg<br>Configuration: Front Wheel Drive |
| **ICE** | In-line 4 cyl. Turbocharged Diesel<br>Displacement: 1.461 l<br>Rated power: 81 kW @ 4000 rpm<br>Rated torque: 260 Nm @ 1750 rpm<br>Gearbox: 6 - MT |
| **BSG** | Type: Asynchronous 48V<br>Max Power/Torque: 13 kW/50 Nm<br>Belt Transmission Ratio: 3.0:1<br>Max Speed: 18000 rpm |
| **Battery** | Type: Lithium-Titanate Oxide<br>Capacity: 0.15kWh / 3.12 Ah<br>Nominal voltage: 48 V<br>Cooling System: Air Cooled |

### 2.2.2 Vehicle 2 Test Case

The second vehicle selected as a case study is a P0-P2 gasoline plug-In Hybrid Electric Vehicle (PHEV), classified as a C-segment car. The powertrain layout is classified as P0-P2 (see Figure 60) and it is composed of a Naturally Aspirated (NA) Atkinson 1.6 liter SI engine, coupled with a six speed Dual-Clutch Transmission (6-DCT). The P0 electric motor/generator (hereafter referred to as HSG, i.e. Hybrid Starter Generator) is linked via a pulley to the internal combustion engine. Later on the driveline, a mechanical clutch is adopted to decouple the ICE from the drive electric motor (hereafter referred to as EM), which are coaxially placed before the transmission. The main vehicle characteristics are listed in Table 3. Depending on some conditions such as

vehicle speed, power demand and battery SOC, the powertrain can operate in two main modes:

1. **Electric Mode (EV)**: the HV battery energy is used for traction through the electric motor only, as depicted in Figure 10;

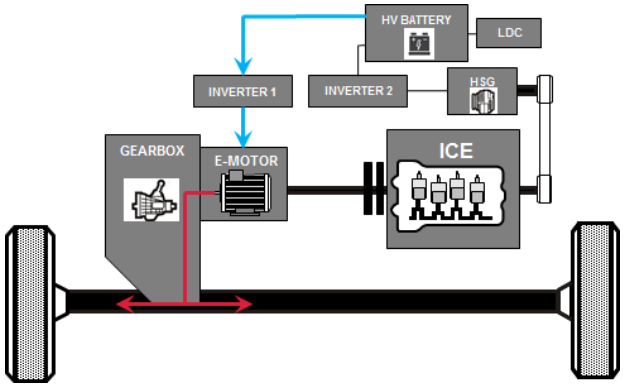


Figure 10: Vehicle 2- EV Mode

2. **Hybrid Mode (HEV)**: the ICE is turned on if higher power is requested and beyond a specific vehicle speed threshold. Thus, the vehicle can work in two different modes according to the battery SOC and accelerator pedal position:
    a. **Load Point Shift/Torque Assist**: the ICE is supposed to work closer to the optimal efficiency area by shifting its load operating points. Hence, when low power is demanded, the extra ICE power serves for battery recharging via the HSG and/or the electric motor (path A); on the other side, the EM and/or the HSG are enabled to increase the ICE torque (path B) in case of higher power demand from the driver. The two different paths are shown in Figure 11 (left);
    b. **Series Hybrid**: The ICE turns into generator and is not mechanically connected to the wheels. It operates almost at constant load and is used to feed the HV battery via the HSG, while the EM propels the vehicle as shown in Figure 11 (right).

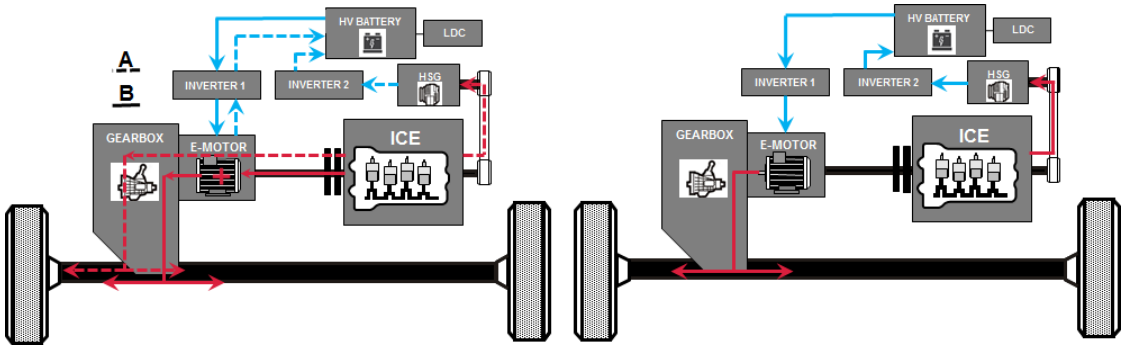


Figure 11: Vehicle 2- Load Point Shift/Torque Assist (left) and Series, HEV Mode

Table 3: Vehicle 2 - Vehicle and powertrain main specifications

| Technical Data | |
|---|---|
| **Vehicle** | Curb weight: 1495 kg<br>Configuration: Front Wheel Drive |
| **ICE** | In-line 4 cyl. NA Atkinson SI<br>Displacement: 1.580 l<br>Rated power: 77kW @ 5600rpm<br>Rated torque: 147Nm @ 4000rpm<br>Gearbox: 6 - DCT |
| **HSG** | Type: IPM synchronous<br>Max Power/Torque:8 kW/35.3 Nm<br>Min Power/Torque:-7.3kW/-21.4Nm<br>Belt Transmission Ratio: 2.6:1<br>Max Speed: 18000 rpm |
| **EM** | Type: IPM synchronous<br>Max Power/Torque:44.5 kW/170 Nm<br>Max Speed: 6000 rpm |
| **Battery** | Type: Lithium-ion Polymer (Pouch)<br>Capacity: 8.9 kWh / 24.7 Ah<br>Nominal voltage: 360 V<br>Cooling System: Forced Air Cooled |

### 2.2.3 Vehicle 3 Test Case

The third vehicle selected as a case study is a P2 Diesel plug-In Hybrid Electric Vehicle (PHEV), classified as a E-segment car. In this case, the 13.5 kWh Li-Ion HV battery in the hybrid vehicle is paired with a 2.0-liter Compression Ignition (CI) engine. The core is the 9-speed hybrid transmission, which is an automatic transmission (AT) with torque converter and an additional traction electric motor with integrated converter and a separating clutch. The main vehicle characteristics are listed in Table 4: a powerful 90 kW/440 Nm EM allows driving

in all-electric mode at a top speed of 130 km/h. Depending on the driver's demand, the four listed operating modes can be manually selected:

- **Hybrid Mode (HEV)**: it is the default setting; all functions, such as electric driving, boost and energy recovery, are available according to the driving situation and route profile, as depicted in Figure 12;

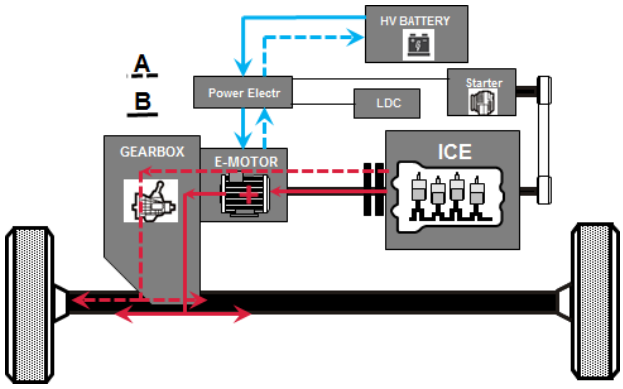


Figure 12: Vehicle 3- Load Point Shift/Torque Assist, HEV Mode

- **Electric mode (EV)**: electric driving by means of the main traction motor (Figure 13), for example in the city center. The accelerator triggers the pressure point at which the combustion engine is started;

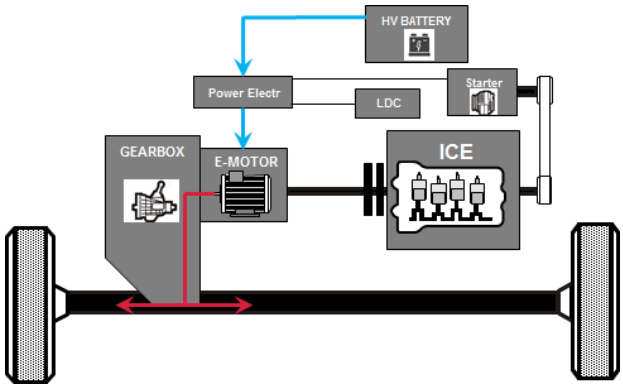


Figure 13: Vehicle 3- EV Mode

- **E-Save**: the HV battery is being recharged and held at a constant SOC to allow electric driving mode later;
- **Charge**: The battery is constantly charged while driving via the ICE load.

Table 4: Vehicle 3 - Vehicle and powertrain main specifications

| Technical Data | |
|---|---|
| **Vehicle** | Curb weight: 2060 kg |
| | Configuration: Rear Wheel Drive |
| **ICE** | In-line 4 cyl. Turbocharged Diesel |
| | Displacement: 1.950 l |
| | Rated power: 143 kW @ 3800 rpm |
| | Rated torque: 400 Nm @ 1600-2800 rpm |
| | Gearbox: 9 - AT |
| **EM** | Type: PM synchronous |
| | Max Power/Torque: 90 kW / 440 Nm |
| | Max Speed: 6000 rpm |
| **Battery** | Type: Lithium- nickel-manganese-cobalt |
| | Capacity: 13.5kWh / 37 Ah |
| | Nominal voltage: 365 V |
| | Cooling System: Water Cooled |

## 2.3 Vehicle Instrumentation: a non-invasive approach

Working at vehicle level means that vehicle instrumentation is a key point of the integrated methodology. Actually, the proposed methodology tries to avoid the tear down of the different powertrain components, for two main reasons: on one side, vehicle benchmarking for EMS investigation and fuel consumption, $CO_2$ and pollutants measurements do not justify a highly intrusive and costly instrumentation effort; on the other side, benchmarking engineers often have to deal with rentals or cars that might be used for other projects. This is where the need of a smart and sustainable methodology was borne.

Throughout the entire research activity, the laboratory testing were carried out on a chassis dynamometer, which has to recreate the road conditions by applying a resistive force to the vehicle in motion via the installed rollers actuated by electric motors. The test facilities is located in the BRC® R&D center in Cherasco (CN), Italy. A 3d render of the test environment and the top view from a camera are shown in Figure 14: the laboratory comprises a four Wheel-Drive (4WD) chassis dynamometer, made of two rollers benches with a diameter of 48 inches

(1.219 m) and an inertia of 1150 kg. The dyno tolerates a maximum speed of 250 km/h, a maximum traction force of 6600 Nm and an inertia range between 800 to 3650 kg. The cell is a climatic test cell, which means that the chassis dynamometer is installed in a room capable of simulating ambient conditions ranging from -40 to 45 °C with a variable humidity range [48].

**Figure 14: Schematic of Vehicle Installation (left) [49] and real top view (right) on a Chassis-Dynamometer**

Even though, the principle outcome of this activity is the investigation and reverse engineering of the powertrain behavior in terms of hybrid-system energy flow, sometimes testing has involved measurement of $CO_2$ and pollutants emissions. For the sake of knowledge, the sampling of gaseous emissions is carried out via a Critical Flow Venturi – Constant Volume Sampler (CFV – CVS), which has the purpose of maintaining a total constant flow rate under all driving conditions, after the exhaust gasses are diluted with air. Afterwards, mass-based emissions in g/km are calculated. The dilution of exhaust gasses is carried out to avoid the condensation of water vapor, responsible for the corruption of the measurements of particular pollutants since it prevents the reaction between different chemical species [48]. A schematic of the dilution system is shown in Figure 15. However, in order to have accurate measurements, the concentration of chemical species in the exhaust flow is reduced because of the dilution effect; this requires the usage of highly sensible and accurate measurement devices. Typically, the dilution ratio in the CVS is between 10 and 30, while the actual ambient dilution factor ranges from 500 to 1000 [50].

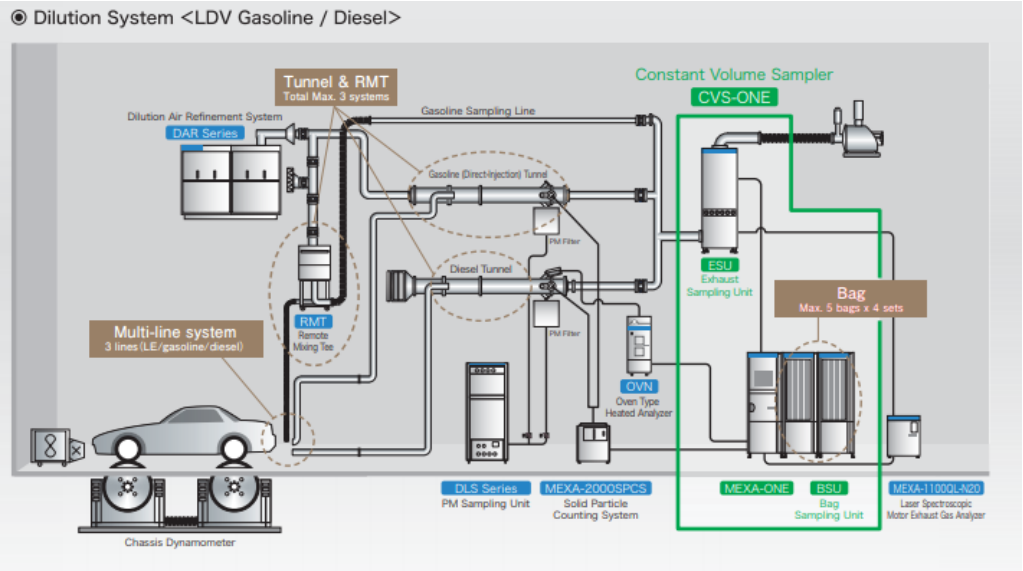


**Figure 15: Schematic of Emissions-Measurement Dilution System**[51]

In the next paragraphs, the instrumentation protocol is explained in detail, with the aid of schematics of the powertrain layouts and the sensors location. Dealing with both HEVs and PHEVs requires different effort and hardware specifications, due to the size of the electrical hybrid system and the location of the multiple energy sources. Thus, vehicle instrumentation is distinguished between the main job of instrumenting the electrical side and the additional instrumentation.

### 2.3.1 Electrical side instrumentation

As it has been already pointed out, the core of the whole activity relies on understanding the powertrain behavior on the hybrid electrical side, since it constitutes the novelty into the automotive industry. For this reason, the instrumentation procedure will be explained in details, vehicle by vehicle. This paragraph is completely dedicated to the instrumentation of the electric system by measuring mainly current and voltage, which are used to compute the electric power as reported in equation (2-1):

$$P = V \cdot I \tag{2-1}$$

Where $\boldsymbol{P}$ is the electric power in [W], $\boldsymbol{V}$ is the measured voltage in [V] and $\boldsymbol{I}$ is the current in [A]

As far as Vehicle 1 is concerned, it is clearly the simplest system among the three powertrains, from a technological point of view. In order to perform a worthy energetic analysis of the powertrain, the vehicle was instrumented as illustrated in Figure 17: five commercial shunts sensors were placed on both the HV and LV sides. To be more specific, it was necessary to measure current and voltage in five key locations, such as:

- 48 V battery input/output (I/O), for its energetic balance

- DC/DC High Voltage side, as depicted in Figure 16
- DC/DC Low Voltage side
- 12V Battery input/output (I/O), for its energetic balance and for the assessment of the loads consumption
- BSG electrical energy absorbed and generated.

The adopted sensors are capable of measuring both current and voltage: the ISAscale® IVT-S constitutes a high precision current and voltage measurements system, intended for DC applications. These shunts were inserted in series with the load, on the positive side, while the negative side had to be grounded. These devices have a range up to ±1000 A and the voltage channels include a range of ±600 V. By means of a 16-bit analog-digital converter, the shunt-based measurement system transforms the voltage variation into a digital signal [52]. The final acquisition step is based on a CAN bus interface used for data communication between the hardware and the software, passing through a CSM®'s AD MiniModules (ADMM) used for analogue signals collection and conversion into digital ones.


Figure 16: Shunt installation on the DC/DC HV side

As regard to Vehicle 2, a schematic of its powertrain layout with the instrumentation details is shown in Figure 18: the system is made up by more subsystems; hence, it is more complicated with respect to Vehicle 1. For example, the Hybrid Control Power Unit (HPCU) is a unique block containing the HV inverter that rules the connection between the HV battery and the two electric machines: the HSG and the EM. Moreover, this unit also includes the DCDC converter that feeds the low-voltage auxiliary 12V battery and the 12V loads. In order to achieve a complete powertrain characterization, it was necessary to measure current and voltage in four key locations, such as:

- The HV battery input/output (I/O), for its energetic balance;
- HPCU High Voltage side;
- DC/DC Low Voltage side

- 12V Battery input/output (I/O), for its energetic balance and for the assessment of the loads consumption
- Current to the HV A/C compressor, as an indication of its consumption

Normally, tests were performed with the HVAC system off in order to achieve a proper characterization of the system during normal traction conditions, thus, the A/C current measurement is not fundamental for this methodology. Moreover, the reader can note that HV AC 3-phase was not instrumented due to the complexity of the signals acquisition and the cost of the required instrumentation. Since it was crucial to gather information regarding the electric machines, it was possible to collect those kind of data available on the CAN bus (see next paragraph). Anyhow, the instrumentation and the processing of high-frequency 3-phase electrical signals could represent a further step of improvement for future work. As for the direct current (DC) HV side, high precision current and voltage measurement systems were used, via the application of LEM®'s HTR 500-SB current transducers. The measuring range of these open-loop Hall Effect transducers is about ±1000A, with an accuracy of 2% of the measured current. Like the previous vehicle, the acquisition measurement chain relies on a 16-bit analog-digital converter to transform the voltage output into a digital current signal [53].This time, voltage signals were measured by intercepting in parallel the wire (resistance) and the analogue signal was directly measured and converted through a CSM®'s ADMM.

Finally, Figure 19 depicts a schematic of Vehicle 3 powertrain layout with the performed instrumentation: also in this case, the Hybrid Control Power Unit (HPCU) is a unique block containing the HV inverter that rules the connection between the HV battery and the electric motor. However, this vehicle does not fit a HV starter/generator, but it has a common 12V starter. With the aim of performing a complete powertrain characterization, it was necessary to measure current and voltage in four key locations, such as:

- The HV battery input/output (I/O), for its energetic balance;
- HPCU High Voltage side;
- DC/DC Low Voltage side
- 12V Battery output, for its energetic balance and for the assessment of the loads consumption

Measurements in these 4 points were carried out using the previously described ISAscale® IVT-S high precision current and voltage measurements system. Additionally, secondary devices were instrumented via LEM®'s HTR 500-SB current transducers. Even though the investigation of the following devices is not strictly required to achieve the goal of this activity, it could give some additional information regarding the powertrain behavior and the energy split:

- Positive Temperature Coefficient (PTC) Thermistor HV current, used for cabin heating [54];
- Gearbox oil electric pump for transmission lubrication
- 12V conventional starter

As already mentioned, this vehicle features only a HV AC PM Synchronous motor (PMSM), which was not instrumented due to the complexity of the signals acquisition and the cost of the required instrumentation. As explained for Vehicle 2, it was possible to characterize the EM via data available on the CAN bus (see next paragraph).

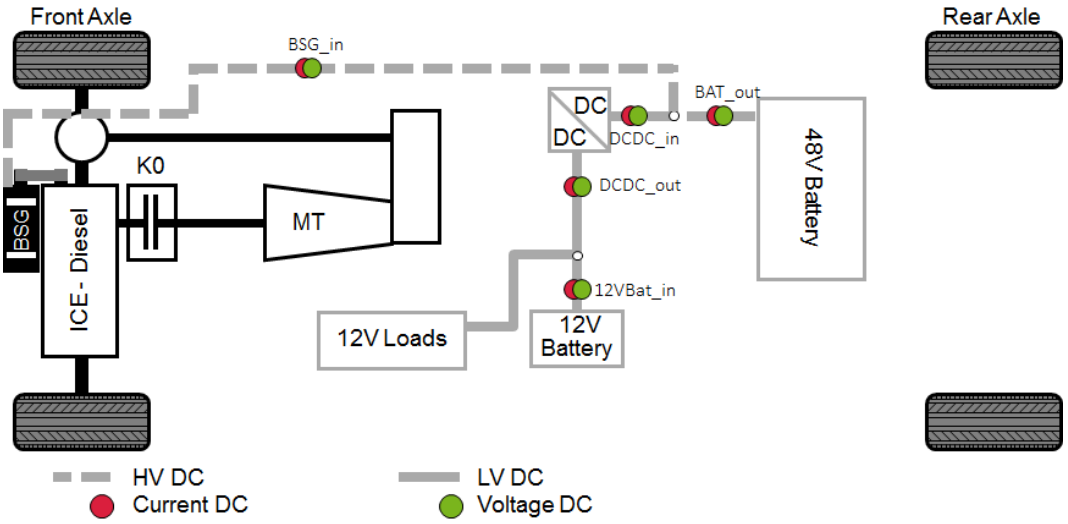


Figure 17: Vehicle 1 - Powertrain layout with instrumentation details

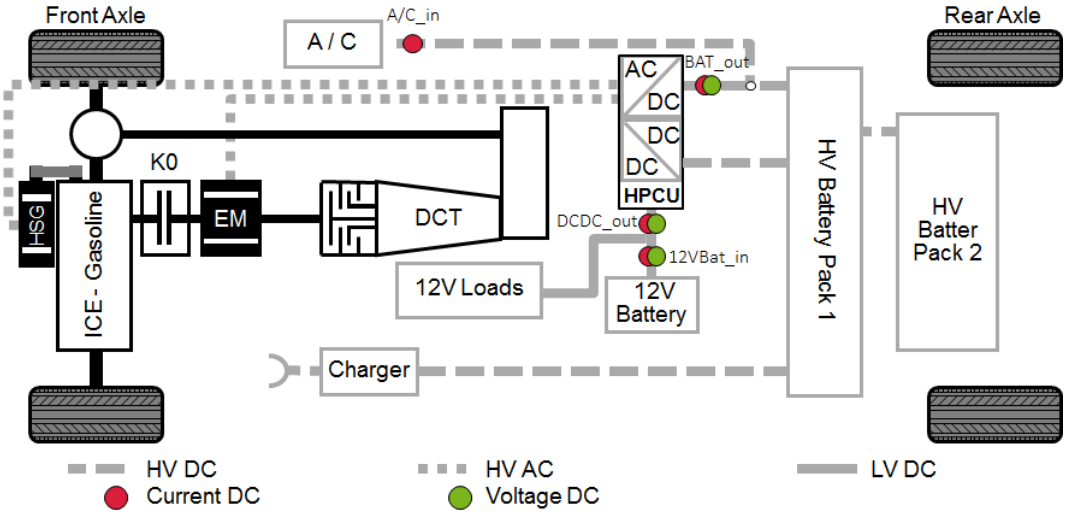


Figure 18: Vehicle 2 - Powertrain layout with instrumentation details

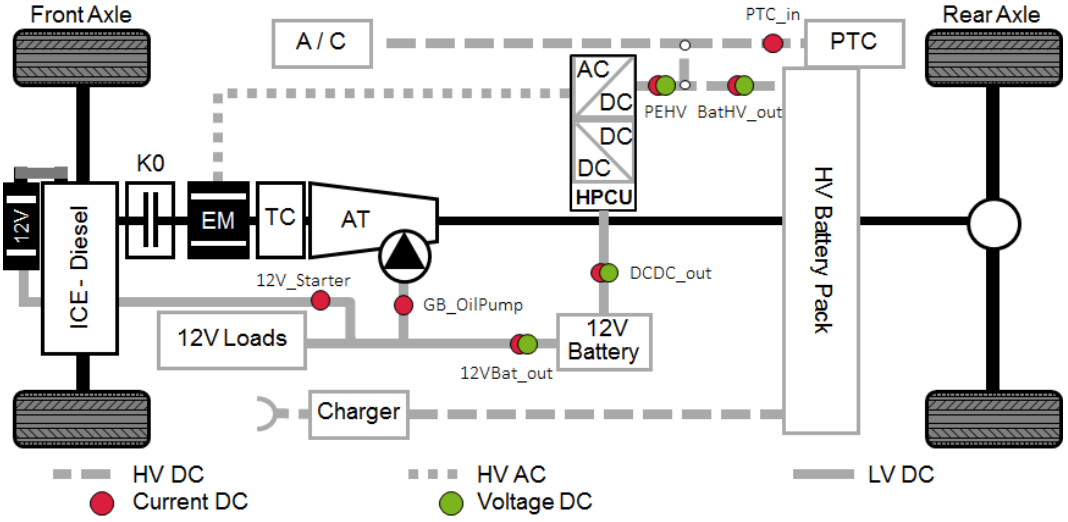


Figure 19: Vehicle 3 - Powertrain layout with instrumentation details

### 2.3.2 Additional instrumentation

As already discussed, dealing with electrified vehicles means dealing with multiple energy sources. The previous paragraph presented in details the main instrumentation process, which is dedicated to the vehicle electric system. However, in this paragraph the additional instrumentation and measurements carried out during the experimental campaign will be introduced. For the sake of brevity, the additional procedure will be explained and applied only on Vehicle 3, but the reader has to keep in mind that this was performed for the three case studies.

A fundamental system to instrument to understand the thermal management of the vehicle is the cooling circuit. Nowadays, due to the presence of more subsystem and because of their complexity and different requirements, more cooling circuits can be found on HEVs. To keep this methodology smart and cost effective, only temperatures in key locations were measured by means of type K thermocouples. As depicted in Figure 20 with a star marker, the engine coolant temperatures is measured at both inlet (blue pipe) and outlet (red pipe), in order to understand when the warm-up phase is over and its influence on the cold start strategy. Moreover, other thermocouples were placed on a secondary cooling circuit, used to control the temperature of the HV system (see Figure 21). In this situation, the main concerns is detecting the coolant temperature at the inlet and outlet of the HV battery, and its surface temperature. Additionally, there are other interesting locations for temperature measurements, such as the On-board Charger (OBC) cooling outlet, temperatures before and after the by-pass valve that opens the circuit towards the heat exchanger and towards the intersection with the HVAC system. An example of thermocouples installation is given in Figure 22, where the HV battery surface temperature (left) and the engine coolant temperature (right) are measured. Signals from thermocouples were collected and

converted into digital signals by means of a CSM®'s Thermo MiniModules (THMM).

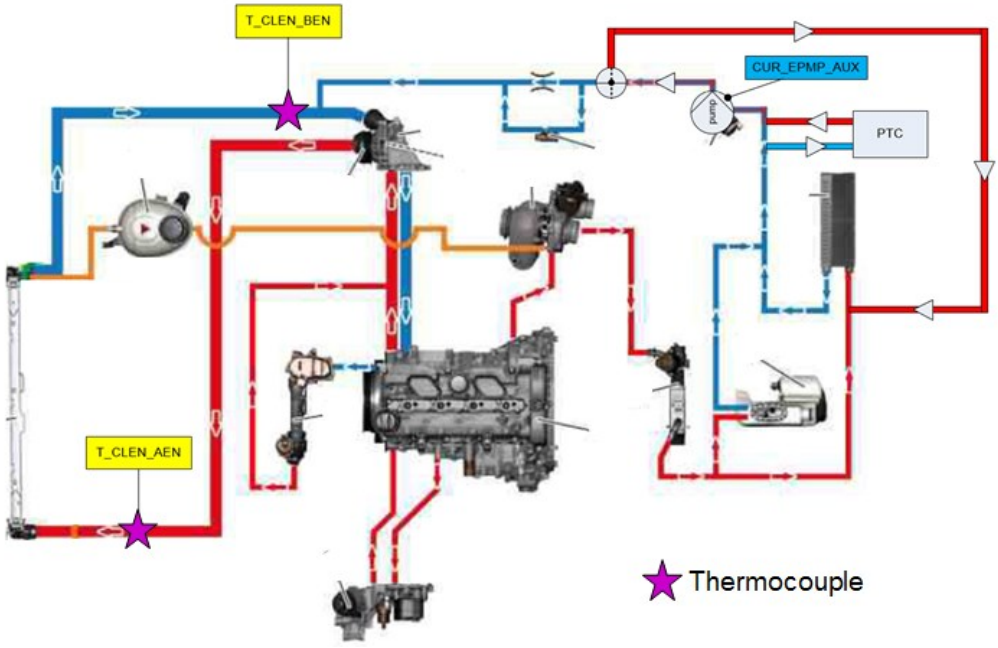


Figure 20: Engine Main cooling circuit – layout and instrumentation

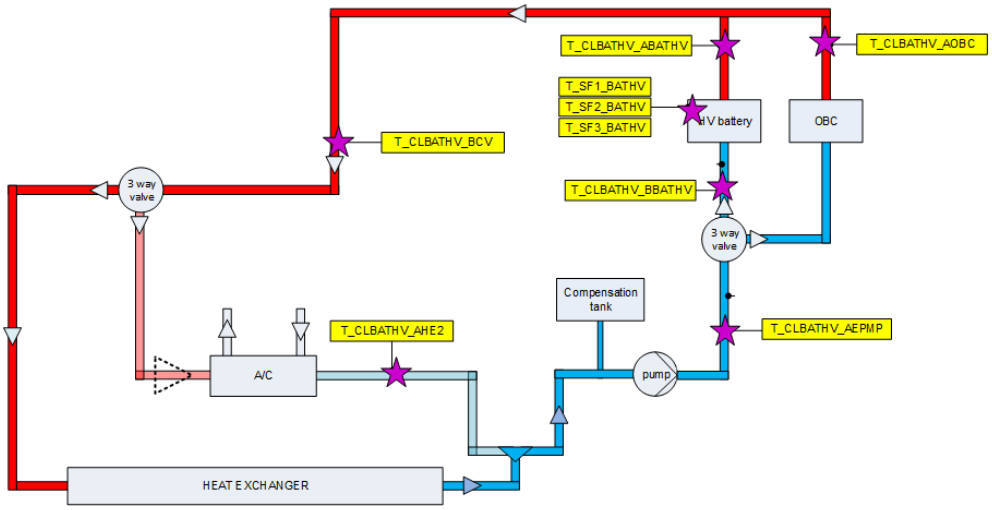


Figure 21: HV system cooling circuit – layout and instrumentation

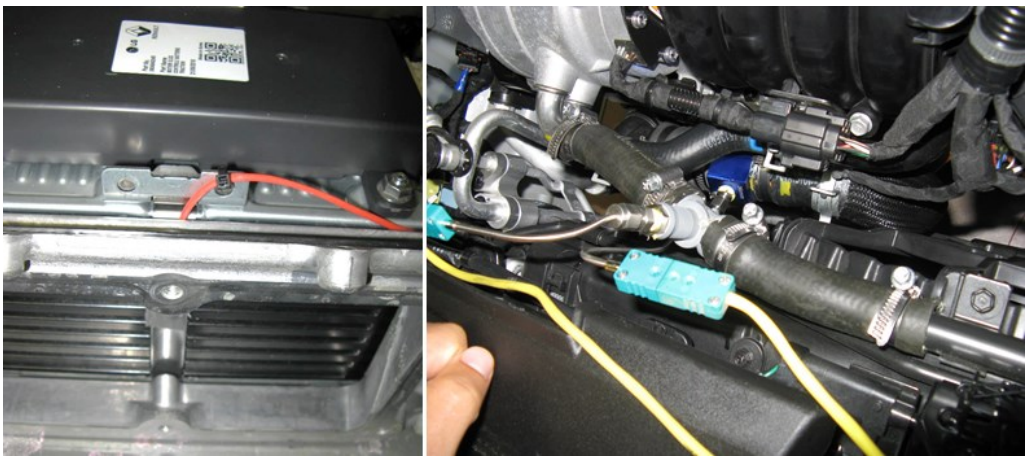

**Figure 22: Thermocouples for measurement of the HV Battery Surface Temperature (left) and Engine coolant radiator inlet/outlet**

Last step of the measurement chain is necessary to fill the gap given by those devices that were not possible to instrument. Hence, some of the variables used for the investigation were acquired using both the On Board Diagnostic (OBD [55]) and the vehicle CAN-bus protocol. AS for signals available on the OBD channel, an OBD scan tool, which belongs to the ETAS INCA suite, was used [56]. The OBD systems has the role of monitoring the performance of engine and after treatment components, especially for the supervision of pollutant emissions [57]. The OBD system detects system malfunctions; hence, it reads and communicates signals that could be interesting for the proposed analysis. The OBD-II specification requires a standard hardware interface: the female 16-pin (2x8) J1962 connector; a schematic of which is displayed in Figure 23 (left) while a picture from a car is shown on the right side.

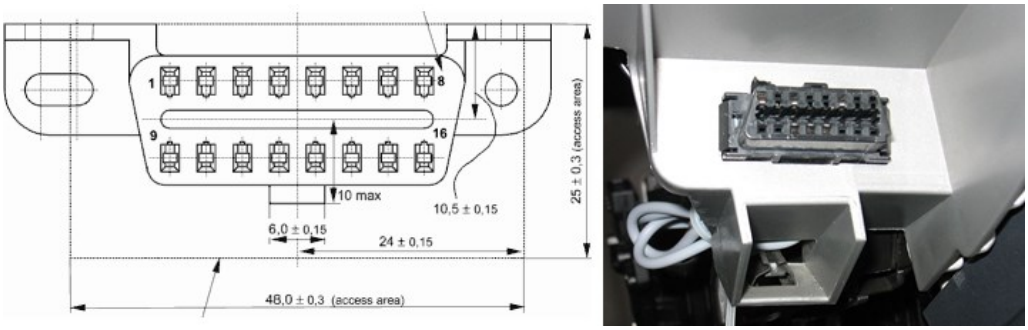


**Figure 23: SAE J1962 Vehicle Connector, Type A schematic** [58] **(left) and on a car**[59]

On the other side, not all the most interesting signals can be found on the OBD communication channel; therefore, some information were acquired directly from the different control modules (CM) available in the vehicle. The CAN bus communication network (developed by BOSCH) is a serial communications bus; it is a multi-master, message broadcast system [60]. Figure 24 illustrates the work performed over Vehicle 2 to read signals from both the Engine Control Module (ECM) and the Transmission Control Module (TCM). In this case, the signal acquired from the TCM are taken from the big CAN 1 connector displayed in

yellow. The CAN line number 2 is related to the ECM and the CAN 3 line is a flex ray type [61]. Thanks to data internally available in FEV and the know-how developed over the years, it was possible to re-engineer some signals read on the CAN network and decrypted in a dbc (database CAN) file.

As an example, variables like vehicle speed, engine torque and speed, accelerator pedal position, intake air-flow, battery State of Charge (SOC), EM and BSG torque and speed represents some of the variables read from either the CAN bus or the OBD channel, which are fundamentals for supplementary data post-processing to perform powertrain characterization. Of course, each application is different, thus some variables can or cannot be read from one of the two above-mentioned sources.

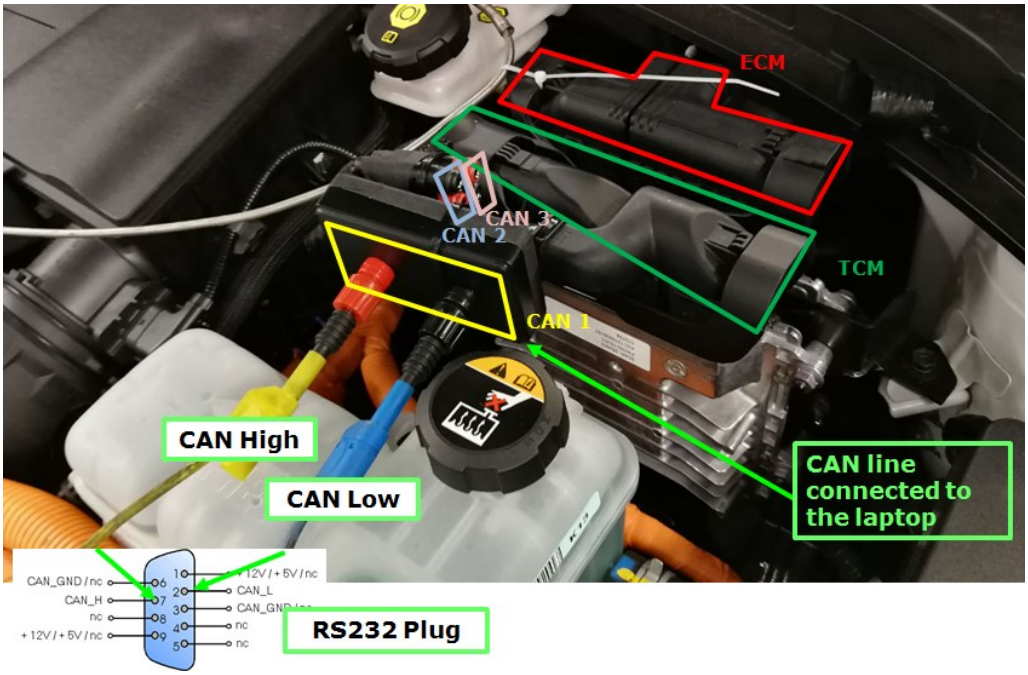


Figure 24: CAN logging from different Control Modules (CM)

For a better understanding, in Figure 25 is illustrated the measurement chain performed thanks to vehicle instrumentation: firstly, the testing engineer is responsible for data logging via a valid laptop that supports the implemented hardware. Then, all sensors placed in the powertrain need to be connected to the ETAS or CSM modules for analogic-to-digital conversion and resampling. Once the hardware is set and calibrated, the variable list is selected and displayed during the experimental campaign (the same signals will also be saved for post-processing). The authors decided to set an acquisition frequency of about 100 Hz, since it was considered acceptable for vehicle benchmarking. Later, during data processing, most of the times signals are resampled to a frequency of 20Hz, which is considered acceptable for calibrating a quasi-static model that does not have to simulate the transient behavior of the system.

As far as Vehicle 3 is concerned, this test case underwent a deeper instrumentation process due to the fact that the authors were also concerned about

the AT and Torque converter characterization, as well as the braking system investigation. As a matter of fact, this vehicle is the state-of the-art technology form different points of view; however, the instrumentation of the transmission output shaft and the braking calipers is not useful for the topic developed in this research activity. Hence, more info can be found in the related publication [62] and in the master thesis [63].

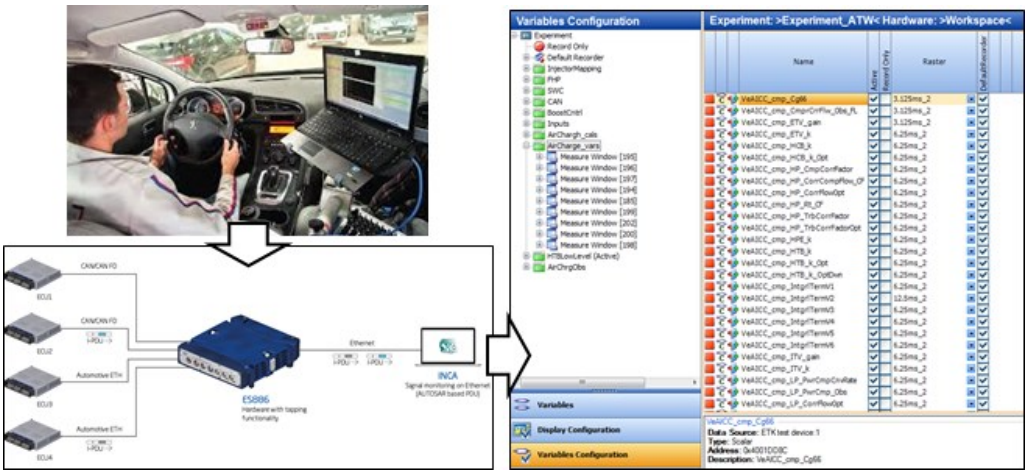


**Figure 25: On-board Measurement Chain via ETAS Inca** [64]

To conclude, it is important to point out that the simple performed instrumentation effort is necessary in order to characterize both the electrical and thermal side of the powertrain. In this regard, Figure 26 shows an example of vehicle installation on a chassis dyno and full instrumentation. Thanks to this procedure, it was possible to detect the power split between the different modules, and to investigate the EMS logics. In order to fulfill the scope of this research, only the most important signals for components characterization and for model calibration and validation were considered. Therefore, the analysis shown later (see Analysis of the Experimental Campaign) is focused on voltage and currents on the HV and LV side, together with dynamic behavior of the ICE and electric machines.

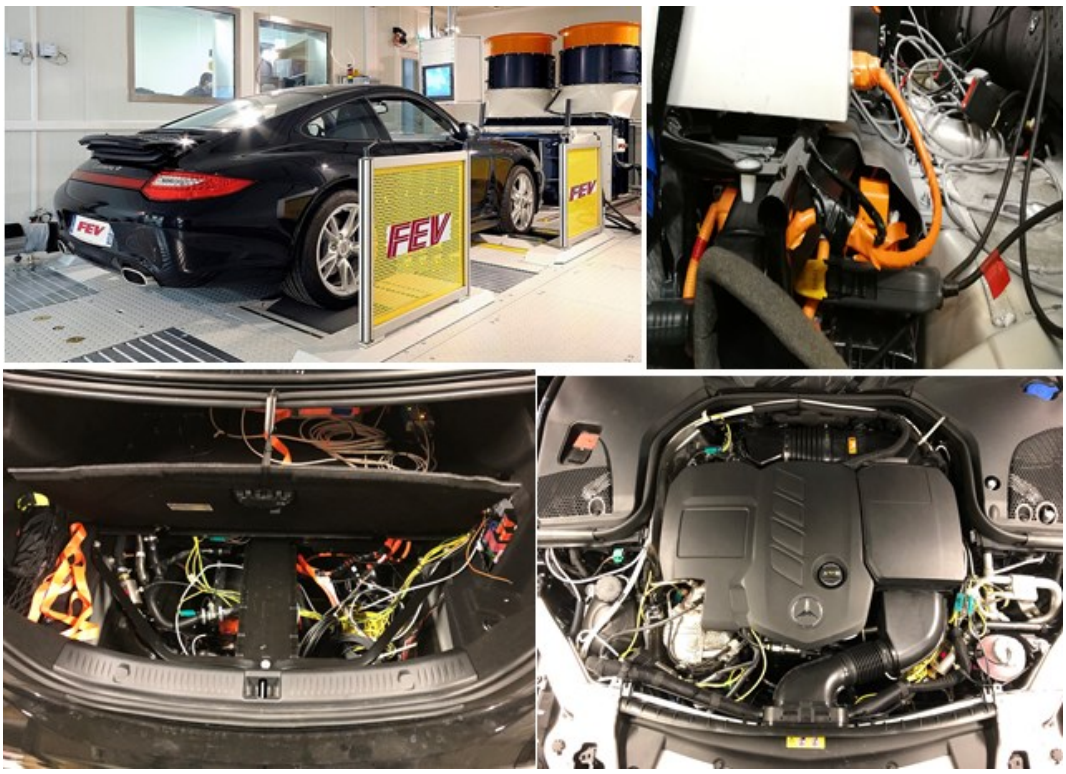


Figure 26: Example of vehicle instrumentation and dyno installation

## 2.4 Test Procedure

As mentioned in the *Introduction*, powertrain characterization necessitates both tests on the chassis-dyno and on the road. As far as the chassis dyno is concerned, measurements were performed following the Type Approval (TA) procedure; thus the WLTP and NEDC regulations [65,66] were consulted for Road Loads (RLs) and test mass determination: values are listed in Table 5. Moreover, laboratory and road testing can be further classified into different families: in the next paragraphs, different types of tests will be listed and explained. In particular, some specific maneuvers, called performance tests and critical missions, are intended to build up the dataset for components mapping, whereas the TA standard driving cycles were performed mainly for the calibration and validation of the vehicle model.

This paragraph will present the test procedure adopted for the three vehicles, which are different in terms of powertrain configuration and battery energy content. Tests are divided into two main families: Standard Driving Cycles and Characterization tests.

Table 5: Vehicle Road Loads and Test Mass

| | | Unit | NEDC | WLTP |
|---|---|---|---|---|
| **Vehicle 1** | Test Mass | kg | 1700 | 1794 |
| | F0 | N | 115.1 | 123.7 |
| | F1 | N/(km/h) | 0 | 0 |
| | F2 | $N/(km/h)^2$ | 0.0402 | 0.0402 |
| **Vehicle 2** | Test Mass | kg | 1590 | 1695 |
| | F0 | N | 101.7 | 144.4 |
| | F1 | N/(km/h) | 0.286 | 0.295 |
| | F2 | $N/(km/h)^2$ | 0.0305 | 0.0498 |
| **Vehicle 3** | Test Mass | kg | 2040 | 2162 |
| | F0 | N | 152.9 | 171.5 |
| | F1 | N/(km/h) | 0.809 | 0.833 |
| | F2 | $N/(km/h)^2$ | 0.0272 | 0.0280 |

### 2.4.1 Standard Driving Cycles

The first step of the experimental campaign is carried out in the laboratory, in order to prevent the measurements to be affected from the possible adulteration of the vehicle characteristics due to enhanced and aggressive on-road testing. Vehicles were tested on two standard driving cycles, the New European Driving Cycle (NEDC) and the Worldwide Harmonized Light Vehicles Test Cycle (WLTC).

The old TA cycle, which was still in use until September 2018, is the NEDC test: due to its simplicity and its smoothness, this test was performed to gather experimental data and for parameters tuning during vehicle model calibration, therefore the vehicle test mass and the speed profile strictly follow the regulation requirements. The gathered data were post-processed and used for HEV model calibration thanks to the fact that the NEDC has a modular vehicle pattern. In fact, it is composed of an urban phase (UDC) and an extra-urban phase (EUDC) allowing the user to easily detect the trends during the EMS investigation. The top part of Figure 27 illustrates the NEDC cycle speed trace and its phases.

The new test procedure is the Worldwide Harmonized Light-duty Test Procedure (WLTP) and its reference driving cycle is the (WLTC). It has been developed since 2007 by a technical group of the United Nations (U.N.) and introduced to close the gap between TA and "real world" CO2 emissions, while its application in EU started on September 2017 [67]. The introduction of WLTP brings several novelties to vehicle testing and procedure if compared to the NEDC; however, this is not discussed in this work since it is not in line with the topic of the research activity. More details regarding the impact of the WLTP introduction can be found in another author's paper [68].

The WLTP regulation defines different categories of hybrid-electric and electric vehicles: OVC-HEVs (off-vehicle chargeable hybrid electric vehicles); NOVC-HEV (not off-vehicle chargeable hybrid electric vehicles); and PEV (pure electric vehicles). All these kind of electrified vehicles are classified as Class 3 vehicles [69]. With respect to this study, Vehicle 1 is considered as NOVC-HEV, while Vehicle 2 and Vehicle 3 are OVC-HEVs. Emissions and a number of other parameters are tested over the respective Class 3b cycle, in both charge-depleting (CD) and charge-sustaining (CS) modes. The WLTC is made of four different phases: Low, Medium, High and Extra-High, as depicted in the bottom part of Figure 27. Due to the high dynamic of the cycle, characterized by more aggressive transient phases and less steady state parts, the WLTC is more representative of real driving conditions and it is mainly used for powertrain components mapping and model validation, in order to test the predictive capabilities of the simulation platform. A summary of the main characteristics of the two driving cycles adopted in the methodology is reported in Table 6. Afterwards in Results, the experimental measurements over the NEDC and WLTC cycles will be presented together with the model output, in order to validate the integrated methodology.

Starting from September 2017 [70–73], the TA authorities requires a procedure for measuring the pollutant emissions during real on-road driving, in addition to laboratory testing. The RDE adoption by the European Union (EU) is mainly a countermeasure to those research activities revealing increased nitrogen oxides ($NO_x$) emissions from cars equipped with Diesel engines, regardless of the fact that such vehicles are regulation complaints The RDE legislation, introduced in the Euro 6 regulation, has been proposed with 4 packages. The first RDE package, implemented in May 2015, outlines the RDE test procedure. The second RDE package, implemented in October 2015, outlines the NOx Conformity Factors and the introduction dates. The third RDE package, implemented in December 2016, introduces a Particle Number (PN) Conformity Factor and regulates the cold-start emissions. The fourth RDE package, implemented in May 2018, introduces the In-Service Conformity RDE testing and market surveillance and reduces the 2020 NOx Conformity Factor from 1.5 to 1.43 [74]. For a thorough understanding of the RDE regulation and its goals, please refer to [70–73,75].

Table 6: Summary of the characteristics of NEDC and WLTC class 3b

| | Unit | NEDC | WLTC |
|---|---|---|---|
| Duration | s | 1180 | 1800 |
| Distance | km | 11.03 | 23.27 |
| Avg Speed | km/h | 33.6 | 46.5 |
| Max Speed | km/h | 120 | 130 |
| Avg Accel | $m/s^2$ | 0.59 | 0.41 |
| Max Accel | $m/s^2$ | 1.04 | 1.67 |
| Stop Phases | - | 14 | 9 |
| | **SHARES** | | |
| Stop Phases | % | 23.7 | 12.6 |
| Constant Speed | % | 40.3 | 3.7 |
| Acceleration | % | 20.9 | 43.8 |
| Deceleration | % | 15.1 | 39.9 |

As far as this study is concerned, the RDE procedure is adopted as a further proving ground in order to enlarge the testing conditions under which the hybrid vehicles are investigated. Due to the newness of the real driving procedure, only Vehicle 3 was tested under the RDE protocol, hence the experimental and simulation outcomes will be later presented to validate the vehicle model: Table 7 highlights the main characteristic of the internally designed RDE cycle. The total energy required for driving the RDE cycle is calculated considering the test mass and RLs from the WLTC procedure, adding the road gradient contribute. On the other side, the traction energy is calculated in the same way, but only when the total force is positive, i.e. not during the deceleration phases. As reported in the table, the average speed is equal to the one of the WLTC, and the road gradient ranges from -15 to 15%.

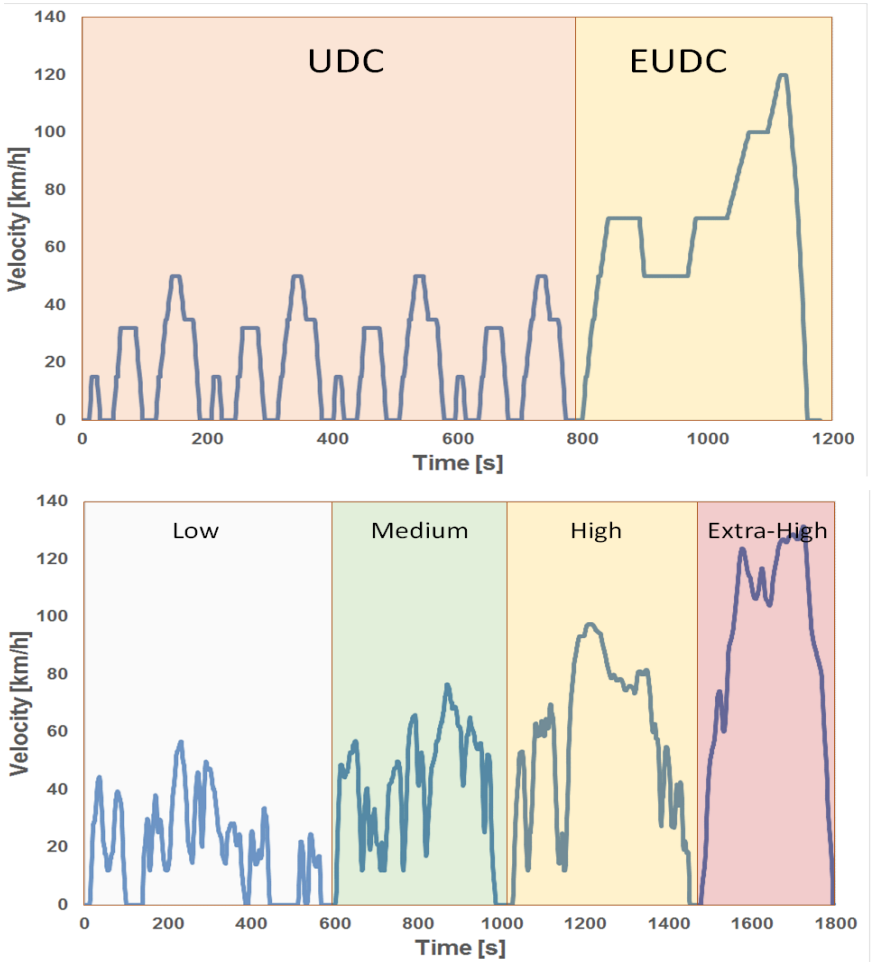


Figure 27: NEDC (top) and WLTC Class 3b (bottom) speed profile

The RDE path adopted during vehicle testing is illustrated in Figure 28 (top). According to the regulation, the test begins with urban driving in which vehicle speed has to be maintained below 65 km/h; this operation is carried out in the city of Turin, nearby the FEV's testing facilities. Afterwards, rural and motorway operations are conducted on major roads, driving away from the city on the south-west side. The requirements of the test are achieved without introducing artificial stop periods, and urban severity is achieved through moderate hill climbs and multiple crossroads. Both rural and motorways driving include hill climbs and descents, arriving at a peak of 370m of altitude. The total test time is around 112 minutes for a covered distance of 87 km, as shown in the bottom part of Figure 28.

Table 7: RDE Characteristic for Vehicle 3

| RDE – Vehicle 3 | | |
|---|---|---|
| Cycle Energy | kWh | 9.17 |
| Traction Energy | kWh | 16.64 |
| Avg. Speed | km/h | 46.25 |
| Max/Min Road Gradient | % | ±15 |
| Total Distance | km | 87 |

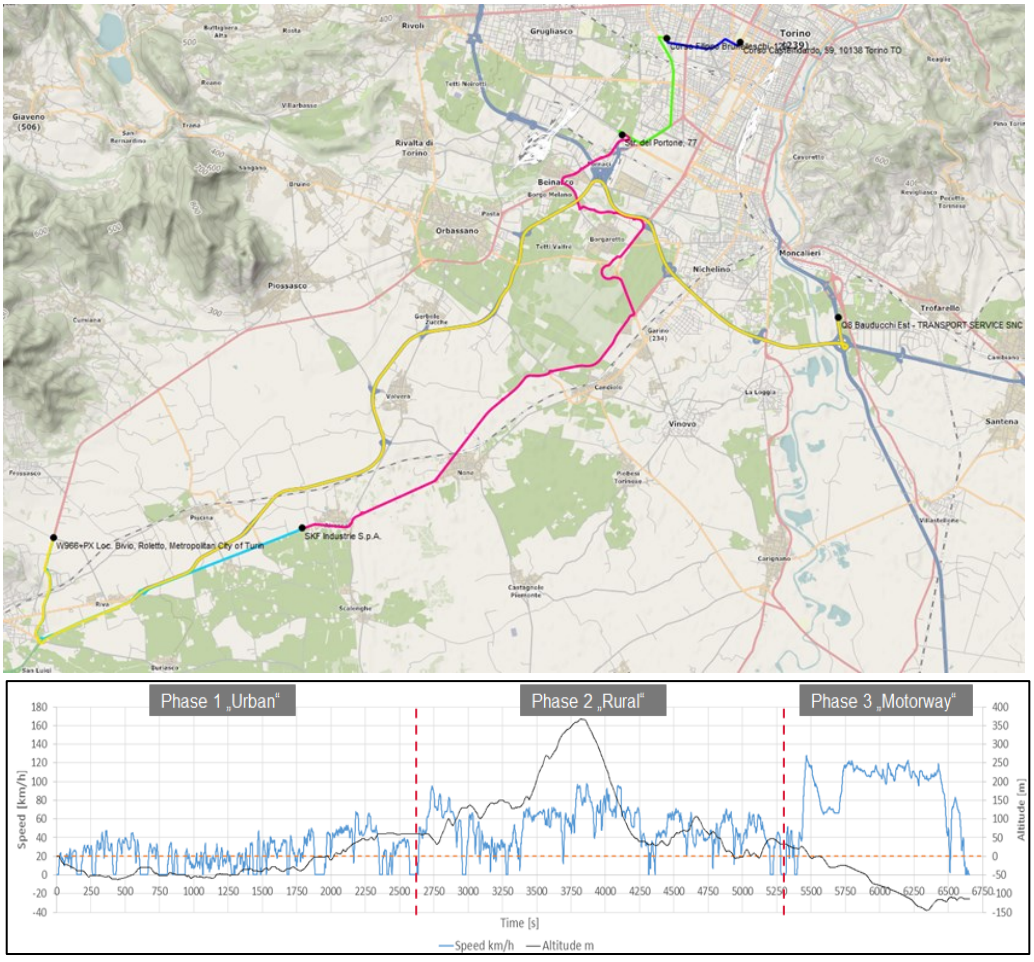


Figure 28: FEV RDE Route definition (top) and speed/altitude profile (bottom): phase 1 (urban) blue, phase 2 (rural) green and phase 3 (highway) purple

## 2.4.2 Characterization Tests

The second step of the experimental campaign is carried out both in the laboratory and on the road. The test categories introduced in this section are conceived in order to collect a sufficient amount of data regarding the interaction

between the different powertrain components. Therefore, the Performance tests are designed to explore the powertrain behavior under medium-to-high power request, while the Critical Missions want to simulate common driving condition faced in real life. Normally, it is good practice to test the repeatability of the maneuver by performing more than one repetition.

**PERFORMANCE TESTS**

The Performance tests explore aggressive driving situations that can cause tires slipping on the rollers and emergency issues related to power limitations of the chassis dyno. Thus, it is not always possible to carry out such demanding procedures on the test rig. For this reason, some activities are carried out on the road; this is the case of the standing-start maneuver from 0 to 100 km/h: in the proposed methodology, the acceleration from standstill is performed on the road. Moreover, the test is carried out with two levels of accelerator pedal position and with different levels of HV battery energy content, as listed in Table 8. This is common procedure in the automotive testing field because the outcome of this maneuver are used as a performance index. In this framework, this test has the benefit of exploiting a wide range of operating points, enabling both the ICE and the electric machines at different speed and loads. In this regard, Figure 29 depicts the speed profile followed in this test and the accelerator pedal position for Vehicle 1. The test was carried out at low (a), and high (b) battery initial SOC.

Table 8: Performance tests: standing-start and elasticity operating conditions

| **Standing-Start Acceleration** | | |
|---|---|---|
| 0 -100 km\h Acceleration | EV Mode<br>HEV High SOC<br>HEV Low SOC<br>Sport Mode | 50% - 100% Accelerator Pedal |
| **Elasticity Test** | | |
| 40 - 80 km/h<br>60 - 100 km/h<br>80 - 120 km/h | EV Mode<br>HEV High SOC<br>HEV Low SOC<br>Sport Mode | 50% - 100% Accelerator Pedal |

The elasticity maneuver is the other test belonging to the performance test family; it was carried out on the chassis dyno. In this type of test, there is a sudden power demand increase while vehicle is cruising at constant speed condition. The operating conditions are listed in Table 8: starting from various initial speed and

in different driving modes (i.e. different HV battery SOC), the vehicle is accelerated with two levels of accelerator pedal position. This test is useful to investigate the logic of the EMS and the ICE On/Off request. In the bottom part of Figure 29, the speed profile followed during multiple accelerations is depicted, together with the accelerator pedal position. Subplot (a) is related to a repeated 80-120 km/h acceleration test, carried out at high SOC and at gas pedal position about 100% (the kick-down position is reached in the first part). On the other side, subplot (b) depicts the same maneuver carried out at medium SOC with gas pedal position about 40-50%. Moreover, the impact of the ECO MODE was tested, since it is supposed to be the less fuel-consuming mode. For the sake of completeness, if the accelerator pedal is not fully depressed (i.e. it does not reach the end of the stroke), the "before kick-down" label is adopted.

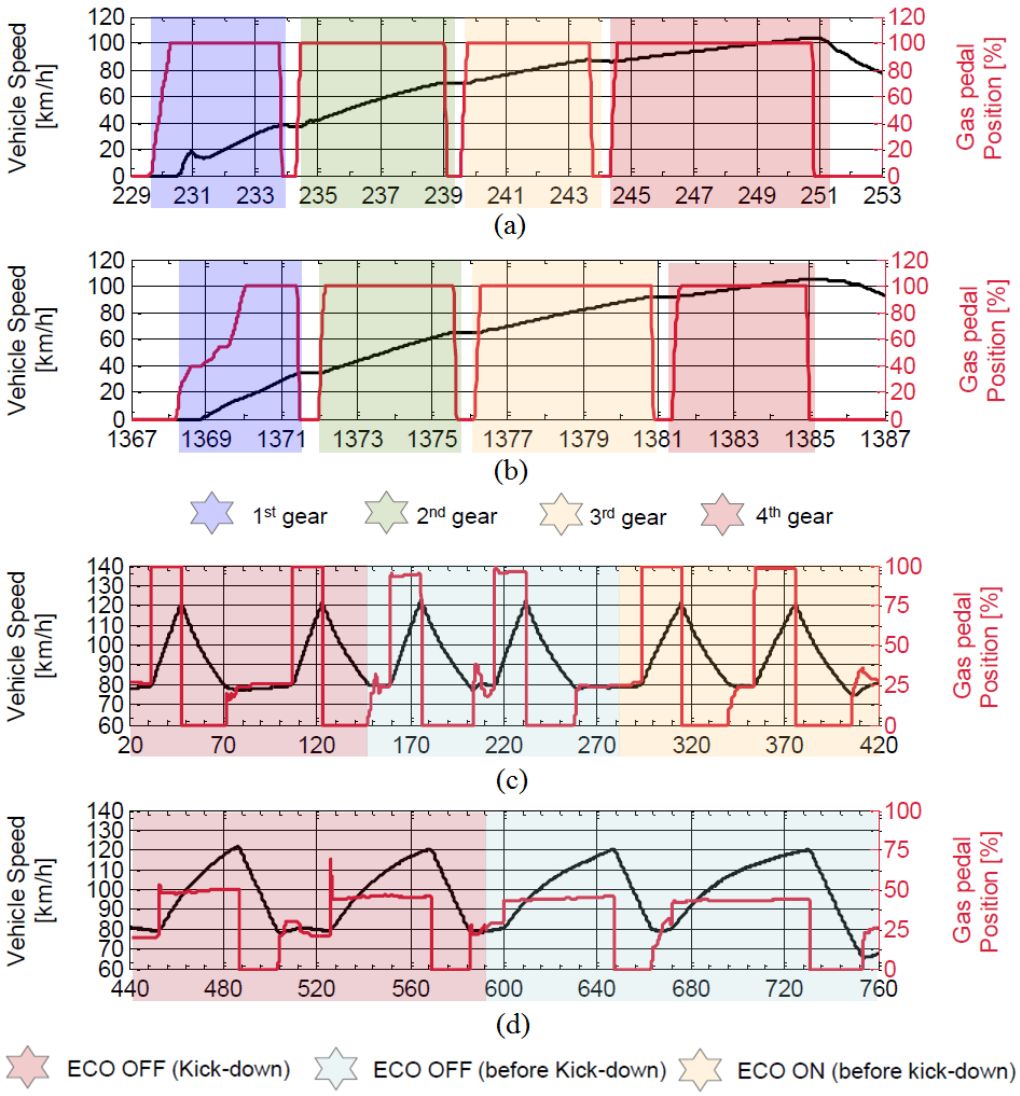


**Figure 29: Performance Tests - Standing-start 0-100 km/h for low (a) and high (b) battery initial SOC; Elasticity test 80-120 km/h maneuver for high SOC and high power request (c), mid SOC and low power request (d)** [76].

## CRITICAL MISSIONS

The label of Critical Missions is used to group tests that emulate ordinary driving conditions and that are relevant for the investigation and the reverse engineering of the EMS. In this regard, all the activities were performed on the chassis dyno: Table 9 illustrates the operating conditions of the Critical Missions campaign. As highlighted in the table, the same typology of test was carried out starting at different vehicle speed, investigating four different driving modes. Obviously, several repetition were performed of each test, such as constant speed driving, active braking, pedal release, and sailing. An illustration of the Critical Mission tests is reported in Figure 30: the first subplot (a) shows a steady-state driving maneuver at 70 km/h, carried out both in CS and CD mode, targeting mainly the switch between EV and HEV mode. The second subplot (b) shows the active braking maneuver from 100 km/h to 0 km/h, performed by actively depressing the brake pedal. The last subplot (c) shows an example of a sailing test, achieved by slightly releasing the accelerator pedal at 100 km/h. Vehicle sailing can be seen as a stop-in-motion function; use to disconnect the engine from the transmission and stopping (or idling) the engine, with the vehicle still travelling at a relatively high speed [77]. Only the pedal release test is not shown, since it is a normal deceleration procedure with the accelerator pedal released, performed to investigate the logic behind the regenerative braking at different speed and battery SOC.

**Table 9: Critical Missions: operating conditions**

| **Critical Missions** | | |
|---|---|---|
| Constant Speed<br>Active Braking<br>Pedal Release<br>Sailing | EV Mode<br>HEV High SOC<br>HEV Low SOC<br>Sport Mode | 30 - 50 - 70 - 100 - 120 - 130 - 150 km/h |

The next paragraph reports the outcome of the experimental campaign, especially regarding the Characterization tests. This part of the work aims at a deeper understanding of the EMS logics behind the powertrain behavior, in order to translate the gathered information into maps, threshold values and curves to be used into the all-in-one hybrid vehicle model.

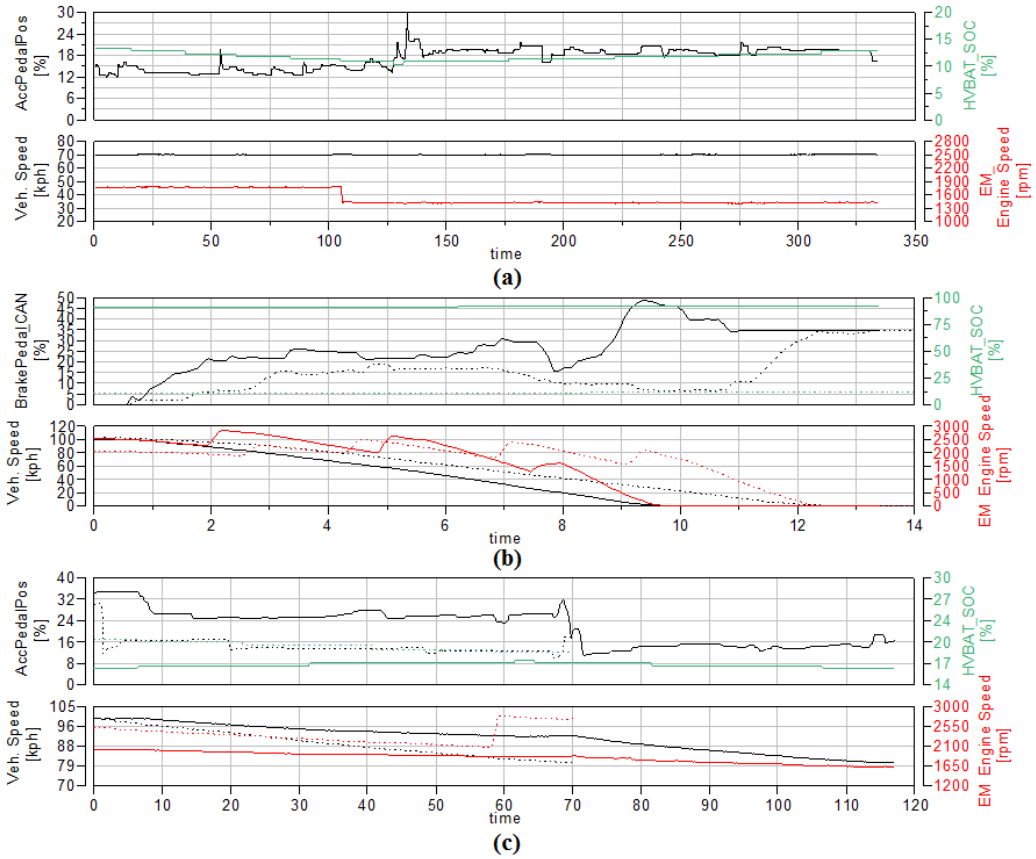


**Figure 30: Critical Mission tests: (a) Steady-State driving, (b) Active Braking and (c) Sailing** [78]

## 2.5 Analysis of the Experimental Campaign

The powertrain characterization was carried out thanks to vehicle instrumentation and signal acquisition from CAN and OBD network, as previously explained. In this paragraph, the outcomes of the different maneuvers are firstly presented, later, input creation for powertrain modelling is discussed. Therefore, the more relevant processed signals will be shown and only the most important test will be discussed, since they are useful for understanding and modelling the powertrain behavior. For a complete powertrain characterization, the whole set of data was analyzed, including output from standard driving cycles. It is worth to mention that the investigation of the hybrid system is mainly based on the so-called Characterization tests, while the standard driving cycles were used for model calibration and validation. Later in The Comprehensive xEV Model Chapter, some of the data measured in the experimental campaign will be adopted as input for the vehicle model.

### 2.5.1 Vehicle 1 Analysis

This section analyses the powertrain behavior of Vehicle 1 considering the main acquired signals form the Diesel engine, the BSG and the 48V battery, since this is P0 architecture.

The standing-start test was carried out on the road due to the power limitations of the chassis dyno. The acceleration from 0 to 100 km/h was investigated under two different levels of 48V battery SOC to evaluate the impact of this variable on the EMS and for battery modelling. In this regard, Figure 31 illustrates a set of data related to vehicle, ICE, BSG, 48V battery. Particularly, vehicle speed profile and the accelerator pedal position are shown in the first subplot; current measured with shunts from the BSG and the 48V battery is shown in the second subplot: positive motor current means motoring mode, negative current means generator mode. On the contrary, positive battery current means recharging, while negative current means discharging. In the third subplot torque from the ICE and the BSG are reported; finally, the 48V battery SOC with the at DC/DC converter input current are reported in the fourth subplot. The battery SOC is read from the CAN and it is the "displayed" value, hence it ranges from 0% to 100%, while the real value normally sweeps between 10-to-90%, in order to prevent an excessive battery derating. In particular, the top of the figure illustrates an acceleration carried out at very low SOC, which takes more time to bring the vehicle at 100km/h. Due to the limited battery energy content, the BSG switches between generator and motor mode. Especially in the first gear, the BSG works as a generator until the battery has been partially recharged and, afterwards, it is able to support the ICE with a very limited torque. The bottom part of Figure 31 shows the standing-start acceleration at very high initial SOC level (85%). This time, the BSG acts as a motor in order to help the ICE and reduce the turbolag effect for the entire acceleration. The accelerations drains the battery SOC to almost 70%.

The other characterization test was carried out on the chassis dyno. The elasticity maneuvers are useful for the BSG characterization and it was performed in various gears, various battery SOC levels and various accelerator pedal positions position. In particular, the elasticity test performed in second gear, from 20 km/h up to the maximum engine speed is reported in Figure 32. The test shown in the top part of the picture was carried out at relatively high battery SOC (40%), with high driver power request; additionally, the test investigates the influence of the ECO mode and of the kick-down. Clearly, there is no impact of the ECO mode regardless of the kick-down position. On the other side, when the ECO mode is on and the kick-down is not reached, the BSG boosts the ICE only for few seconds and mitigates the turbolag if. Moreover, the bottom part of Figure 32 illustrates the same test performed at low battery SOC (below 10%), with low driver power request (about 40% gas pedal). In this case, the BSG must work as a generator, even if performing an acceleration. Only when the battery energy level has increased to about 40%, the BSG works as a motor. In this situation, the ECO mode does not have a significant impact.

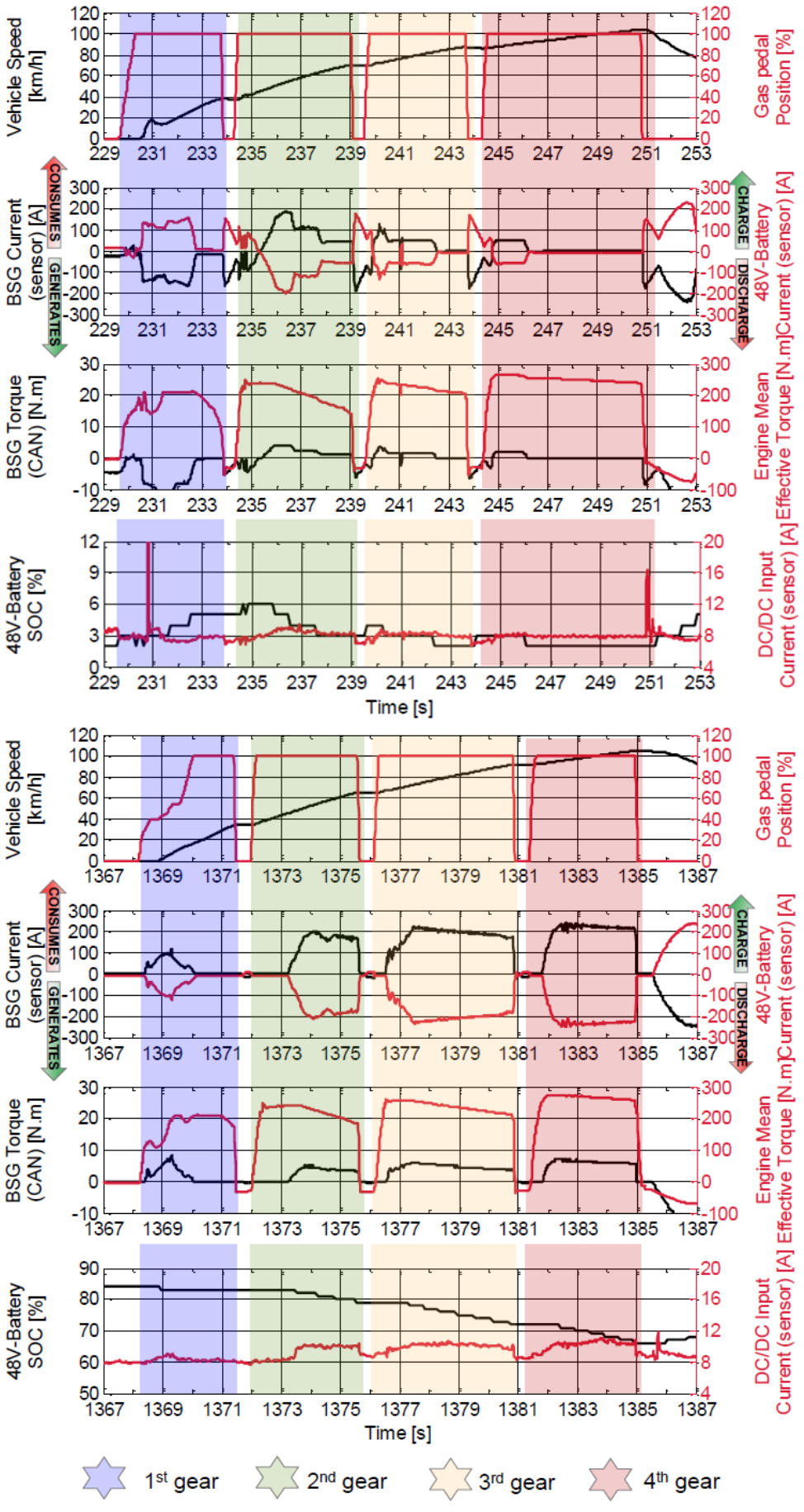


Figure 31. Measurements for 0 – 100km/h performance test at low SOC (top) high SOC (bottom)

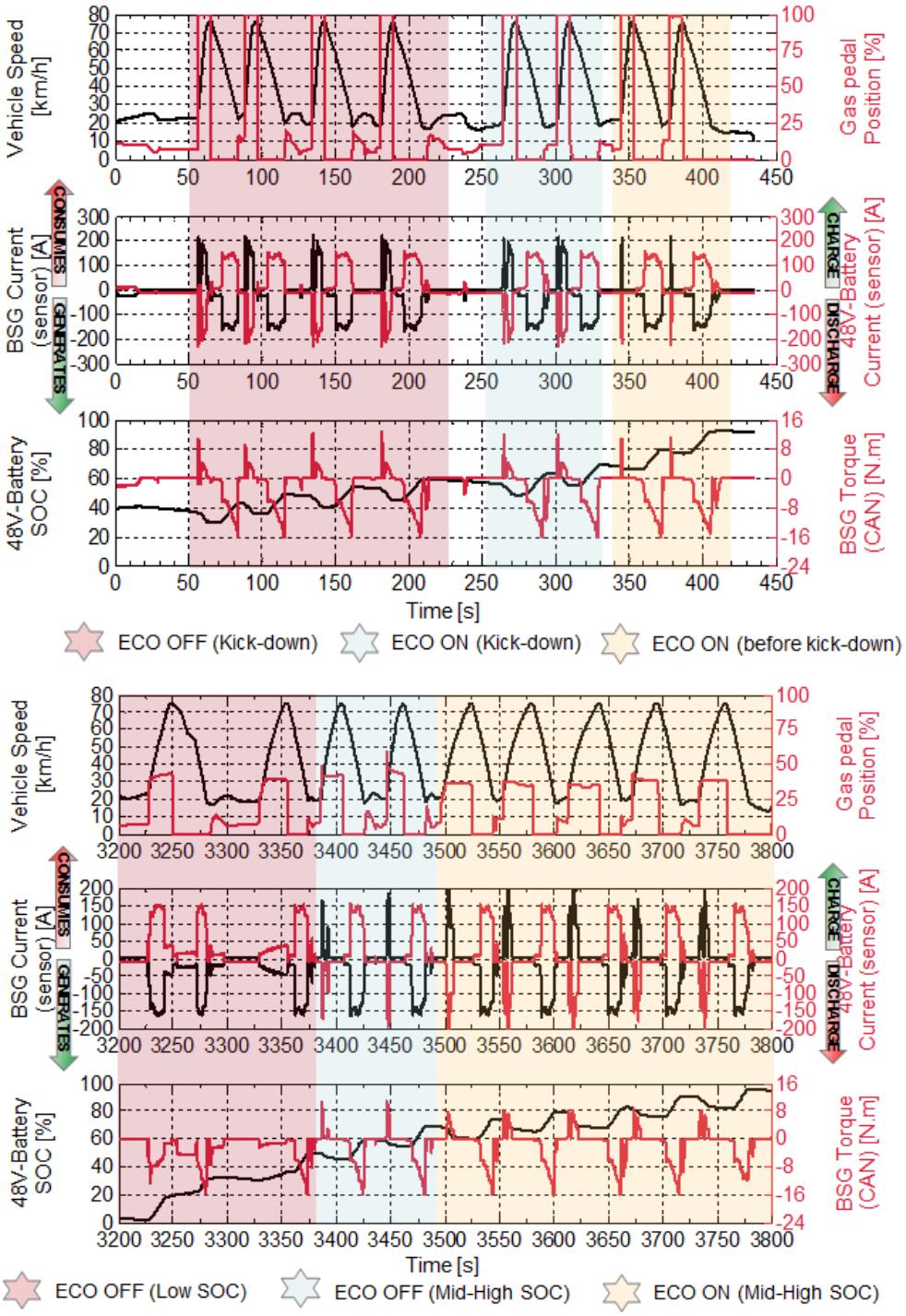


**Figure 32. 2nd gear elasticity test measurements at high SOC for high power requests (top) and low SOC for low power requests (bottom)**

Finally, to reach higher vehicle speeds, the elasticity was performed in sixth gear, going from 80 km/h to 120 km/h, in different situations. The test shown in the top part of Figure 33 was carried out starting at 90% battery SOC and with high power demand, with gas pedal position close to 100%. In this case that the kick-down is not reached, the BSG gives a longer support; moreover, when the vehicle runs in ECO mode, the BSG supports the ICE only for mitigating the turbolag, otherwise it can support the ICE for a longer time. To conclude, data reported in the bottom part of Figure 33 refer to a situation in which the battery

SOC goes from 80% to medium values and accelerator pedal position is around 45%. At the beginning, with high SOC, the BSG reduces the turbolag effect giving more power, providing continuous support. However, in the last two tests, battery SOC is below 40% and battery charging is forced.

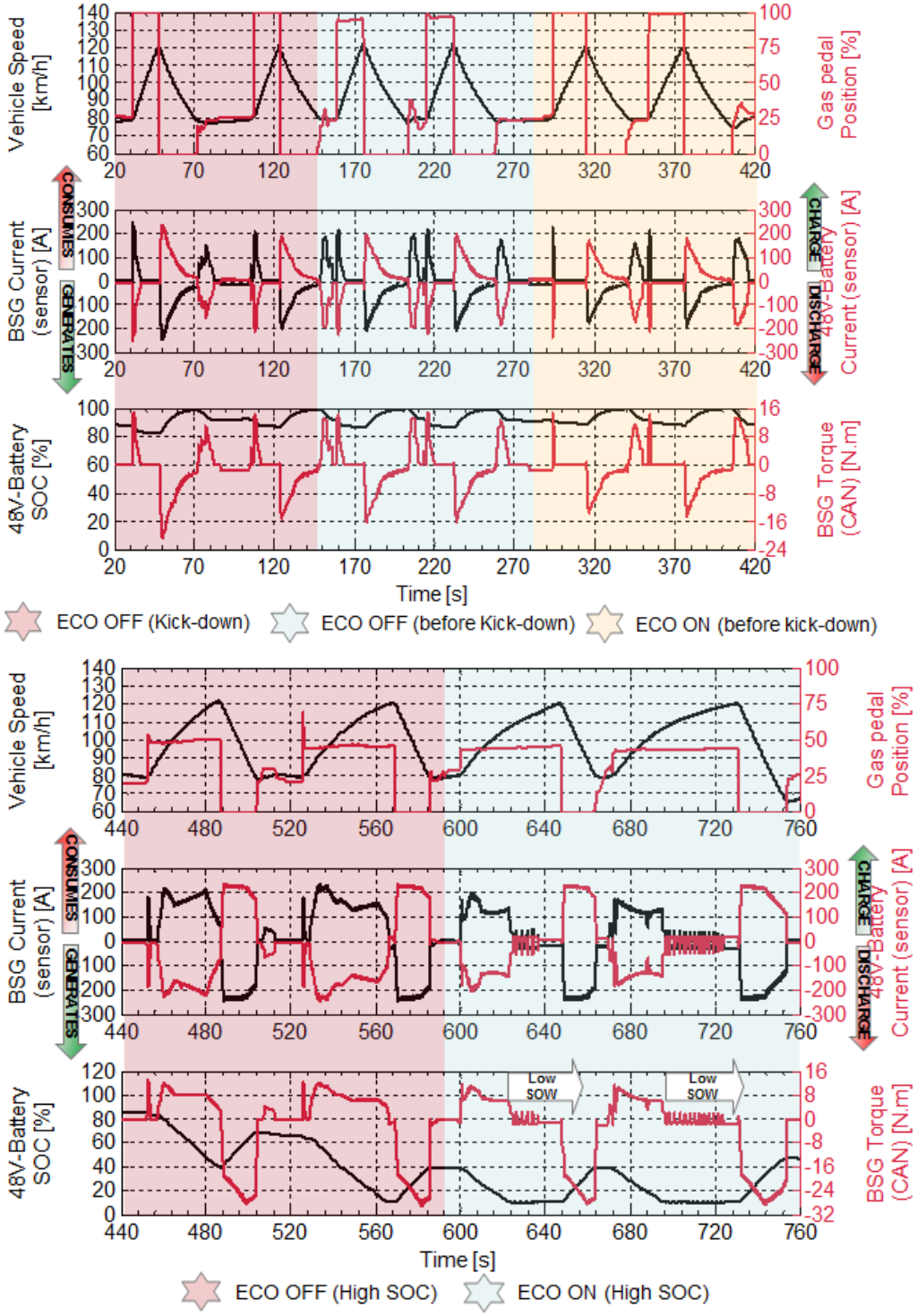


Figure 33. 6th gear elasticity test measurements at high SOC for high power requests (top) and high SOC for low power requests (bottom)

As an example of Critical Missions, Figure 34 depicts the output of the steady state driving, performed on the chassis dyno at different vehicle speed levels. This

type of maneuver was used to assess the BSG working points and the 48V systems discharge strategies. As highlighted in the following picture, the test started at medium SOC (40%) while the vehicle is driven at constant speed, without any kind of acceleration/deceleration. It can be noticed that the battery SOC is kept constant around 40% until the vehicle slows down to 30 km/h, and later the 48V battery is discharged to its lowest content. Throughout the entire test, BSG always works as a generator, except for the part in which the battery is depleted (positive BSG current).

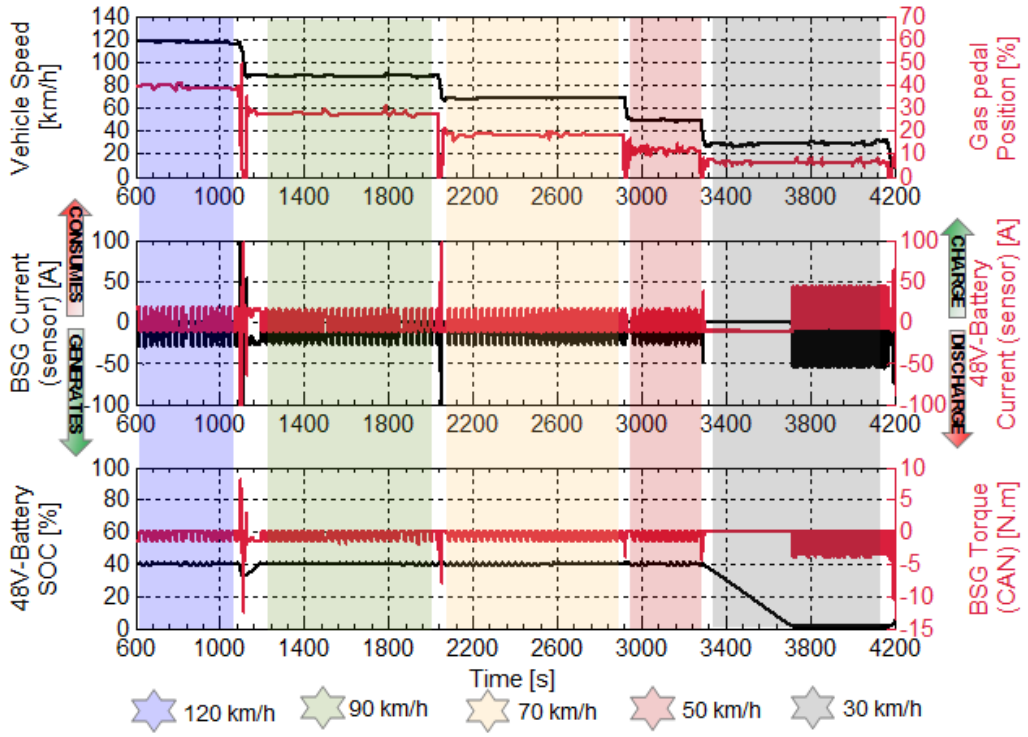


Figure 34: Steady State driving on the chassis dyno at different vehicle speeds

In conclusion, the tailored experimental campaign has been useful to gain a deep understanding of the P0 architecture behavior; data gathered during the characterization tests and the standard driving cycles are merged for powertrain investigation. In Figure 35 it can be noticed that the starter/generator is used as a reliable support for the reduction of the turbolag, in particular the torque assist function works around the low-end torque (low speed – high load) area to give a faster powertrain response and to allow down speeding (longer gears for same torque). This is highlighted in the grey box, at speeds below 2500 rpm (~850 rpm engine speed), where only a positive BSG contribution is recorded, while regeneration is avoided in this area. On the electric side (right plot), it can be seen that max electrical power reached is about 10 kW in motor mode, with a 250A maximum current. During different operations, it was found that the battery voltage ranges from 37 to 51V, which corresponds to a 1% to 99% SOC range and that the charge-sustaining threshold is adjusted according to the driver request. In particular, 39% SOC when driving between 40 and 60 km/h, 18% SOC when driving between 90 and 100 km/h, and finally 9% SOC when driving around 120

km/h. As far as the boosting function is concerned, the BSG assists the ICE at high speed / high load to increase power as shown in Figure 36. This picture shows the ICE full-load torque and power (blue line), and the combined output (red line). The boosting function has some restrictions, such as it is maximized for gas pedal above 40% and during constant speed driving it is enabled for speeds equal or lower than 40 km/h. To summarize, all the main findings of this activity will be used as input for vehicle modelling.

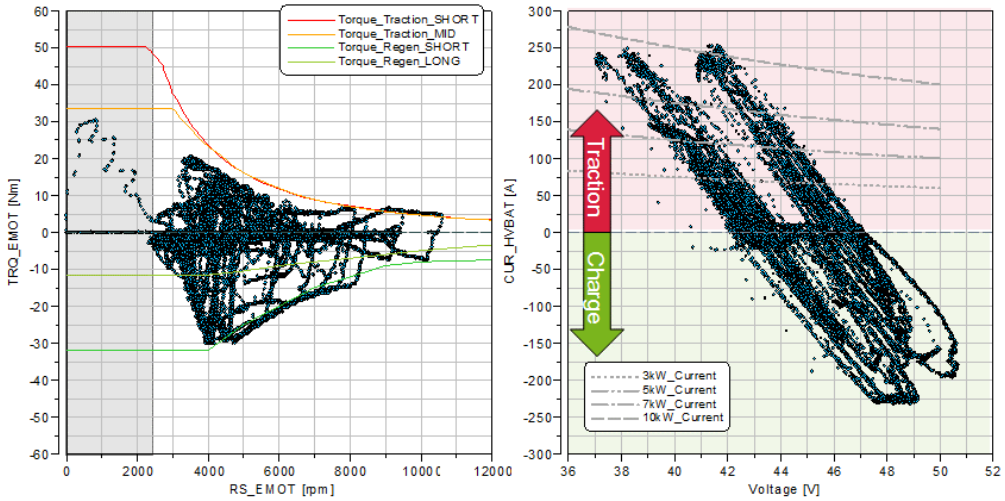


Figure 35: BSG (left) and 48V Battery (right) operating points recorded during testing

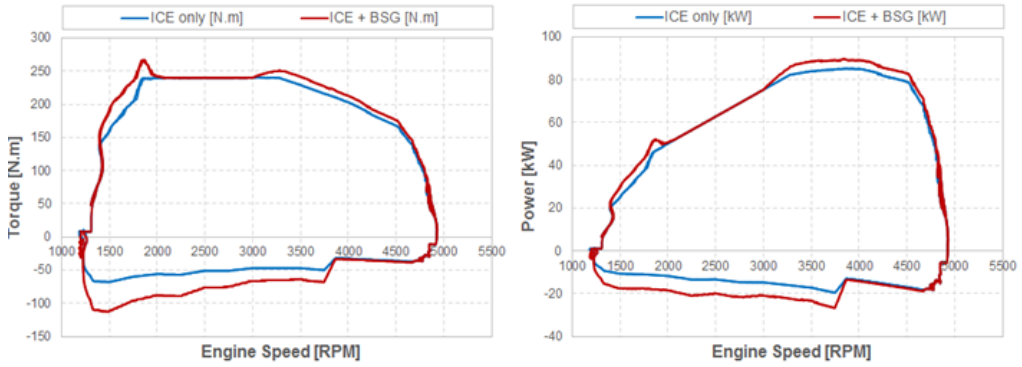


Figure 36: ICE and BSG full load torque (left) and power (right) for Vehicle 1

## 2.5.2 Vehicle 2 Analysis

This section analyses the powertrain behavior of P0-P2 Gasoline Vehicle 2, analyzing measurement from the ICE, the EM, the HSG and the HV battery.

As previously explained the standing-start test must be performed on the road, considering different working conditions of battery SOC, driver power request and selected driving mode. In Figure 37 the reader can find the most important signals used for the investigation of vehicle behavior, and for the characterization of the ICE, the EM, the HSG and the HV battery. In particular, the top plot illustrates the HV battery current and the EM torque: during charging phases positive current and negative torque are measured, while during discharging

phases negative current and positive torque are measured. Moreover, the accelerator pedal position is shown along with the HV battery SOC and finally vehicle speed and the EM rotational speed. In the bottom plot the torque from the two machines is shown, together with the activation status of the HSG (1 is for motor and -1 for generator). Lately, the rotational speeds are reported, while the last subplot illustrates vehicle speed. The standing-start maneuver was carried out at 50% accelerator pedal request, at high SOC (60%), in EV mode (solid line) and Hybrid Mode (dashed line): this test is reported on the left side of Figure 37. If the vehicle is in EV mode, the ICE does not provide any torque while the EM has to give the power request. On the contrary, if driving in HEV mode, the ICE is turned working at almost constant load and speed (2000rpm/80Nm), while the EM supports the maneuver with an additional boost at very low torque (>20Nm). Similarly, the right side of Figure 37 reports the output of vehicle acceleration at 100% accelerator pedal request, in EV mode (solid line) at 60% SOC and Hybrid Mode (dashed line) at 15% (low) SOC. It is clear that the higher power request requires similar behavior, regardless of the battery SOC, hence, the EM immediately propels the vehicle while the ICE progressively revs up to a constant torque value of about 125Nm. During the load point shift operation, the road load is followed by adjusting the EM load. When the P2 clutch is closed, the two rotational speeds (dashed lines) are synchronized, as reported in the bottom part of Figure 37.

As already introduced for Vehicle 1, the elasticity maneuvers were carried out on the chassis dynamometer. Different conditions were tested such as different speed range, driving mode, HV battery SOC and power request. The following plots will report results coming out from a couple of tests, with the aim of highlighting the key of this type of procedure. To this extent, the left part of Figure 38 depicts the 40-80km/h elasticity test performed in EV mode, at 100% accelerator pedal (solid line) and 50% accelerator pedal (dashed line). In the acceleration in EV mode, at 100% pedal request, the ICE is turned on delivering a constant torque, while the EM supports the ICE and gradually adjusts its torque output. On the contrary, in the acceleration at 50% pedal request, more time is required to reach the target 80km/h speed: the whole maneuver is performed in pure electric mode and lower EM torque and lower battery current are requested. The second elasticity test reported, was carried out in HEV Mode at low battery energy SOC (~10%), going from 60 km/h to 100 km/h, with two different accelerator pedal positions, as shown on the left of Figure 38. A longer time (35s) is needed to reach 100km/h at 50% pedal, while only 8s if performing the acceleration at 100% accelerator pedal. Because battery SOC is low, the ICE is turned on and the EM provides a decreasing contribution until the ICE torque reaches the target value of 80 Nm at 50% pedal and 125 Nm at 100% pedal.

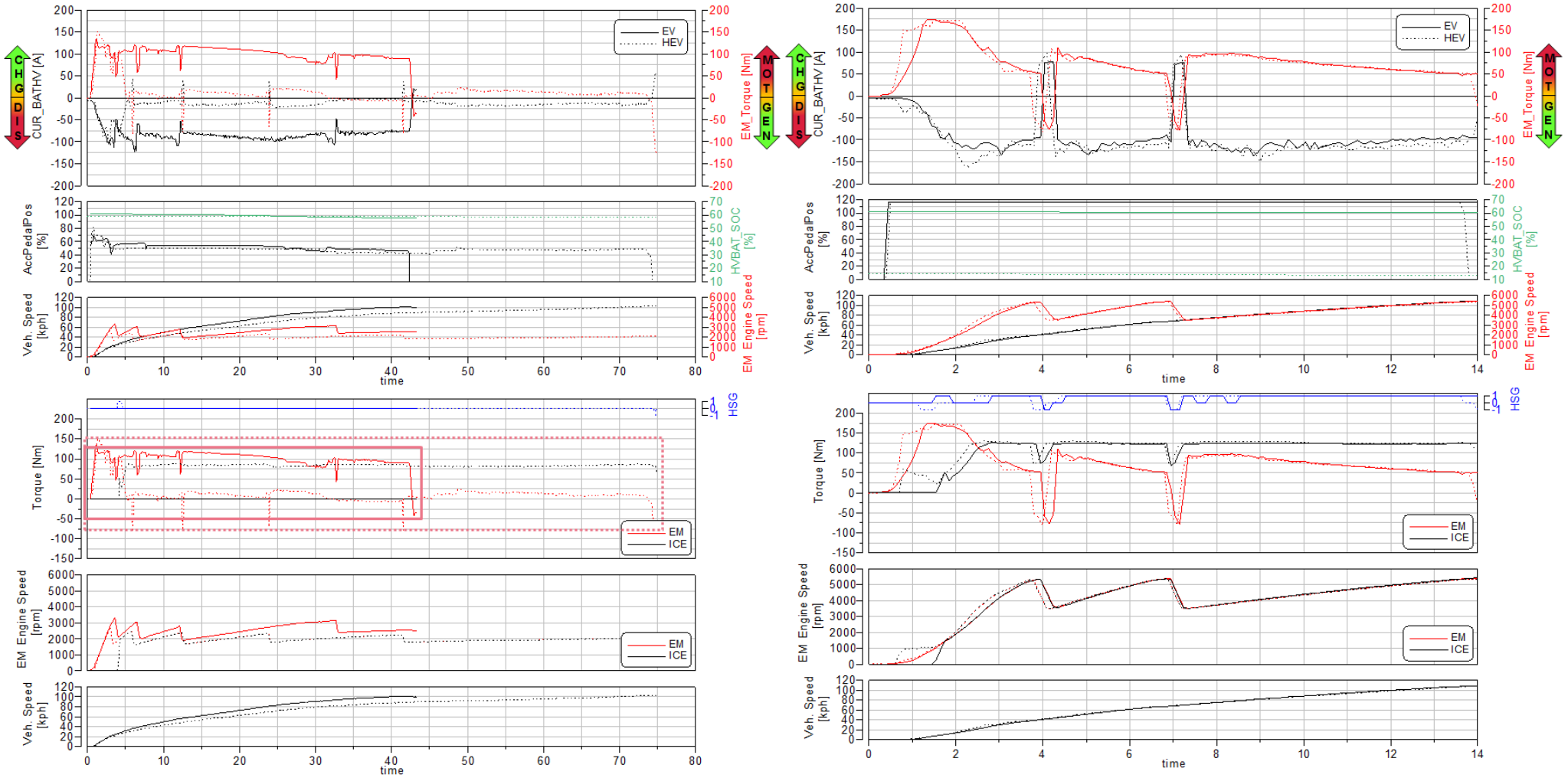


Figure 37. Main measurements for 0–100km/h test at 50% (left) and 100% (right) accelerator pedal, in EV Mode (solid line) and Hybrid Mode (dashed line)

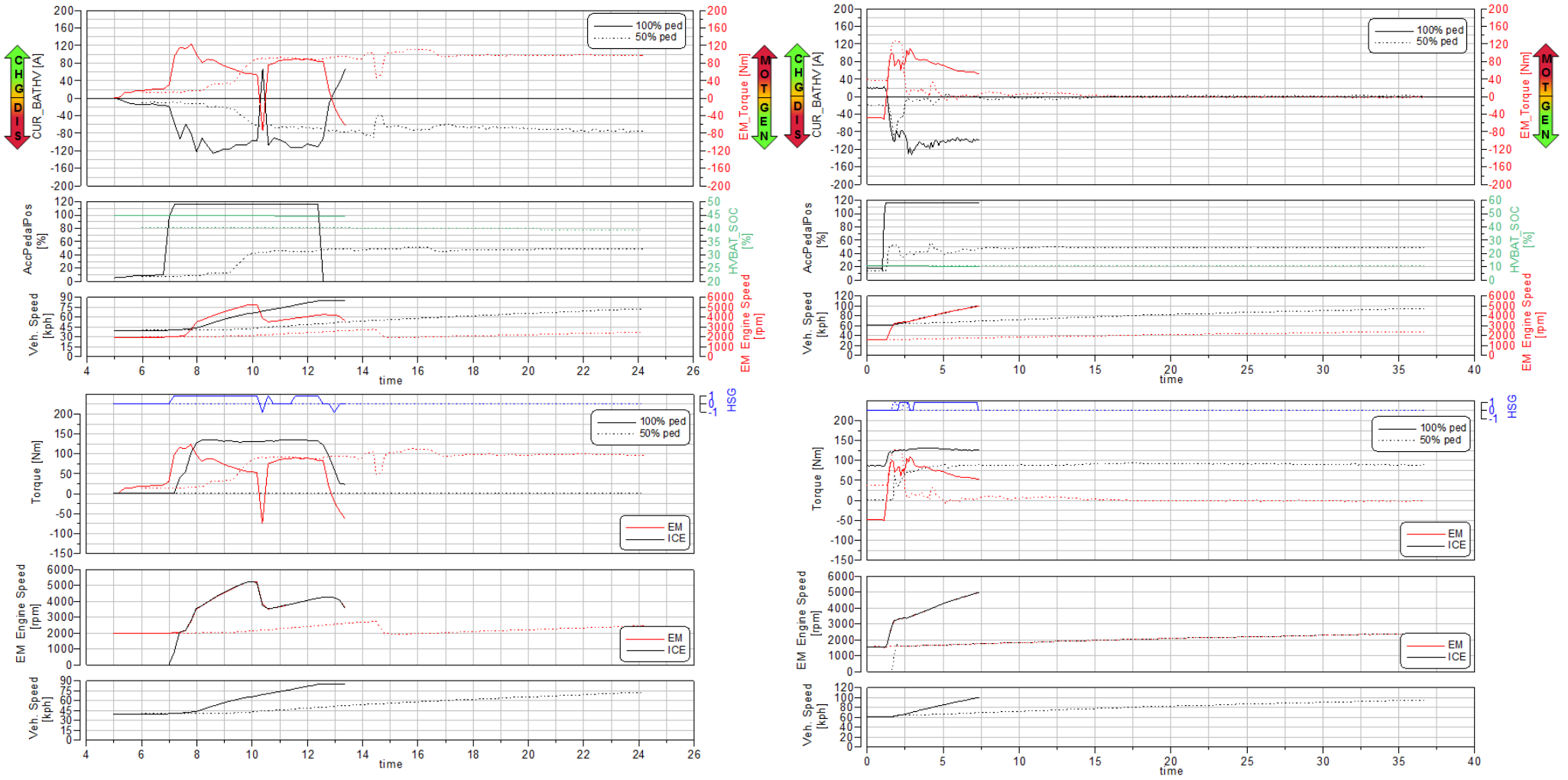


**Figure 38. Main measurements for 40–80km/h Elasticity test in EV Mode (left) and 60–100km/h Elasticity test in Hybrid Mode at low SOC (right), at 100% accelerator (solid line) and 50% accelerator (dashed line)**

With the aim of testing the vehicle under ordinary situations, the critical mission tests were carried out. Firstly, the constant speed driving was performed to investigate the charge sustaining mode, at low battery SOC. In the left part of Figure 39, the main signals recorded from the EM and the ICE are shown: driving at constant 30km/h speed, the ICE is turned on by the HSG before 150s (the rotational speeds are synchronized). This is due to the fact that HV battery SOC reaches the lowest threshold of about 10.5%; therefore, the EM has to recharge the battery by working as a generator. As far as the ICE is concerned, it delivers a constant torque of approximately 80 Nm. The switch between the two working modes is highlighted from the duality between battery current and EM torque. Moreover, steady driving at 120km/h speed is reported on the right side of Figure 39. It can be noticed that at high speed, the EM cannot be used as a generator, hence, the ICE has to provide torque requested at the wheels. The engine propels the vehicle at with a stable torque of 90 Nm, while the electric motor is off.

After the steady state driving test, the deceleration tests were carried out and outcomes of active braking and sailing will be addressed in the following lines. These tests are performed to investigate the interaction between vehicle speed, brake pedal position and battery SOC. In this regard, Figure 40 shows the output of an active braking procedure, starting at 100km/h, both in EV mode (solid line) and Hybrid mode (dashed line). The brake pedal position is displayed in the second subplot showing a similar behavior, regardless of the driving mode and the battery SOC. The battery is constantly charged via the EM, at maximum constant torque of 175Nm, while the measured HV battery current is close to 120A. Additionally, Figure 41 illustrates an active braking procedure, starting at 120km/h, both at 50% brake pedal (solid line) and 75% brake pedal (dashed line). When braking at 50% pedal, the HSG shortly acts as a generator to charge the battery; and, before turning the engine off, the HSG works as a motor to speed the ICE at 1500rpm. This can help during a possible change of mind of the driver. On the other side, a more energetic braking (75%) requires the ICE to go suddenly off. In both situations, the mechanical torque absorbed by the EM is about 175Nm.

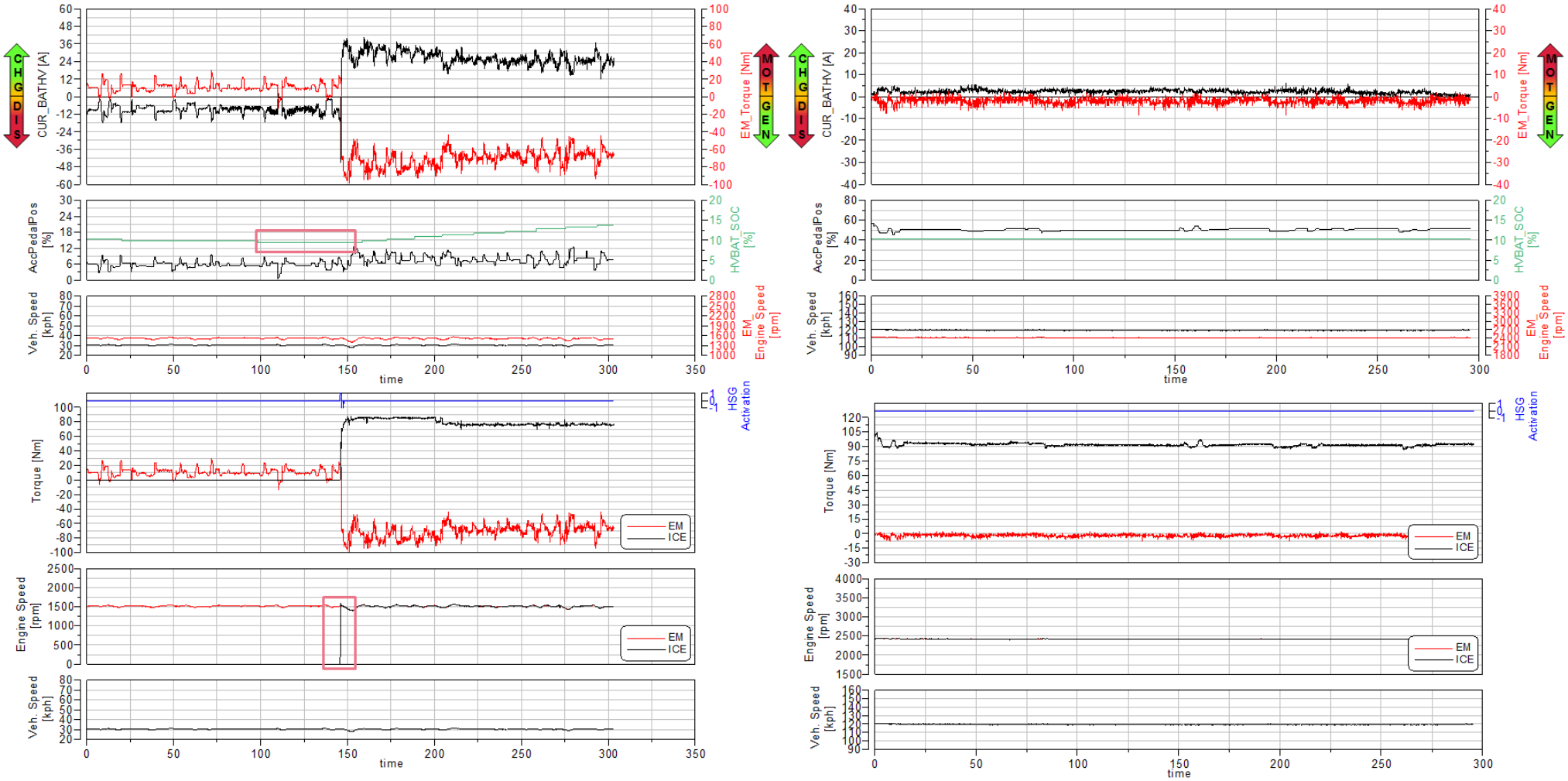


Figure 39. Main measurements for 30km/h (left) and 120km/h (right) Steady State driving in Hybrid Mode

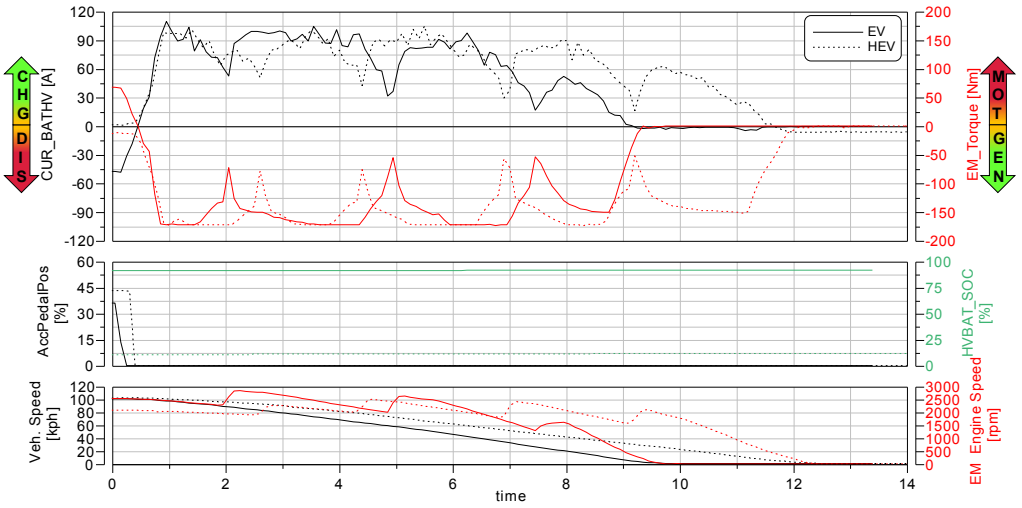


**Figure 40. Main measurements for Active Braking from 100km/h, in EV Mode (solid line) and Hybrid Mode (dashed line)**

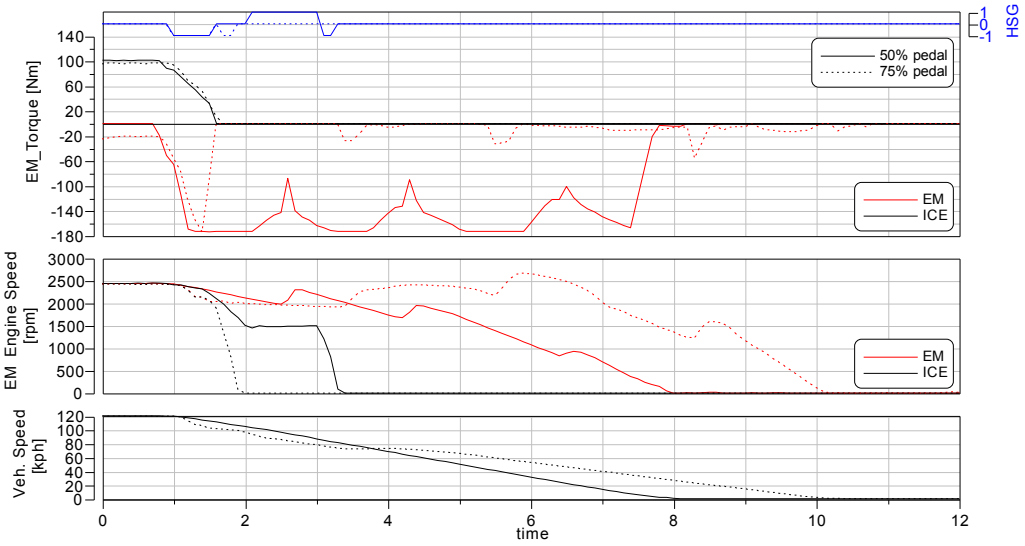


**Figure 41. EM and ICE measurements for Active Braking from 120km/h, at 50% brake (solid line) and 75% brake (dashed line)**

To conclude with the critical mission test, the sailing functionality is analyzed: Figure 42 depicts a situation of sailing at low speed of 50km/h, both in EV mode (solid line) and Hybrid mode (dashed line). Regardless of the HV battery SOC level, the two decelerations are performed in the same way: only the EM is used and it works as a generator to recharge the battery. Additionally, in Figure 43 the sailing procedure from 100km/h is shown, in both Hybrid mode (solid line) and EV mode (dashed line). It can be noticed that the ICE is used in Load Point Shift to charge the battery until the requested torque is above 70Nm. Therefore, the ICE goes off and the EV mode is automatically engaged. As seen before, the HSG prevents the ICE from stopping for a short amount of time with the aim of covering a possible change of mind. Finally, sailing in EV mode is completely performed with the EM as a motor even during the deceleration.

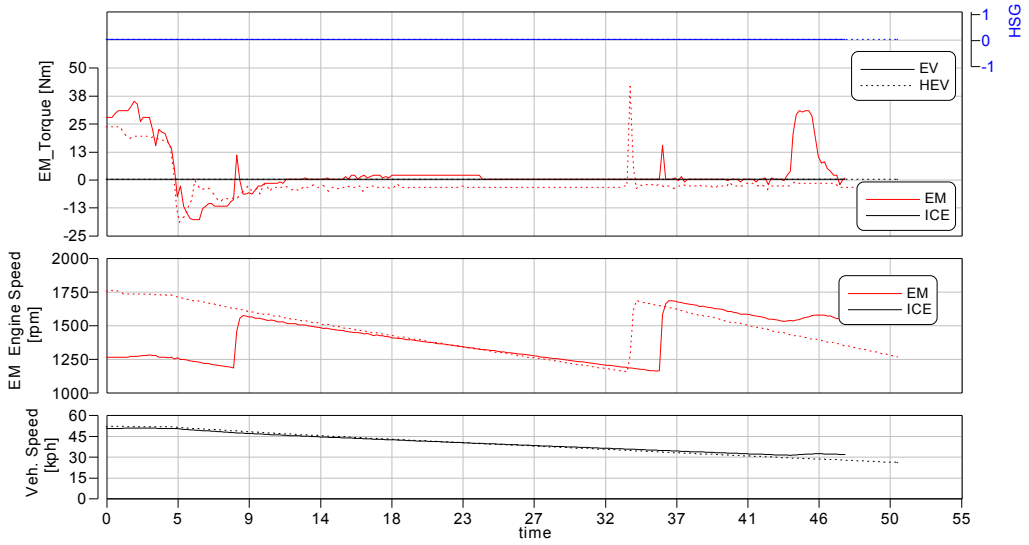


**Figure 42: EM and ICE measurements for 50-30km/h Sailing test in EV mode (solid line) and Hybrid mode (dashed line)**

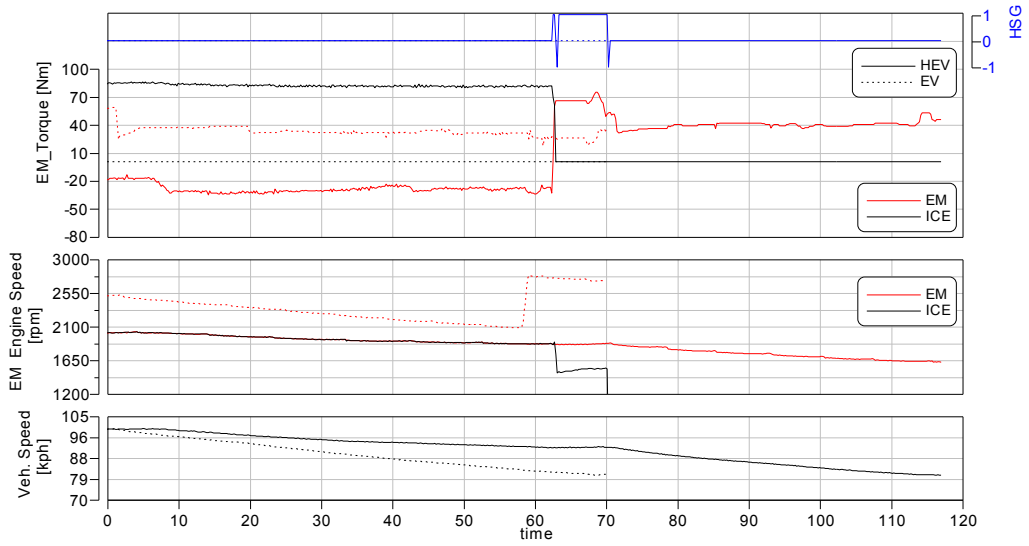


**Figure 43: EM and ICE measurements for 100-80km/h Sailing test at high SOC, in Hybrid Mode (solid line) and EV Mode (dashed line)**

To summarize the activity carried out on Vehicle 2, the same methodology was applied to evaluate the capabilities of a P0-P2 architecture; data gathered during the characterization tests and the standard driving cycles are merged for detecting the control logics behind the powertrain behavior. To this regard, Figure 44 shows that the P2 EM is mainly used above 1000 rpm, in both working modes, as is highlighted by the grey box. Particularly, the positive motor torque is provided until maximum rotational speed, since it has to provide the pure electric driving; on the other side, the recuperation torque is mainly absorbed in the constant torque region, with speed below the base speed. As for the HV battery (right plot), the maximum electrical power reached is about 60 kW in motor mode, with a 175A maximum current. Generally, the battery voltage ranges from 300 to 400V, and the highest current tis reached in traction mode rather than in

charge mode, as it was already seen from the lower torque measured from the EM communication network.

Regarding the Hybrid Mode request, i.e. the cooperation of both the ICE and the EM, it was found out that it is regulated with a threshold-vehicle-speed map (Figure 45). It depends on the torque requested at the wheels and of the battery SOC. Looking at the iso-Torque curves (a) subplot, it can be noticed that for a given value of torque, the higher the battery SOC level, the higher the vehicle speed threshold to enable the HEV mode and turn on the ICE. On the other side, looking at the (b) subplot, for a given value of battery SOC, the higher the torque requested, the lower the vehicle speed required for the transition.

In order to understand the EMS control logic, the driving mode characterization is performed. Therefore, in Figure 46 the torque requested at the wheels during the different driving modes, gathered during the complete experimental campaign, is plotted; in particular, the pure EV drive is reported with green markers, the regenerative braking with black markers, the LPS operation (charge mode) with blue markers and the boost is highlighted with red markers. The left plot shows that below 25 km/h only the EV drive and the regenerative braking are enabled and the whole speed range can be covered by the EV drive, while the ICE is often used in LPS and Boost mode, not only for vehicle start-up. On the right plot, the same operating points are reported as a function of the product between vehicle speed and acceleration, showing that the ICE-on operation is enabled for higher values of speed and acceleration, while the pure EV drive takes care of the smooth driving conditions.

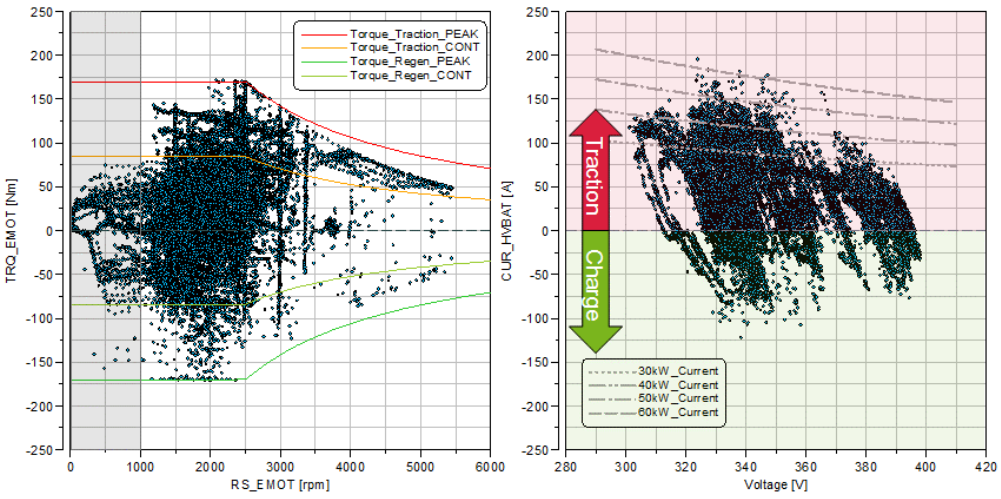


**Figure 44: P2 EM (left) and HV Battery (right) operating points recorded during testing**

Considering the ICE operating conditions, its working strategy was mapped via the analysis of portions of tests in which only positive power at the wheels was requested. In Figure 47, the ICE power in Hybrid Mode is depicted, as a function of the vehicle speed, and the gear engaged. It can be highlighted a linear relationship between power and speed during the Load Point Shift operations, this is true either in battery charging (top) or in supporting the EM (bottom). The

engine is controlled to work in constant load mode, while the EM load is continuously adjusted.

In conclusion, the main findings of this analysis will be used as input for vehicle and powertrain modelling, as explained in the next Chapter.

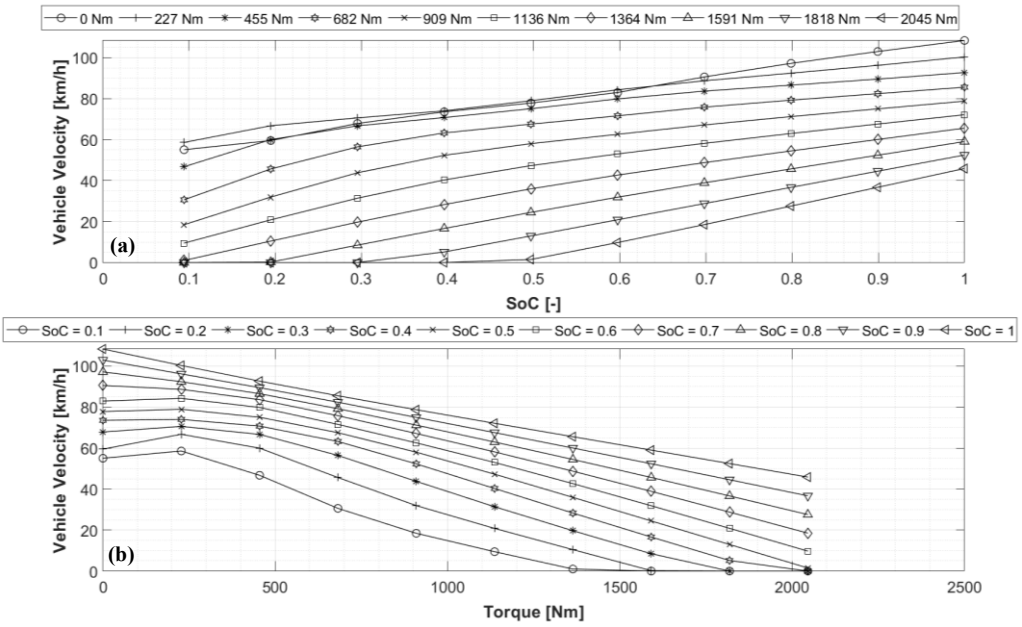


**Figure 45: Hybrid Mode activation map: threshold vehicle speed function of torque at wheels (a) and battery SOC (b)**

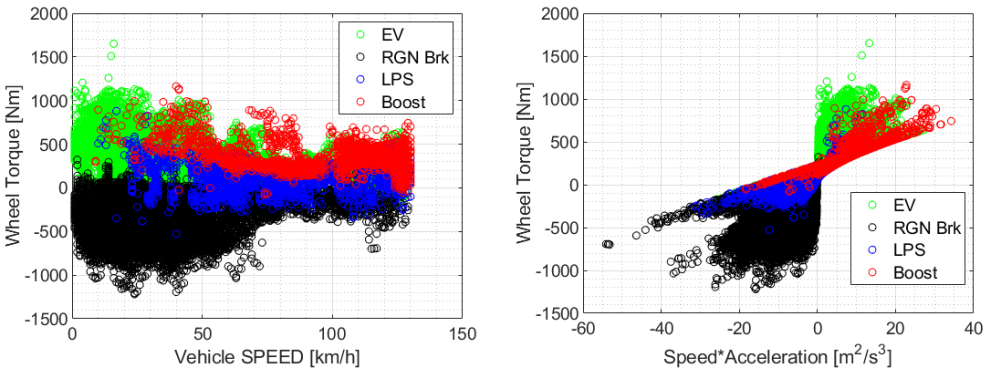


**Figure 46: Driving Mode split operating points as a function of vehicle speed (left) or speed times acceleration (right) and torque requested at the wheels**

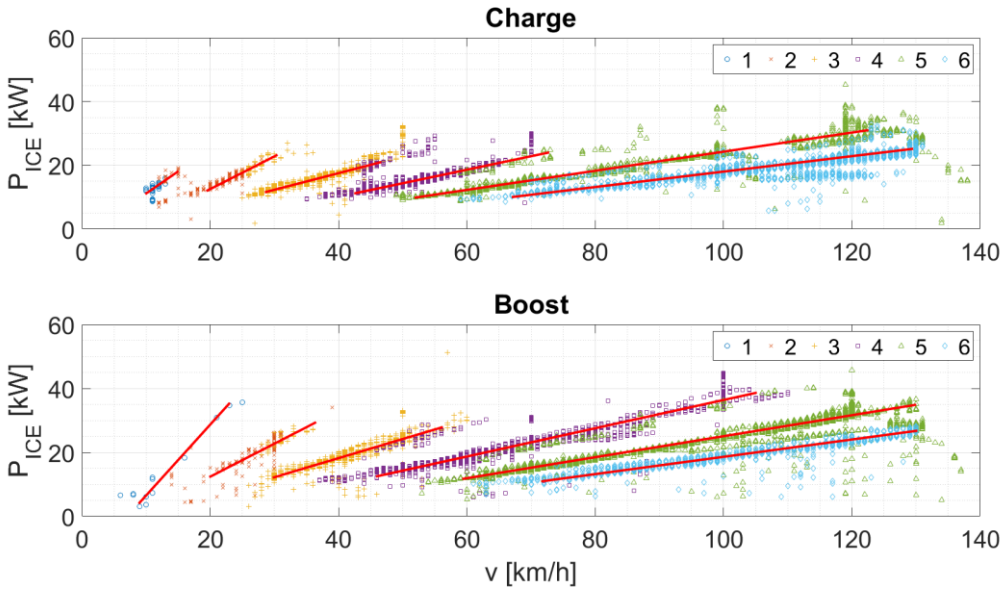


**Figure 47: ICE Power generated versus vehicle speed during Load Point Shift in Hybrid Mode, for each gear: battery charging (top) and boosting (bottom)**

### 2.5.3 Vehicle 3 Analysis

This section analyses the powertrain behavior of P2 Diesel Vehicle 3, analyzing measurement from the ICE, the EM and the HV battery.

Before illustrating the results coming from the experimental campaign, it is worth to mention that on this vehicle there were some issues in acquiring the HV battery SOC, which results to be an essential variables for the battery and EMS reverse-engineering. For this reason, it was decided to create a SOC signal starting from the dashboard reading; this means that the SOC signal involved in the analysis is a relative value, based on the approximation of the displayed value. In order to estimate the battery SOC with manual reading from dashboard, the actual HV battery current measurement was used. As reported in [79] , the Modified Coulomb Counting Method was adopted as a way to estimate the battery energy content by means of a corrected current flowing in and out of the battery. Normally, the Coulomb counting method uses the discharging current and integrates this current over time in order to estimate the SOC, as reported in the following equation:

$$SOC(t) = SOC(t-1) + \frac{I(t)}{Q_n}\Delta t \qquad (2\text{-}2)$$

However, numerous factors affects the accuracy of Coulomb counting method such as temperature, battery history, discharge current, and cycle life [80]. To account for all these factors and for the approximation made by the displayed SOC value, the Modified Coulomb Counting Method calculates the corrected current as follows:

$$I_c(t) = k_2 I(t)^2 + k_1 I(t) + K_0 \quad (2\text{-}3)$$

Where $k_2$, $k_1$ and $k_0$ are constant values obtained from experimental data. Then, the modified current can be used to estimate the SOC as follows:

$$SOC(t) = SOC(t-1) + \frac{I_c(t)}{Q_n}\Delta t \quad (2\text{-}4)$$

In this regard, Figure 48 shows the assessment process performed over a series of three consecutive NEDC cycles (bottom plot), which were performed for TA approval procedure simulation. In this picture, the top plot shows the base measured battery current (black) and the corrected one (red), according to [79]; the central plot shows the estimated SOC (green line) and the experimental data gathered from manual reading (black markers). By performing a RMSE minimization analysis, the best coefficient for SOC estimation were found and reported in the following table:

Table 10: Modified Coulomb Counting Method coefficients

| $K_0$ | $K_1$ | $K_2$ |
|---|---|---|
| 0.100007 | 0.881808 | 6.658E-05 |

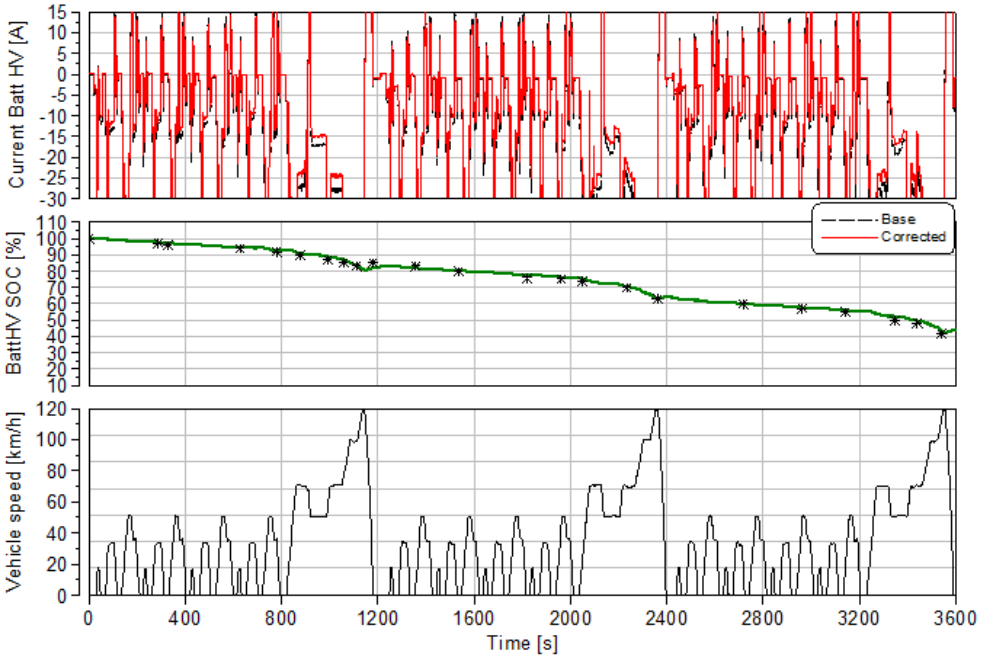


Figure 48: Modified Coulomb Counting Method application for HV Battery SOC estimation over three NEDC cycles

Before moving to the characterization and critical mission test explanation, it has to be mentioned that during the TA procedure simulation it was found that this PHEV behaves in a dual mode: on one side, the CD mode is always activated until the battery depletes a net energy content equal to 9.3kWh. After that, the vehicle

runs in pure CS mode, using both the EM and the ICE to recharge the battery, as illustrated in Figure 49. As it can be noticed from the red dashed line, the first ICE cranking was detected when the battery energy output reached 9.3 kWh, which corresponds to the declared net battery energy content. Additionally, in the bottom plot the powertrain operating points are displayed as a function of torque requested at the wheels and HV battery SOC; as highlighted from the red (boost mode) and blue (Load Point Shift mode) markers, the ICE works only in a 6% to 15% SOC range, while the majority of the cycles is performed in pure EV mode (green markers), other that in regenerative braking mode (black markers). Of course, a detailed explanation of the EMS logic will be given at the end of this section, considering the outcomes of the whole experimental campaign. Due to this finding, the following test will be related to high SOC cases, while the CS characterization will be provided on the base of the driving cycles performed as usual during the test campaign.

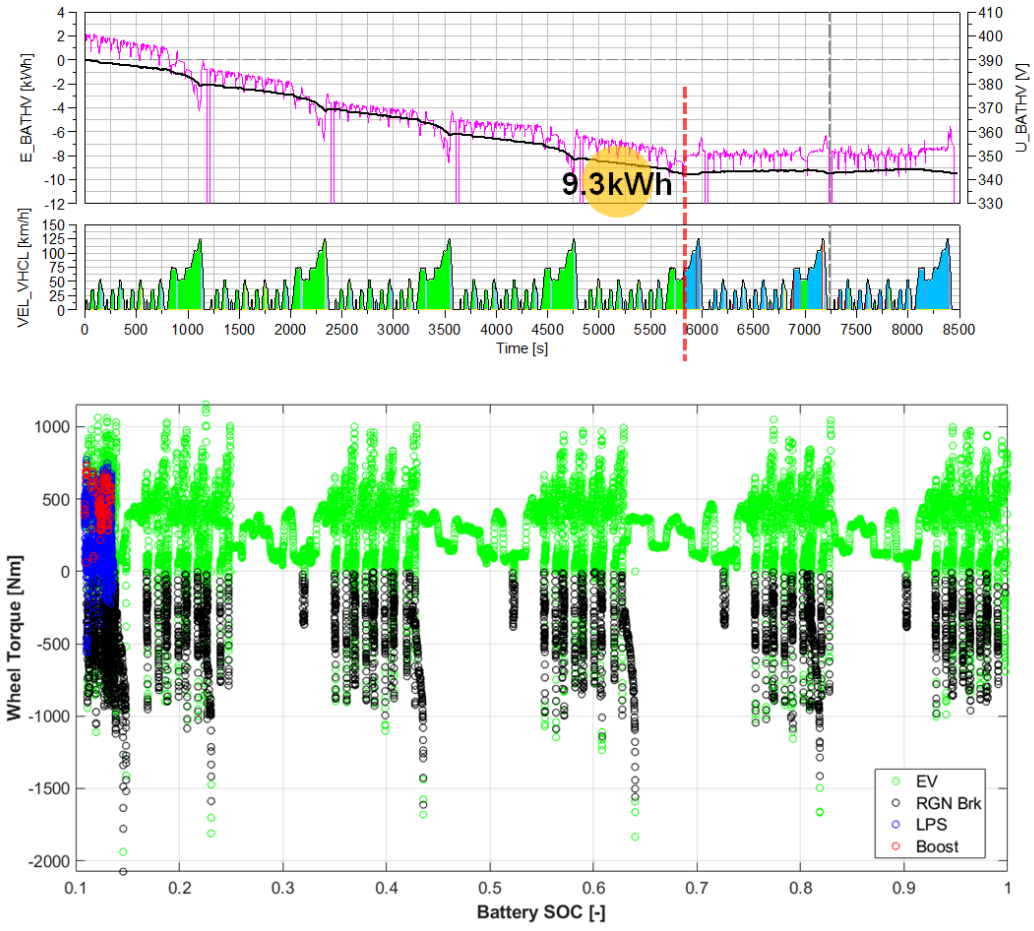


**Figure 49: NEDC TA procedure simulation: HV Battery energy and voltage and vehicle speed (top) and driving mode split (bottom)**

As already introduced for Vehicle 1 and Vehicle 2, the test case underwent a series a specific test. For the sake of brevity, few maneuvers will be reported in order to deeply analyze the powertrain EMS, later in this section. As usual, the elasticity maneuvers were carried out on the chassis dynamometer under different conditions of speed range, driving mode, HV battery SOC and power request. As

an example, Figure 50 depicts the 40-80km/h elasticity test performed in EV mode, at 100% accelerator pedal position. The kick-down acceleration, highlighted with the blue line in the third sub-plot, requires the ICE to be turned on, as soon as the accelerator is depressed at a very high rate. In this situation, the EM keeps providing a positive traction torque close to its maximum target peak value of 440Nm, supporting the ICE in propelling the vehicle, as shown in the first sub-plot. The two machines rotates at a synchronous speed, as can be noticed from the black line and red area overlapping in the second plot. For the sake of completeness, the elasticity maneuver was performed under different conditions; in all of them the ICE was turned on to assist the acceleration, due to the sudden increase in accelerator pedal position.

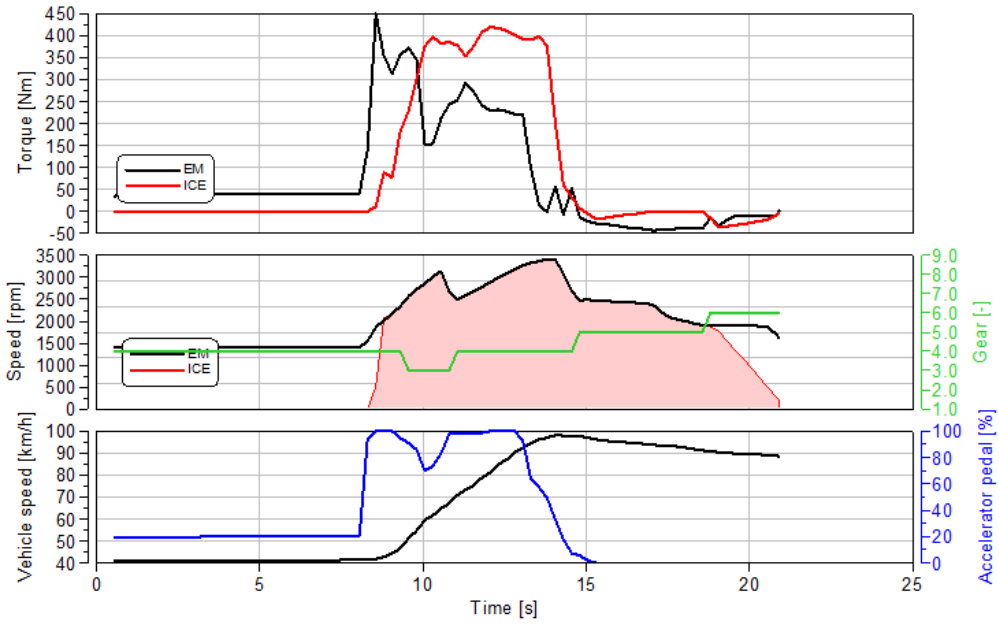


Figure 50.Main measurements for 40–80km/h kick-down Elasticity test in EV Mode

With the aim of testing the vehicle under ordinary situations, the critical mission tests were carried out. At first, the constant speed driving was performed to investigate the powertrain response to variable road resistance, at high battery SOC. For this type of analysis, the chassis dynamometer was set to fixed speed mode in the so-called *Ramp-Up* test. The aim is to force the vehicle to run at a constant speed, imposed by the dyno, while performing a steady accelerator pedal increase from 0 to 100%, in order to simulate a different but gradually increasing driving resistance. An example is shown in Figure 51: the vehicle speed is kept constant at 80 km/h, while the driver performs a 0 to 100% accelerator pedal sweep (bottom plot). During this test performed at high SOC, the vehicle runs in pure EV mode until the pedal position reaches 60%; later, as highlighted from the red curve and the red area in the second plot, the ICE is turned on and works together with the EM in boost mode, at 400Nm constant load. For the sake of completeness, the steady driving test was performed at different vehicle speed, from 10 to 120 km/h: generally, the ICE is turned on around 60% accelerator pedal position.

Moreover, data recorded along this type of tests were collected to characterize the hybrid mode switch in terms of vehicle speed and power request, as illustrated in Figure 52. This picture is the results of the constant speed experimental campaign performed on the dyno; it can be noticed that, on average, the pure electric driving is allowed for a powertrain power request up to about 80 kW, while, later, the increased load is supported by the ICE. As illustrated in both plots with the striped area, the hybrid mode characterization was possible only for vehicle speed above 50 km/h due to chassis dyno power limitations. More in details, on the left plot, the separate and combined EM and ICE contributions are shown, along with the selected gear. On the right side, the bottom green area below 80kW refers to the pure EV driving, while the upper light-blue are refers to HEV mode driving.

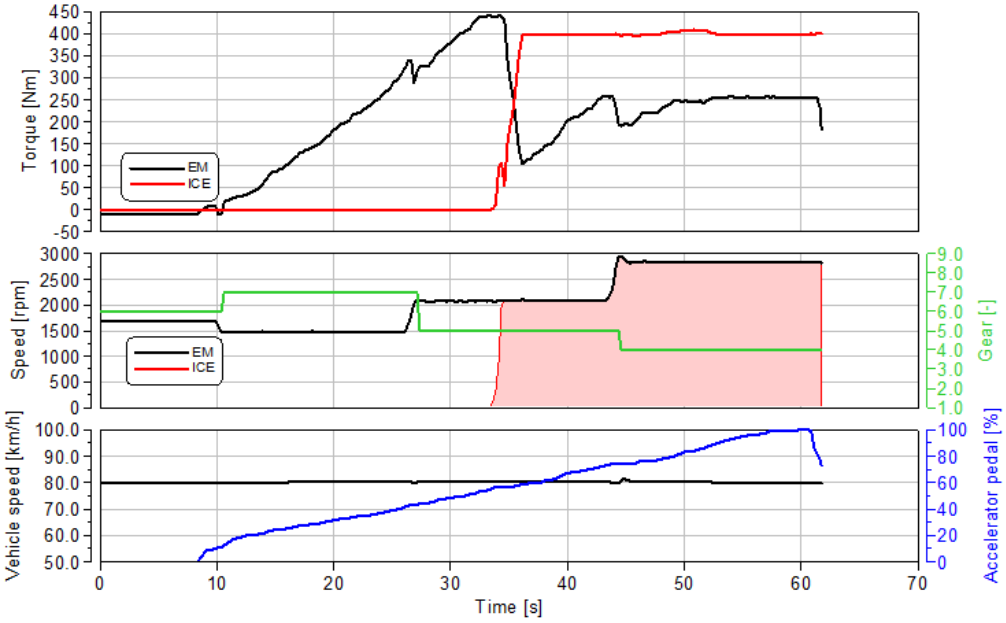


**Figure 51: Powertrain torque (top), speed and gear (central ) and vehicle speed with accelerator pedal position (bottom) during a constant driving test**

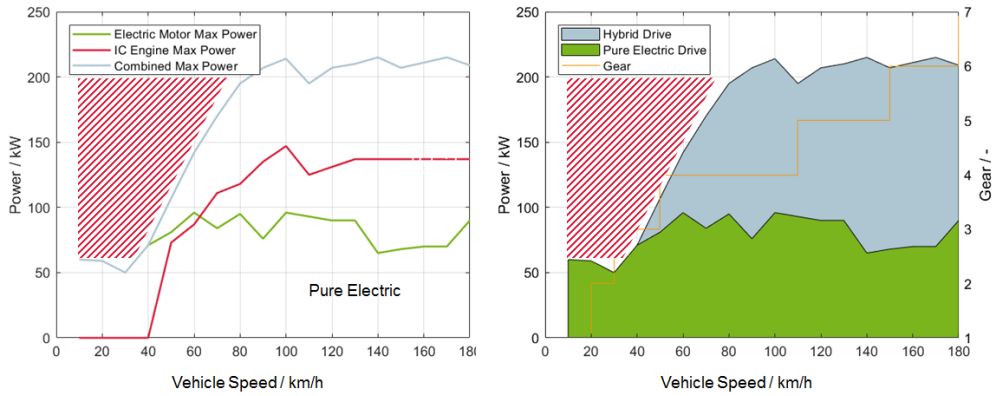


**Figure 52: Hybrid Mode switch characterization by constant speed driving**

After the steady-state driving test, the deceleration tests were carried out in order to investigate the interaction between regenerative and the conventional mechanical braking. More in details, the braking system behaviour was

investigated over a series of imposed deceleration, performed at different deceleration rate. As illustrated in Figure 53, the braking energy from the electric motor (red line) and the hydraulic braking enegy on the rear (blue) and front (green) axle, measured directly from the test bench, were aquired during the procedure. In addition, the accelerator pedal is plotted with the vehicle speed and deceleration rate. As it can be seen, the deceleration rate ws gradually increased up to -2.5 m/s$^2$. Therefore, the vehicle operating points were studied in terms of speed and acceleration.

As a result, Figure 54 depicts the braking power ratio as function of vehicle acceleration and speed, collected during different decelerations. More in details, the powertrain regenerative (only rear) braking contribution over the total braking power, i.e. powertrain and hydraulic, is investigated: it is clear that the regenerative braking effect is relevant in the driving cycle area where low deceleration are taken into account. As a matter of fact, the regenerative power contribution accounts for almost 80% to 90% of the total braking request. However, at higher decelerations rates, the impact of regenerative braking is smaller, but almost constant as noticed throughout the test campaign.

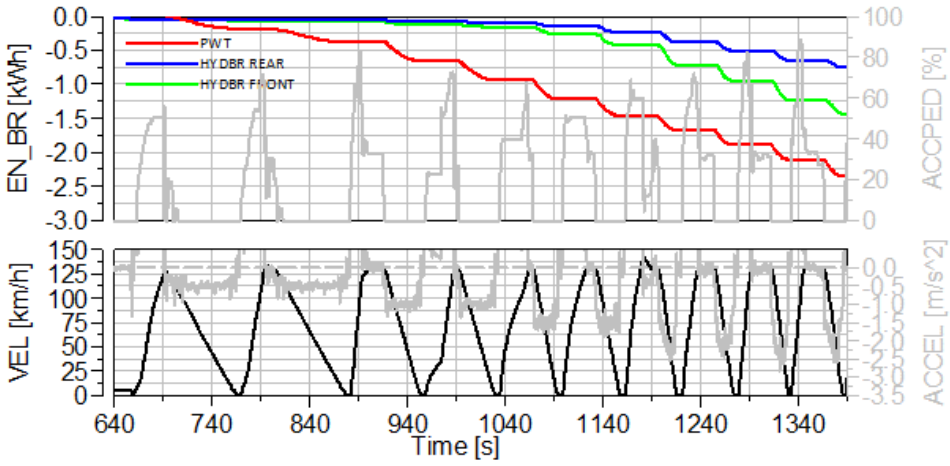


Figure 53: Main signals recorded during active braking test

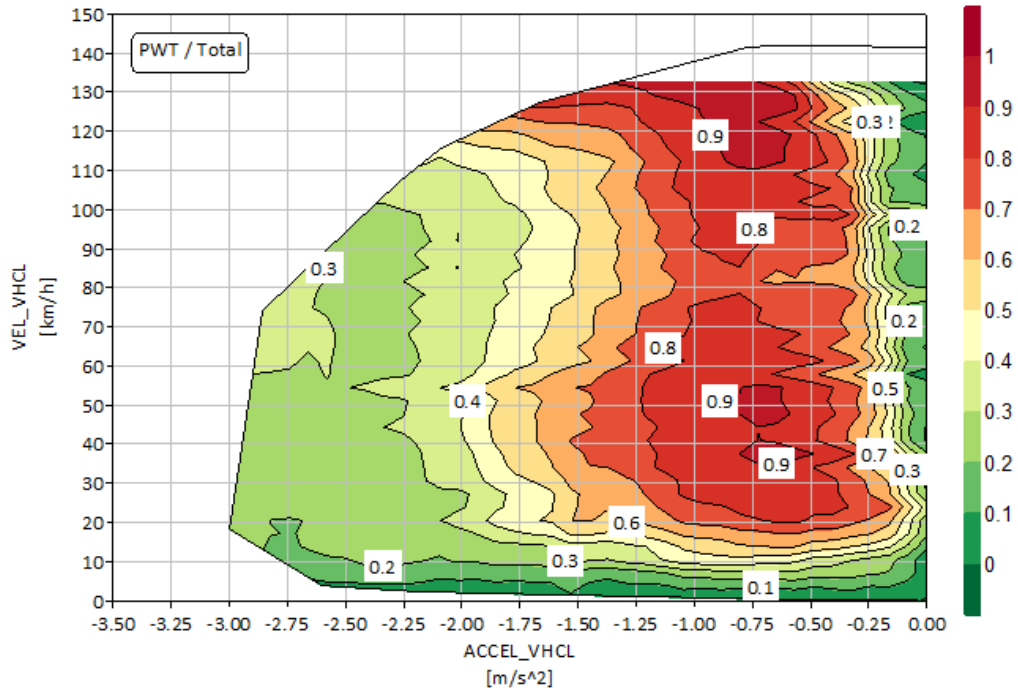


Figure 54: Brake blending ratio: regenerative (PWT) over total braking power

In conclusion, the same methodology was applied on Vehicle 3 in order to understand the capabilities of a P2 architecture. The complete set of data gathered during both characterization tests and driving cycles are useful for powertrain and EMS characterization. To this extent, Figure 55 illustrates that the P2 EM is mainly used above 900 rpm, in both working modes, as is highlighted by the grey box. In particular, the regenerative effect is absent below 400 rpm and above 2000 rpm; while it is reduced up to 900 rpm and mainly used in the central900-to-2000rpm speed area. On the motoring side, the EM is widely used over the entire speed range since this vehicle has nearly no speed limitation in pure EV mode. As a consequence, the positive EM working points reach the maximum peak curve, highlighted by the top red line. As far as the HV battery (right plot) is concerned, the maximum electrical power reached is about 100 kW in motor mode, with a 280A maximum current. During its operation, the battery voltage ranges from 320 to 410V, and the highest current tis reached in motor mode rather than in regenerative mode, as also seen form the torque-speed analysis.

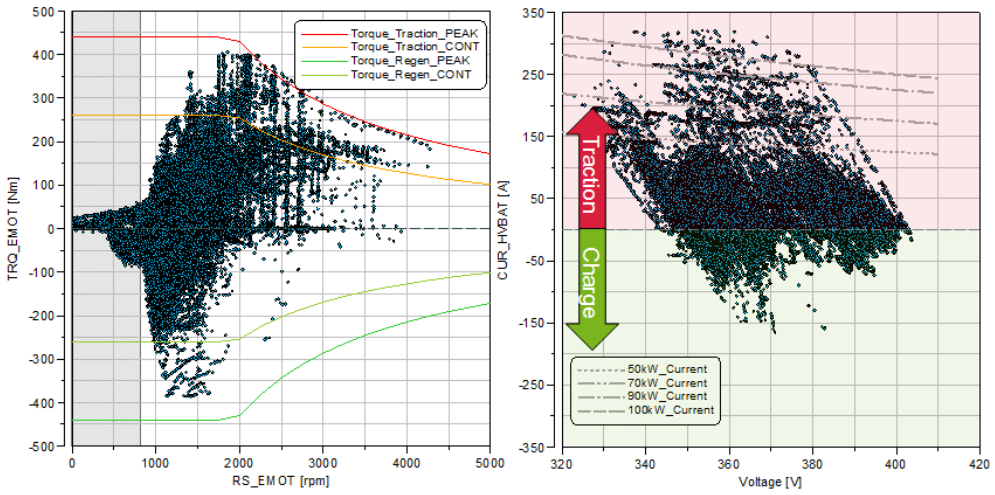


**Figure 55. P2 EM (left) and HV Battery (right) operating points recorded during testing**

Regarding the Hybrid Mode request, it has already been demonstrated that this vehicle operates in a dual mode, hence a direct SOC dependency was not found in the switch between the EV and HEV driving mode request. To confirm this finding, Figure 56 shows the outcome of the reverse engineering of the Hybrid mode request from the HCU. More in details, the plot on the left shows the dependency of the vehicle speed threshold for turning on the ICE, as a function of vehicle torque wheel request and battery SOC. As expected, the experimental data gathered during the ICE-on event have do not show any trend with the battery SOC, while it is clear that the higher the torque request the lower the vehicle speed threshold required for the driving mode transition. On the left side of Figure 52, the same experimental data are modelled in terms of wheel power request threshold, as a function of the product between vehicle speed and acceleration and battery SOC. In this case, a linear relationship was found for the power request; hence, the higher the speed and acceleration request from the driver side, the higher the power at which the transition takes place.

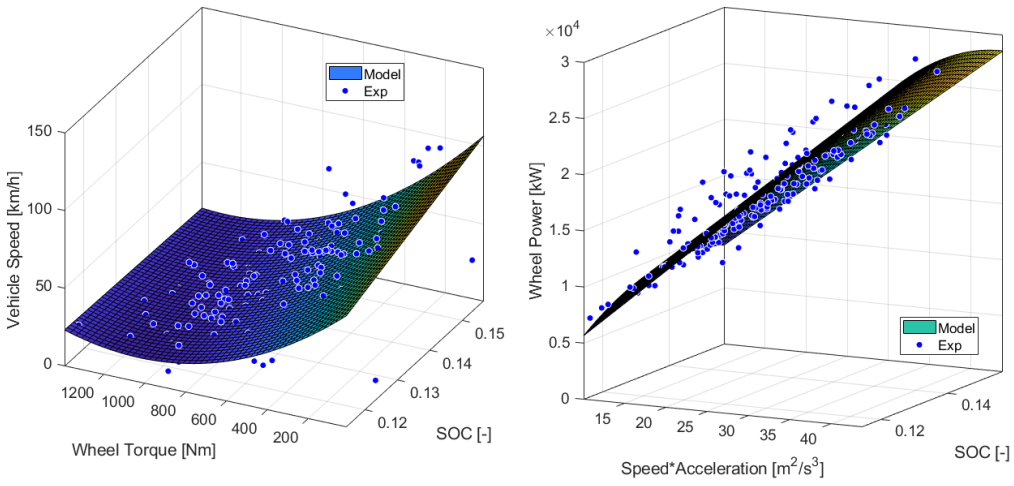


**Figure 56: Hybrid Mode Request: threshold vehicle speed function of torque at wheels and battery SOC (left) and threshold power at the wheels function of speed times acceleration and battery SOC (right)**

As previously illustrated in Figure 49, the driving mode characterization is proposed to understand the EMS control logic. Hence, the left plot of Figure 57 shows the wheel torque request as a function of vehicle speed: it can be seen that below 20 km/h only the EV drive and the regenerative braking are enabled. Furthermore, the EV drive is allowed over the entire speed range, while the ICE is on mainly in LPS mode, which means for battery charging through the EM and for propelling the vehicle. The boost functionality is generally enabled at high torque and low vehicle speed to launch the vehicle and overcome the turbo-lag effect. On the right plot, the same operating points are reported as a function of the product between vehicle speed and acceleration, showing that the ICE-on operation is enabled for higher values of speed and acceleration, while the pure EV drive takes care of the smooth driving conditions.

Finally, the LPS working strategy was further investigated via the analysis of the ICE torque and the EM absorbed torque, when working as a generator. In Figure 58, the EM (top) and ICE (bottom) torques are reported as a function of torque requested at the wheels in Hybrid Mode conditions, colored according to the gear engaged. It can be seen that the higher the torque requested at the wheels, the higher the ICE contribution while the lower the EM contribution. Moreover, the linear relationship is found for each gear, except for the first one in which only the EV is enabled.

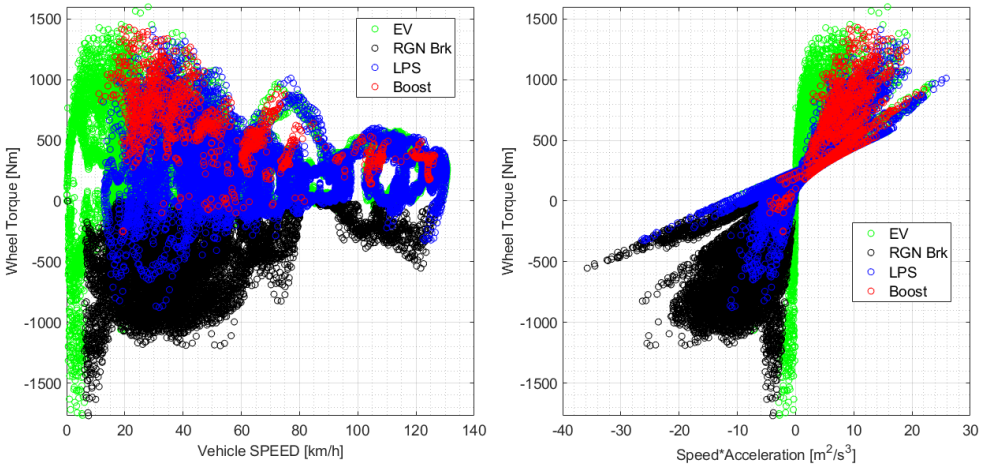


**Figure 57: Driving Mode split operating points as a function of vehicle speed (left) or speed times acceleration (right) and torque requested at the wheels**

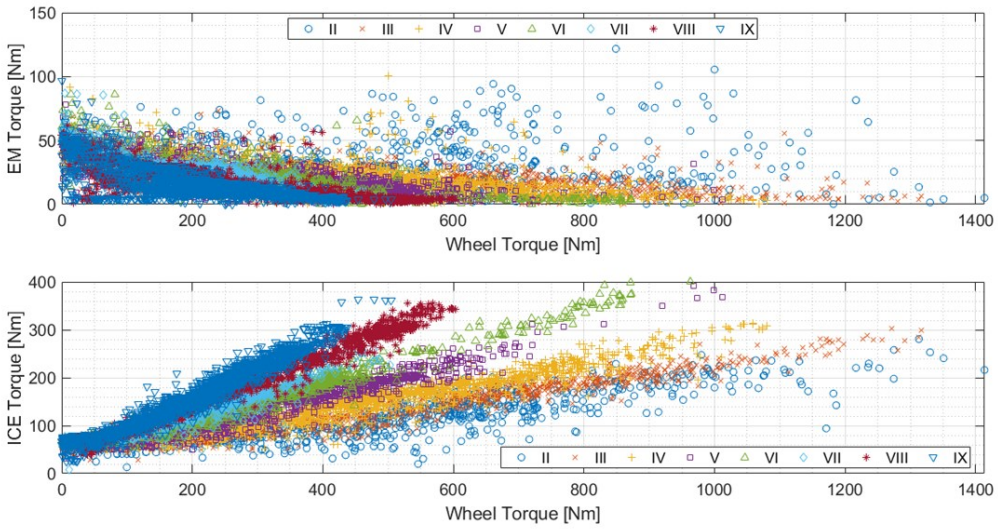


**Figure 58: EM absorbed toque (top) and ICE generated torque (bottom) versus torque requested at the wheels during Load Point Shift operations in Hybrid Mode**

To sum up, the complete experimental campaign has been rolled out and it clearly represents the core of the proposed methodology, since it gives the required tools and knowledge to deal with highly-complex powertrain and characterize the different components. On the development side, it is also a valuable starting point for the model calibration and validation. Hence, the next part of the work will introduce the model-based approach used for HEV investigation, based on data gathered from the experimental campaign. Some of the parameters adopted for HEV modelling have already been introduced and discussed, while the maps used for components characterization will be shown alongside with the model structure and physical equations.

# Chapter 3

# The Comprehensive xEV Model

Part of the work described in this Chapter was previously published in the following publications:

- DiPierro, G., Millo, F., Scassa, M., and Perazzo, A., "An Integrated Methodology for 0D Map-Based Powertrain Modelling Applied to a 48 V Mild-Hybrid Diesel Passenger Car," SAE Technical Paper 2018-01-1659, 2018, https://doi.org/10.4271/2018-01-1659.
- DiPierro, G., Millo, F., Tansini, A., Fontaras, G. et al., "An Integrated Experimental and Numerical Methodology for Plug-In Hybrid Electric Vehicle 0D Modelling," SAE Technical Paper 2019-24-0072, 2019.
- DiPierro, G., Millo, F., Galvagno, E., Velardocchia, M. et al., " A Reverse Engineering Method for Powertrain Parameters Characterization Applied to a P2 Plug-In Hybrid Electric Vehicle with Automatic Transmission," SAE Technical Paper 2020-37-0021, 2020.

The experimental campaign carried out on three different hybrid vehicles, described in Chapter 2, is the basis of the simulation process via the comprehensive map-based 0D HEV model. Inside this chapter, the main blocks and equation of the developed model will be explained; for the sake of brevity, only the newly developed sub-system will be shown in details, since they are the innovative part related to the simulation of the state of the art HEVs. Additionally, the characterization of the EM efficiency and the HV battery will be reported along with the respective model blocks. The model is capable of simulating the energy flow between the different powertrain components, as well as fuel consumption and $CO_2$ emissions; however, this aspect represents a further development of the proposed model, thus, it will be briefly introduced in the *Results* section. The core of the model is the physical representation of the powertrain devices by means of operating maps and the detection of the EMS throughout a limited number of data, available from the previously presented test campaign. The aim of the code is to accurately reproduce the powertrain behavior

along the NEDC and WLTC cycle, recognizing the torque split actuation of both a HEV and PHEV, other than correctly simulating the EM and ICE operating points, which are respectively used to compute the fuel and electric consumption. Other than the input form the experimental campaign and target data available in literature, the model requires input such as:

1. Mission speed and gear profile and, eventually, road gradient;
2. Ambient temperature and cooling circuit initial temperature;
3. HV battery starting SOC.

This chapter will present the design of the vehicle model, focusing on the main blocks introduced for the hybrid powertrain, as well as the map-based characterization of the electric components.

## 3.1 The Model-based Approach

Nowadays, model-based development in the automotive industry is widely adopted. Software like MATLAB/Simulink, MatrixX, Statemate or LabView are able to handle a conspicuous amount of data and high-frequency signals that are the most important data types in the automotive field. Consequently, the early stages of vehicle development have benefit from the usage of high-level models that can be used for different types of simulation [81]. As highlighted in Figure 59, in order to be competitive in the fast growing and adapting automotive market, the model-based approach reduces the so-called time to market and has a positive impact on costs by simplifying the validation process [82].

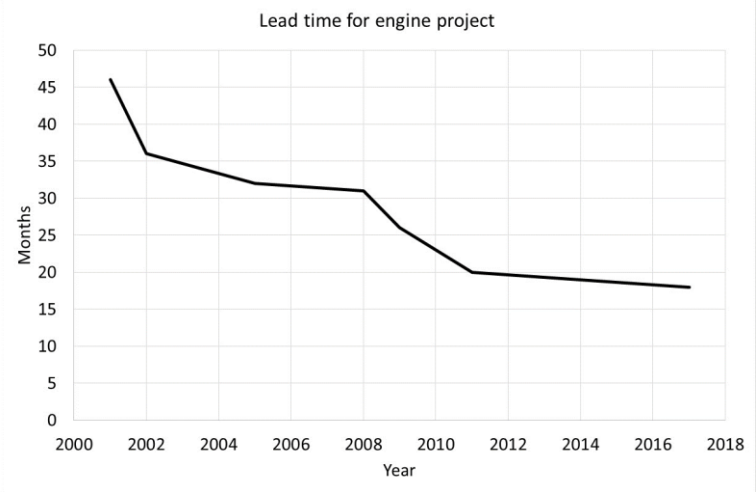


**Figure 59: Time to market evolution for engine project**[83]

As introduced in the previous chapters, the automotive word is now facing a more complex scenario, due to the introduction of alternative fueled vehicles. In this framework, the availability of a reliable simulation tool is a key enabler for the design and the optimization of complex systems such as HEVs. For the development of components or subsystems in the R&D field, detailed models are typically adopted (such as for instance 1D-CFD models for internal combustion engines or 3D-CFD models for fuel injection and combustion). On the other side,

to evaluate the further advantages given by a more complex system configuration, the focus is to simulate either the fuel economy or pollutant emissions or vehicle performance over long duration driving cycles. To this extent, the use of detailed models is not suitable for this task due to the high computational time required, hence, the look-up tables approach for fuel consumption and emissions is usually desired [84].

As far as this study is concerned, the investigation of fuel consumption and energy flows require a methodology that is a good compromise between simulation accuracy and computational time. Hence, a quasi-static approach was adopted with the aim of simulating multiple different driving conditions, such as various driving cycles for model calibration and validation. The quasi-static approach relies on a forward-facing model, involving a driver model (a PI controller) used to replicate the desired vehicle speed. Later, it creates a torque demand signal in order to cover the vehicle needs and the proper power split is determined according to the EMS logic; only the longitudinal vehicle dynamics equations are solved by the code [85–87]. Firstly, the primary shaft torque and speed are determined, later, power split, fuel consumption, CO2 emissions and pollutant emissions can be simulated by means of operating maps [88]. Overall, the simulation model can be considered as a quasi-static model, because the output of the main powertrain devices (ICE, EM, batteries) is extracted from steady-state performance maps. For the sake of clarity, the modelling approach shall be decided a-priori, depending on the targets of the simulation and on the boundary conditions. For example, fuel consumption of a conventional vehicle over the NEDC can be simulated with a reasonable accuracy in the quasi-static approach [89]: this is due to smooth variations of load and speed for the ICE on the NEDC. Similarly, NOx emissions can be simulated with an acceptable accuracy if data for the different combustion modes are available. However, this is not applicable to predict soot emissions, because of the strict dependency to transients phases and mixture formation; thus, a detailed soot model is required [90].

## 3.2 The comprehensive model

As already mentioned, model-based development enables system engineers to test the system in a virtual environment, before implementing the code on the final hardware. To this extent, after the experimental campaign on HEVs, this activity deals with the development of a comprehensive 0D quasi-static vehicle model in a Matlab/Simulink® environment; this software was chosen due to its high flexibility in the implementation of the energy management system strategies. The main goal was to build a model capable of reproducing different types of hybrid and full electric architectures, by the activation/deactivation of the required sub-model blocks, as explained in the following sections. In this regard, Figure 60 shows the possible parallel hybrid layouts that can be modelled.

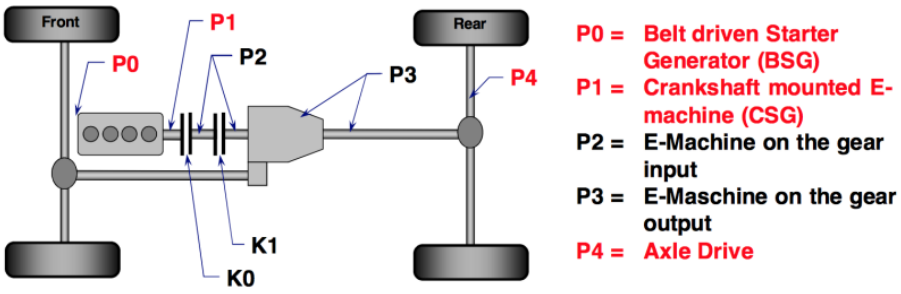


**Figure 60. Hybrid architecture nomenclature based on electric machine position for different parallel hybrid configurations** [91]

The proposed modelling method is common practice in the automotive field: the adoption of Matlab/Simulink® in combination with a 0D quasi-static approach has already been seen in different publications [92–95].The innovative feature is embedded into the model composition because of the distinction between the physical and the control environment. The front layer of the comprehensive model is reported in Figure 61: the CONTROLLER block is responsible for the control logic; the PHYSIC block reproduces the physics of the different vehicle components and subsystems. Furthermore, the SCOPE block manages the input/output transfer to the Matlab® workspace. The last block is the "Inputfile" block that collects the mission data coming from an external file, such as time, vehicle speed and gearshift profile for a specific driving cycle. This data are conveyed to the "inputBusIn" block, which gathers user input, such as specifications for vehicle, engine, driveline, electric machines, batteries, etc.

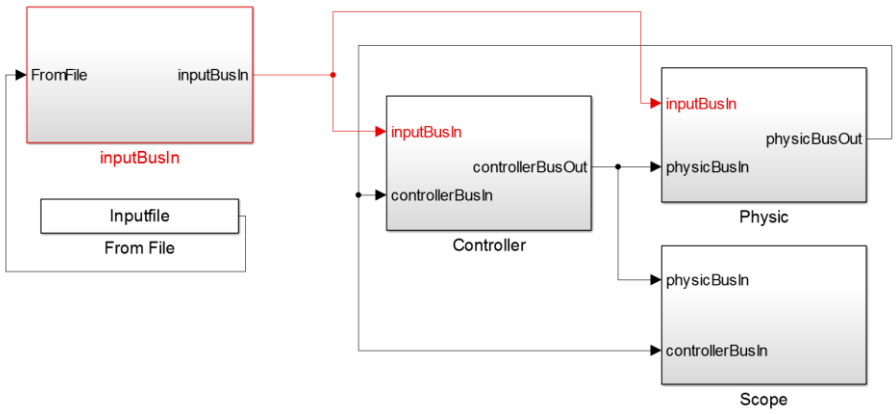


**Figure 61. Simulation model top layer**

With the introduction the modular model structure, the user can better manage different powertrain architectures. This means that all xCUs (generic Control Unit) and vehicle physical sub-systems have their own Simulink® sub-model, in order to facilitate model modularity. In fact, the control logic for the various components in the different architectures are embedded in the CONTROLLER block. On the other side, the physical behavior of the powertrain components is transformed into equations in the PHYSICS block. Hence, this layout was designed to simulate different HEV layout with one universal model, appropriate for vehicle investigation. After model calibration and validation, the user can

eventually perform a sensitivity analysis to assess powertrain components sizing or different EMS logics [76,78]. In the next paragraphs, the main model subsystems will be explained, along with creation of the most relevant input extracted from the experimental campaign, which have not been already discussed in Chapter 2. All the equations use simplified variable names with respect to the ones shown into the Simulink® pictures.

### 3.2.1 Vehicle model

The vehicle model is the physical representation of vehicle body and tires. The model also accounts for dynamic load transfer between the front and rear axle (pitch motion) of the vehicle; it consists of three separate sub-systems: *Air and rolling resistance*, *Brake torque limit front axle* and *Brake torque limit rear axle*. The main outputs are the actual vehicle speed, acceleration and travelled distance. The Simulink ® representation is shown in Figure 62:

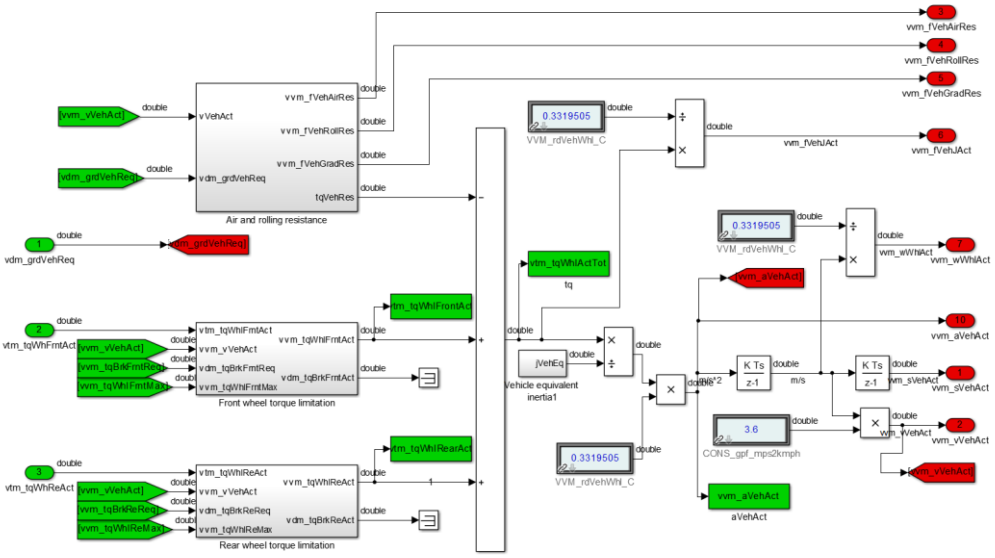


Figure 62: Vehicle model main layer

The sub-system *Air and rolling resistance* calculates the actual forces on the vehicle body because of air, rolling and gradient resistance. The total actual driving resistance is calculated according to equation (3-1). In particular, the air resistance can be calculated as a function of the physical vehicle properties and speed such as frontal area, drag coefficient and air density. Instead, the model used the derived quadratic coastdown coefficient. $F_2$, as shown in (3-2).The rolling resistance depends on rolling resistance factors, vehicle weight but in this case is calculated with the constant $F_0$ and linear $F_1$ coastdown coefficients, as reported in equation (3-3). Finally, the road inclination and vehicle weight are used to calculate the gradient resistance as in equation (3-4). RLs coefficients are reported in Table 5.

$$fVehTotRes = fVehAirRes + fVehRollRes + fVehGradRes \quad (3\text{-}1)$$

$$fVehAirRes = F_2 \cdot vVehAct^2 \tag{3-2}$$

$$fVehRollRes = (F_0 + F_1 \cdot vVehAct\ ) \cdot \cos(grdVehReq\ ) \tag{3-3}$$

$$fVehGradRes = mVeh \cdot g \cdot \sin(grdVehReq) \tag{3-4}$$

Where *fVehAirRes* is the air resistance, *fVehRollRes* is the rolling resistance and *fVehGradRes* is the resistance due to the gradient. *vVehAct* is the actual vehicle speed, *grdVehReq* is the road gradient, *mVeh* is the vehicle test mass and *g* is the gravitational acceleration.

Additionally, the *Front wheel torque limitation* as well as the *Rear wheel torque limitation* blocks limit the torque request to the maximum transferable torque; also, the brake torque request is limited, preventing negative vehicle speed after a brake event or when vehicle speed is close to zero. Once the actual resistance has been calculated and the actual torque to the wheels has been limited, signals such as acceleration, speed and distance are calculated as shown in equations from (3-5) to (3-7):

$$aVehAct = (tqWhlTotAct \cdot rdVehWhl) \,/\, jVehEq \tag{3-5}$$

$$vVehAct = \int aVehAct \cdot \mathrm{dt} \tag{3-6}$$

$$sVehAct = \int vVehAct \cdot \mathrm{dt} \tag{3-7}$$

Where *aVehAct* is the actual vehicle acceleration, *rdVehWhl* is the dynamic wheel radius and *jVehEq* is the vehicle equivalent inertia, which includes the rotating parts and it is assumed to be the 3% of the test mass [96]. By integrating the actual speed and acceleration, the actual travelled distance is then computed (*sVehAct*).

### 3.2.2 Driver model

The driver model is the physical representation of the driver, which controls the vehicle speed by a closed-loop control technique. It differs from the vehicle model since this model calculates the requested signals as first step of the simulation process, and not actual ones. Its main outputs are accelerator and brake torque request generated by a PI controller, as depicted by the red signals in Figure 63. These outputs then serve as an input for the powertrain and vehicle controls. This model contains the sub-systems *Drive Cycle* and *Driver*:

The sub-system *Drive cycle* contains a pre-scribed driving profile, which is an input of the simulation. In addition, the vehicle acceleration required to follow the cycle is calculated based on the given vehicle speed and the cycle gradient profile. This information is used in the *Driver* model for pre-control purposes, since it contains the physical driver behavior in terms of accelerator and brake torque request based on the *Drive-Cycle* sub-system output and the vehicle speed feedback.

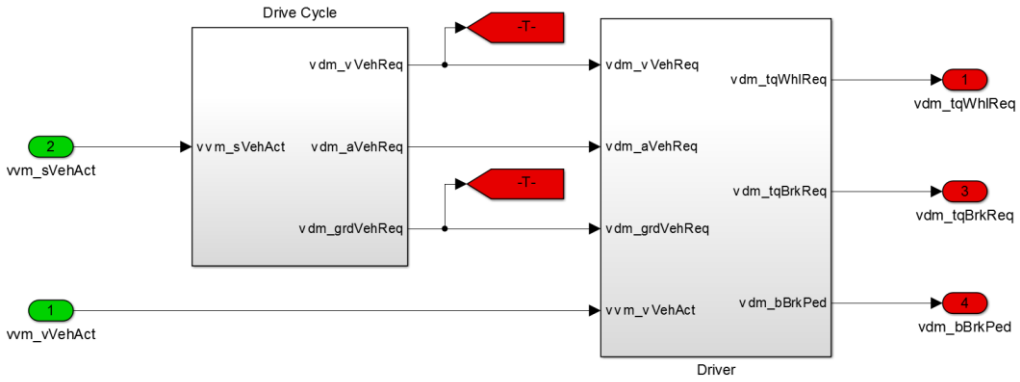


**Figure 63: Driver model main layer**

The sub-system *Driver* calculates the brake status and the brake torque request. It consists of a PI controller that is activated whenever the vehicle moves faster than the input speed profile. Brake torque request is calculated using equation (3-8):

$$tqBrkReq = (vVehReq - vVehAct) \cdot facPBrk + \int (vVehReq - vVehAct) \cdot facIBrk \cdot dt \quad (3\text{-}8)$$

Where *facPBrk* is the proportional multiplication factor for PI controller, *facIBrk* is the integral multiplication factor for PI controller, *vVehReq* is the vehicle speed target and *vVehAct* is the actual vehicle speed. Of course, the integral of the PI controller is reset whenever the actual vehicle speed drops below a specific threshold.

On the propulsion side, the torque requested at the wheels is calculated: the total driving resistance of vehicle is calculated based on vehicle weight, coastdown parameters and driving cycle inputs. In addition, the output of a PI controller is added, in order to account for any deviation between the pre-described speed profile and actual vehicle speed, calculated before in the vehicle model. Firstly, the four components of the total vehicle driving resistance are computed, as shown in equations (3-9) and (3-10):

$$tqWhlPrecReq = (F_{Acc} + F_{Air} + F_{Roll} + F_{Ramp}) \cdot rdVehWhl \quad (3\text{-}9)$$

$$F_{Acc} = mVehEq \cdot aVehReq \quad (3\text{-}10)$$

Where *tqWhlPreCtrlReq* is the total vehicle driving resistance before the controller intervention, *rdVehWhl* is the dynamic wheel radius and $F_{acc}$ is the vehicle inertia force due to its equivalent mass (1.03 times the test mass). The air $F_{Air}$, rolling $F_{Roll}$ and road slope $F_{Ramp}$ contribution are calculated as previously shown in equations (3-3), (3-4) and (3-5), but taking into account the requested vehicle speed. Later, a PI controller adjusts the torque request using the speed difference between the requested and actual vehicle speed. The controller torque request is calculated using the equation (3-11):

$$tqWhlCtReq = (vVehReq - vVehAct) \cdot facPAcc + \int (vVehReq - vVehAct) \cdot facIAcc \cdot dt) \quad (3\text{-}11)$$

Where f*acPAcc* is the proportional multiplication factor and f*acIAcc* is the integral multiplication factor for PI controller. The integral factor was calibrated both for over and under estimation of the vehicle target speed.

### 3.2.3 Engine model

The engine model is the physical representation of the engine to account for inertia, fuel consumption/emissions and temperature effects; moreover, it accounts for the control logic provided by the ECM. As for the proposed research activity, the engine model does not constitute an innovative block, since it has been previously created and used over the years for conventional vehicle simulation. Hence, the ICE model will not be discussed in details, but the main input and output will be introduced.

The engine model is composed by the *Physical engine* block, the *Engine thermal model* and the *Fuel consumption/emission* calculation. More in details, the physical engine model describes the mechanical engine to account for inertia effects and engine start; the thermal model describes the engine thermal behavior and the related heat-up of the coolant liquid, engine block and oil. Finally, being a map-based model, the fuel consumption and emission calculation is performed via look-up tables. Figure 64 illustrates the top layer of the engine model: as one can notice, based on the input coming from the same engine controller (i.e. from the HCU controller later reported), the physical ICE model calculates the actual quantities, such as: actual engine speed, actual Brake Mean Effective Pressure (BMEP), actual torque, a warm-up indicator, and actual temperature for engine oil temperature, engine coolant and engine block.

As far as fuel consumption and emissions are concerned, the model calculates all these quantities as a function of the engine operating points (engine speed and mean indicated pressure. It is worth to mention that, due to the specific requirements of each project, it was not always possible to perform $CO_2$ and/or emission measurement over the different test; in the proper way to build-up operating maps. Hence, fuel consumption and $CO_2$ emission maps fitted into the model are normally taken from same but different engines, whose data were available internally. Later, data were calibrated according to the available experimental data gathered during the testing campaign. In the *Results and Discussion* section, this topic will be carefully explained before showing the related results.


Figure 64: Engine physical model top layer

### 3.2.4 Transmission Model

The transmission model is the physical representation of the transmission to account for the different gear ratios, clutch positions, efficiency and temperature effects; moreover, it controls the operation of the clutches and reduces the appropriate amount of motor torque in the event of a gear shift. As previously stated for the engine model, the transmission model does not constitute an innovative block, since it has already been part of the simulation platform. Hence, it will not be discussed in details, but the main input and output will be introduced.

Figure 65 depicts the content of the sub-system *Physical Transmission*, which is a physical representation of the mechanical transmission and clutches to account for transmission losses due to mechanical losses and clutch engagement/disengagement. On the thermal side, the *Thermal model* models the transmission thermal behavior and heat-up of the transmission housing and oil. The output of the thermal model is then used as input for the physical model to compute the mechanical losses, which are function of input operating conditions (powertrain speed and load) and oil temperature. Also in this case, it is worth to mention that it was not always possible to perform transmission efficiency measurement; since this normally requires gearbox teardown and complex and costly instrumentation. Hence, the mechanical efficiency maps fitted into the model are normally taken from same but different architectures, whose data were available internally. Afterwards, data were calibrated according to the available experimental data gathered during the testing campaign.

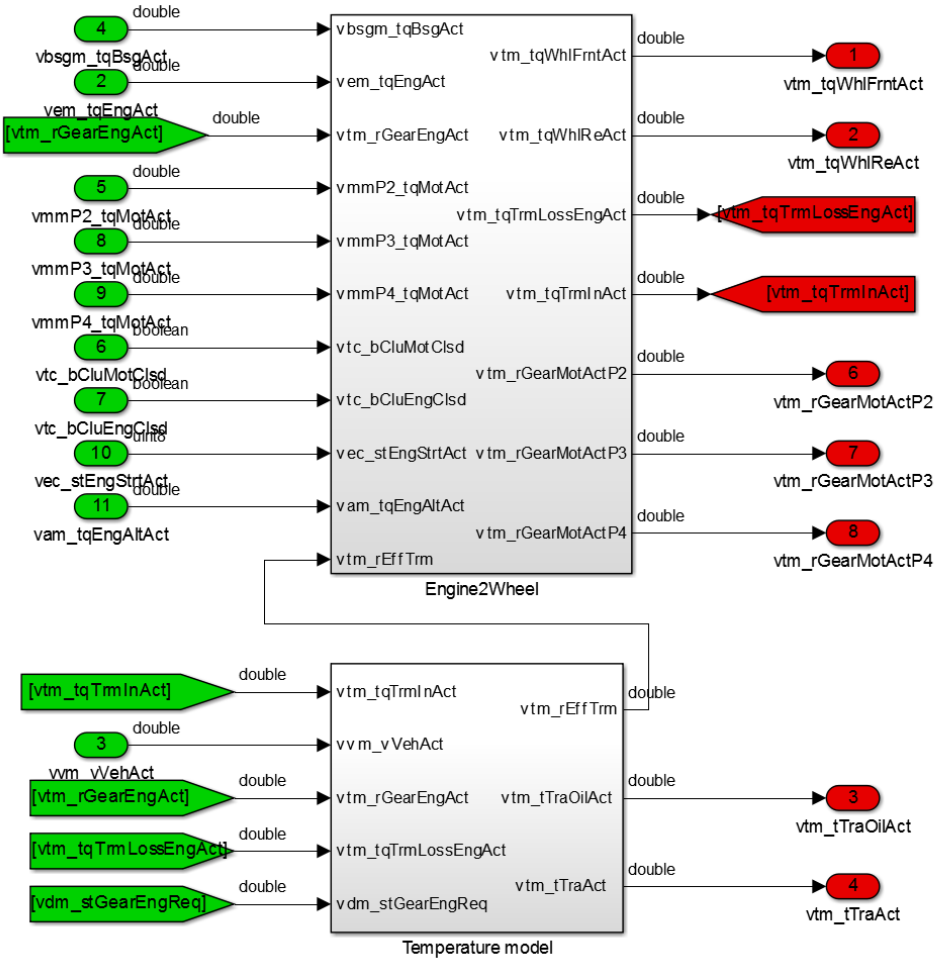


Figure 65: Physical transmission model

### 3.2.5 E-motor model

The motor physical model is the physical representation of the electric traction motor. The model accounts for the calculation of motor speed, torque and actual electric power consumption. The motor model is identically reproduced for every electric machine present on-board, regardless of the position; hence, the model applies also for the BSG/HSG. Since this model was already built into the simulation platform, only the main input and calculations will be explained.

As illustrated in Figure 66, the motor physical model second layer contains the calculation for the dynamic motor speed during vehicle launch and engine start, while the *Zero current control* block determines if the motor is in zero current control mode and adapts the power consumption and the motor drag torque accordingly.

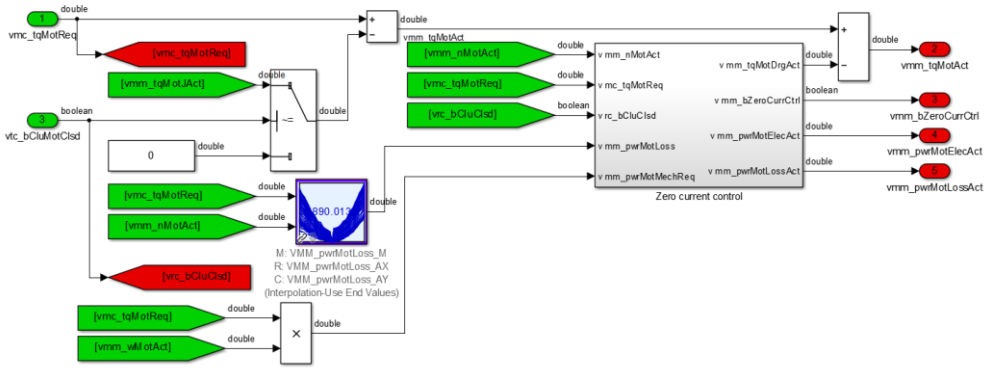


**Figure 66: Motor physical model**

The core of the motor physical model is made by the efficiency maps, which are used to take into account the motor losses both in motor and generator mode. The creation of the motor efficiency map is a key output of the experimental campaign, though the vehicle was not tear down and the EM was never tested on a test bench. It was possible to assess the motor/generator efficiency based on the acquired signals, such as current, voltage and CAN measurements.

Considering the different vehicle layout and instrumentation plan reported in Figure 17 to Figure 19, only for Vehicle 1 was possible to directly measure the electric DC power flowing to the BSG, since it has an integrated AC/DC converter, thus, the motor efficiency includes also the converter efficiency, which was not modelled separately. On the other side, Vehicle 2 and Vehicle 3 have a sophisticated power electronics; hence, no direct measurements were performed on the HV AC 3-phase side. For this reason, the electric power associated with the P2 motors was calculated as a difference between the HV battery side and the LV side, at the DCDC output. E-motor power is then computed as in equation (3-12):

$$P_{el} = (V \cdot I)_{BatHV} - (V \cdot I)_{DCDC\_LV} \tag{3-12}$$

Where $V$ and $I$ are respectively current and voltage measured on the HV and LV side. It is important to mention that, as far as Vehicle 2 is concerned, the HV power is also used to feed the belt-driven HSG (see Figure 18). Hence the previous equation is only valid when the HSG is not working. To prevent errors in energy flow calculation, an additional current clamp was placed on one of the three phases of the HSG power supply, in order to understand whenever the starter/generator was used. As demonstrated during the experimental campaign, the HSG has a smaller impact on the vehicle EMS and it is mainly used. Thus, it was decide to neglect its energy contribution focus on the traction EM.

As far as the motor efficiency is concerned, Figure 66 shows that it depends on motor speed and load, and it is used to calculate the electric energy requested to the HV battery, based on the mechanical and electrical power balance, as follows:

$$P_m = 2\pi \cdot tqMotAct \cdot \frac{nMotAct}{60} \tag{3-13}$$

$$P_{el} = P_m \cdot \eta_c^k \cdot \eta_m^k \tag{3-14}$$

Where $P_m$ is the mechanical power, *tqMotAct* is the actual e-motor torque and *nMotAct* is the actual speed. On the electric side, $P_{el}$ is the electric power request, $\eta_c$ is the inverter efficiency, $\eta_m$ is the mechanical efficiency and $k$ is a constant (equal to -1 during discharge, and equal to 1 during charge). Once the hybrid controller decide the EM working points, the electric power output is sent to the HV battery.

The working points recorded during the experimental campaign have been used for the efficiency maps calculation, as already illustrated in Figure 35, Figure 44 and Figure 55. Assuming a constant 98% inverter efficiency, the EM efficiency was calculated from equation (3-14) as a ratio between mechanical and electrical power; later, to account for the fact that it was not possible to cover the complete working map, an in-house built Matlab tool was used, capable of scaling both EM and BSG efficiency maps, starting from information available in an internal database related to similar PMSM [97–100]. As a result, Figure 67 shows the output of the efficiency mapping process for all the EMs involved in this research activity. Pictures on the top are related to the BSG from Vehicle 1 (left) and the HSG from Vehicle 2 (right); on the bottom the efficiency maps of the P2 EMs from Vehicle 2 (left) and Vehicle 3 (right) are depicted. As usual, the efficiency is plotted over the load-speed map: maximum EM efficiency is about 95%, as shown in the green area, and it is reached in the low-speed medium-torque area. As a consequence, the HCU controls the Ems to mainly operate in the central plot area, in order to reduce the mechanical losses. The curves on top of the map are the target maximum peak motor torque, while the bottom dashed curves are the maximum continuous motor torque. On the negative side, same curves represent the maximum torque values for the EM generator mode. Same for the BSG, where maximum efficiency is around 95%; the starter-generator has a maximum higher speed, since it has to take into account the belt ratio for mechanical coupling.

To conclude, the e-motor model calculates the rotational speed starting from the actual vehicle speed, as shown in Figure 68. The rotational speed is computed from the wheels to the motor, as in the following equation:

$$nMotAct = \frac{Vel_{veh}}{R_{dyn}} \cdot \tau_{gb} \cdot \tau_{fd} \tag{3-15}$$

Where $Vel_{veh}$ is the vehicle speed, $R_{dyn}$ is the dynamic wheel radius, $\tau_{gb}$ is the gear ratio and $\tau_{fd}$ is the final drive ratio. This procedure is not applicable during a gearshift event because the cinematic connection is not verified, due to disengagement of the gears.

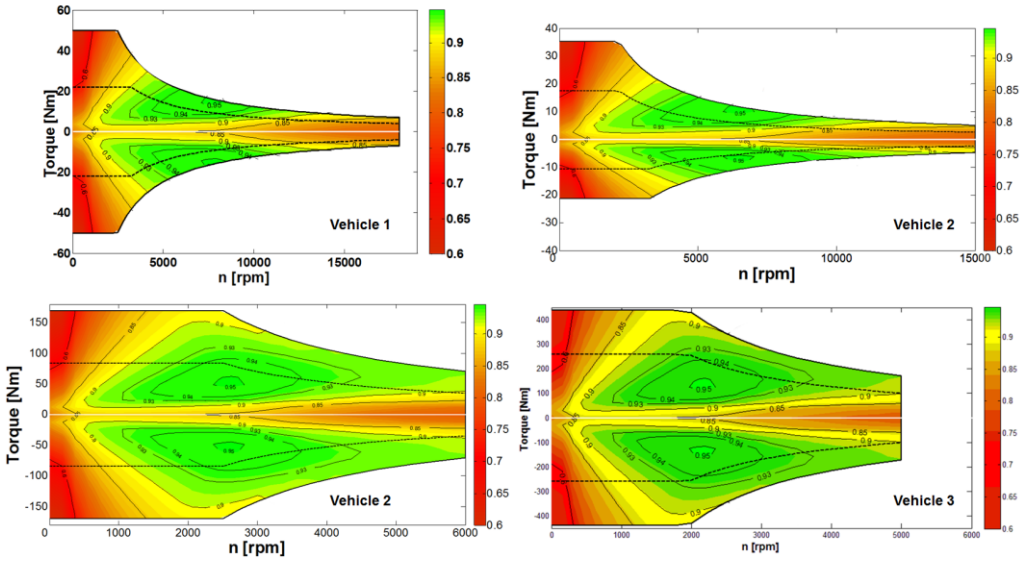


Figure 67: Efficiency maps for BSG (top-left), HSG (top-right) and Ems (bottom) of the three test cases

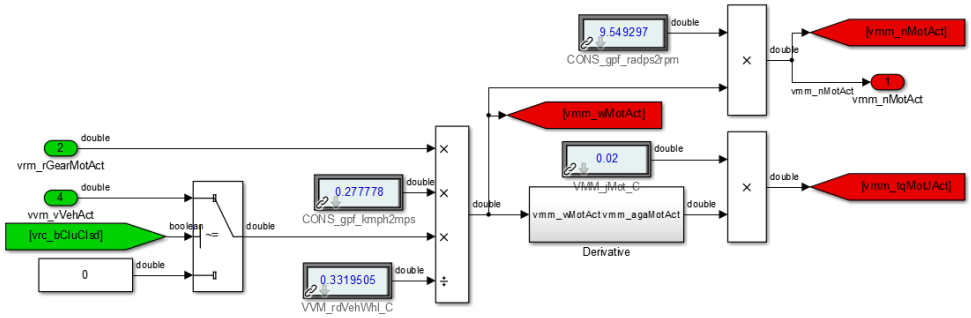


Figure 68: E-motor speed calculation

Finally, it has to be mentioned that the EM physical motor receives input from the motor controller module, which is responsible for limiting the torque request from the hybrid control unit (later illustrated). The electric traction motor maximum available torque is equal to the full-load curve already reported, both in motor and generator mode. In addition, a time limit is included to prevent the EM to work in peak operation for a long time, which in reality can cause thermal issues and consequent power limitation.

### 3.2.6 HV Battery model

The battery physical model is the physical representation of the HV battery and it is made of different sub-systems. The model accounts for the calculation of battery SOC, voltage and current as a function of power request.

The sub-system *Open circuit voltage and internal resistance* is illustrated in Figure 69; it contains cell based profiles battery characteristics, which serve as an input for the battery model. In addition, it contains scaling parameters such as the number of cells in series and in parallel. Both the open circuit voltage (OCV) as

well as the internal resistance are functions of battery State of Charge (SOC) and battery cell temperature. The output of the two look-up tables is then scaled according to the battery configuration.

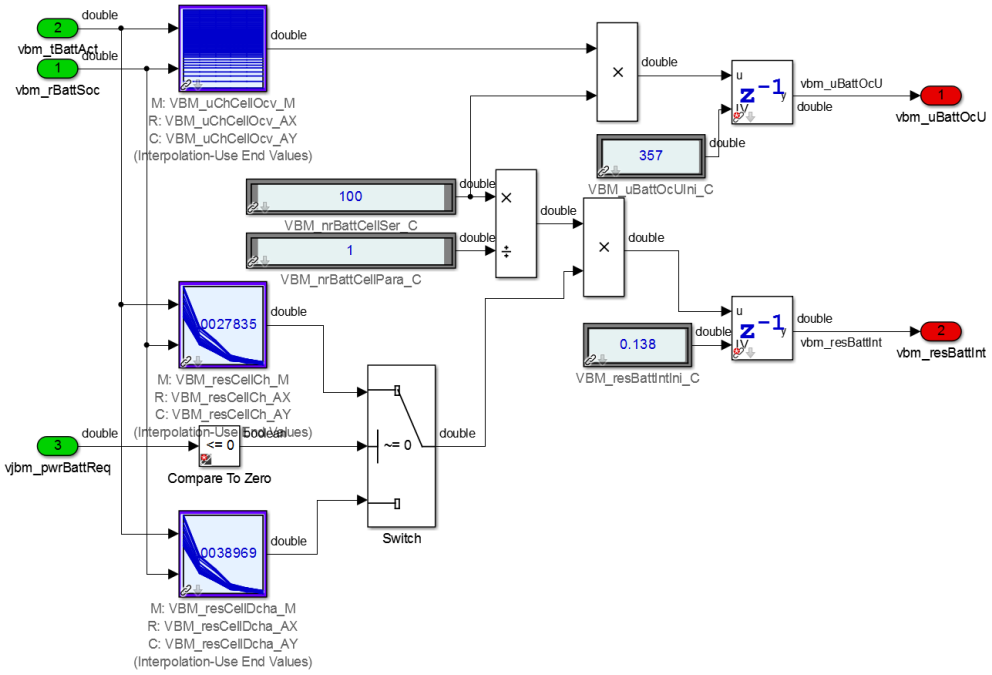


Figure 69: Open circuit voltage and internal resistance sub-system

Equation (3-16) shows the OCV calculation:

$$uBattOcU = f(rBattSoc, tBattAct) \cdot nrBattCellSer \qquad (3\text{-}16)$$

Where *nrBattCellSer* is the number of HV battery cells in series, *rBattSoc* is the battery SOC and *tBattAct* is the actual HV battery cell temperature. On the other side, the total battery internal resistance is calculated according to equation (3-17):

$$resBattInt = f(rBattSoC, tBattAct) \cdot \frac{nrBattCellSer}{nrBattCellPar} \qquad (3\text{-}17)$$

Where *nrBattCellPar* is the number of HV battery cells in parallel and *resBattInt* is the total HV battery internal resistance. It can be noticed that the battery cell internal resistance has two different maps, one for charging events and another for discharge events.

In this regard, the data recorded during the experimental campaign have been used for the assessment of both the battery internal resistance and the cell OCV. As a matter of fact, the data collected cover a wide range of battery current, voltage and SOC, other than the operating points of the rest of the powertrain. Therefore, the HV battery was characterized adopting a very simple equivalent model, made of an ideal OCV generator and a resistance in series, which represents the internal resistance of the battery, as illustrated in Figure 70.

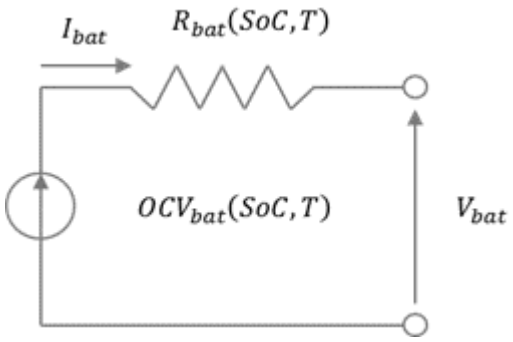


Figure 70: Battery equivalent model

For each type of battery technology, both the OCV and the internal resistance can be mapped as a function of the SOC and the cell temperature; more in details, the OCV is strictly related to the chemistry, hence data available in the scientific literature were used to create the OCV curve. According to [101], the relationship between SOC and OCV battery cell can be modelled and validated through a set of experiments. Thus, the OCV dependency on cell SOC can be represented with the following equation:

$$OCV(SoC) = a + b \cdot [-\ln(SoC)]^m + c \cdot SoC + d \cdot e^{n \cdot (SoC-1)} \qquad (3\text{-}18)$$

Where *a*, *b*, *c*, *d*, *m*, *n* are the calibration coefficients of the model. As for the Vehicle 1 LTO battery, this parameters were found in [101]; while the Vehicle 2 Lithium-ion Polymer battery cell was characterized with data from [102] and Vehicle 3 Lithium- NMC battery uses data from [103,104]. Hence, data available in the scientific community are used as a starting point for this analysis. Later, to account for multiple factors, such as the cell chemistry, the electrode material composition, the electrolyte ionic conductivity, and the fact that the model involves the complete battery pack rather than the single cell, the model parameters were experimentally characterized by achieving the same battery voltage output, which was measured during the aforementioned tests.

As already explained in the instrumentation section, both battery current and voltage are measured during tests; so that the voltage across the battery load and the OCV are linked by the following equation:

$$\Delta V\ [V] = (OCV[V] - I[A] \cdot \mathrm{R}_{Int}[\Omega]) \cdot nr_{cells} \qquad (3\text{-}19)$$

Where $\Delta V$ and $I$ are measured, while the $OCV$ and $R_{Int}$ are initially taken from literature and $nr_{cells}$ is the number of cells in series configuration. As a result, the measured output voltage (black line) and the first-tentative modelled voltage (blue line) can be compared, either during charging and discharging driving, as illustrated on the left side of Figure 71. After this step, the same equation can be rewritten with the adoption of some coefficient that will be later calibrated, as follows:

$$\Delta V_{sim}\,[V] = (\alpha \cdot OCV[V] - I[A] \cdot \beta \cdot \mathrm{R}_{Int}[\Omega]) \cdot nr_{cells} \qquad (3\text{-}20)$$

Where $\Delta V_{sim}$ is the model voltage, while α and β are the two parameters used to calibrate the new resistance and OCV maps, either for the charging and discharging test. To this extent, a root mean square error (RMSE) minimization problem has been solved to match the gap between the model and experimental output; resulting in both OCV and internal resistance map variations. The minimization problem returns a corrected voltage output signal with an adjusted $r^2$ of around 0.995, as highlighted on the right side of Figure 71.

Finally, the three maps shown in Figure 72 respectively represents the α-corrected OCV cell values for the LTO (left), the LiPo (center) and the Li-NMC (right) battery technology. As it can be noticed, the temperature effects was considered negligible due to the fact that the battery simulation is mainly performed under normal operating conditions. Similarly, the three maps in Figure 73 illustrates the β-corrected cell internal resistance values. It is worth to mention that only for Vehicle 1, as a first test case, a constant resistance value of about 14 mΩ [105] was assumed. Later, more data were found in literature as for the LiPo and the Li-NMC technology, hence, the corrected resistance values were calculated both in charging and discharging phases. As illustrated on the left side of Figure 73, for the Vehicle 2 LiPo battery, the same map can be adopted to model the cell internal resistance. As one can notice from the curves, the reported values are calculated at cell level to reflect the average data available in literature.

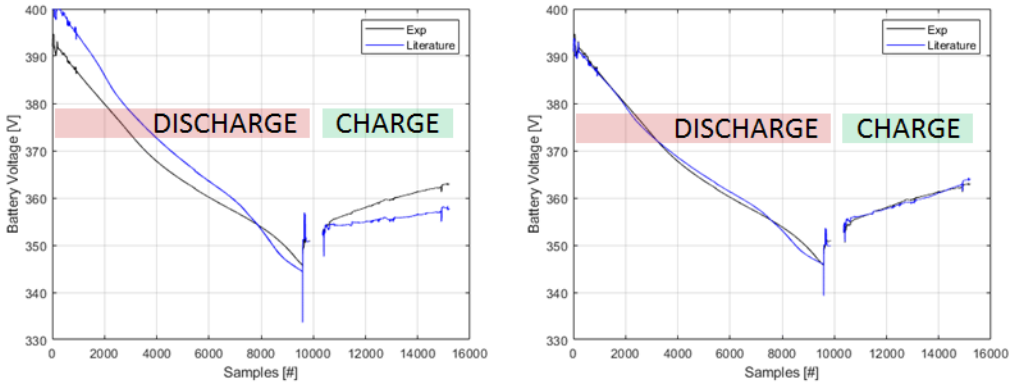


Figure 71: Battery model output voltage correlation before (left) and after (right) maps correction

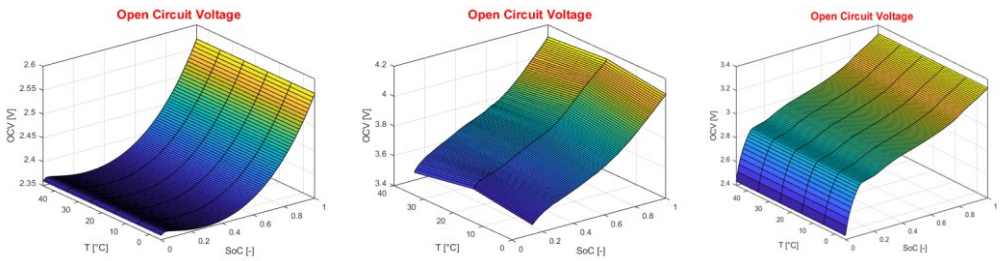


Figure 72: HV battery cell OCV for LTO (left), LiPo (center) and Li-NMC (right) technology

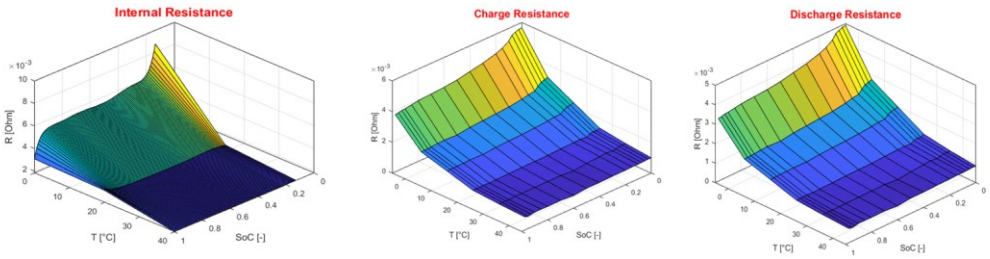


**Figure 73: HV battery cell internal resistance for LiPo (left) and Li-NMC in charge (center) and discharge (right)**

To conclude, the experimental characterization is based on the implementation of the OCV-R model for the batteries under investigation; the corrected maps were implemented into the previously mentioned battery physical model.

Once the battery SOC and internal resistance were computed, the battery voltage and actual current were determined as a function of the battery power request, which comes from the onboard electric loads request. This calculation is based on the battery equivalent circuit previously shown in Figure 70. The battery actual current is calculated according to equation (3-21):

$$iBattAct = \frac{uBattOcU - \sqrt{uBattOcU^2 - 4 \cdot pwrBattReq \cdot resBattInt}}{2 \cdot resBattInt} \qquad (3\text{-}21)$$

Where *pwrBattReq* is the HV battery power request and *iBattAct* is the actual battery current. Afterwards, the battery actual voltage *uBattAct* and the actual power losses *pwrBattLossAct* are determined using equation (3-22) and (3-23):

$$uBattAct = uBattOcU - iBattAct \cdot resBattInt \qquad (3\text{-}22)$$

$$pwrBattLossAct = iBattAct^2 \cdot resBattInt \qquad (3\text{-}23)$$

Finally, the HV battery SOC is calculated based on the actual battery current, as shown in Figure 74.

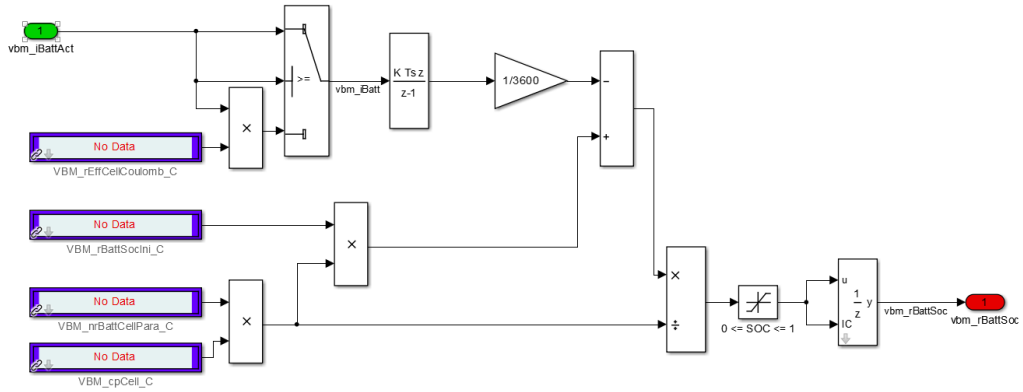


**Figure 74: HV battery SOC calculation**

For positive (discharge) current, SOC is calculated following equation:

$$rBattSoc = \frac{(nrBattCellPar \cdot cpCell \cdot rBattSoCIni) - \frac{\int iBattAct \cdot dt}{3600}}{nrBattCellPar \cdot cpCell} \quad (3\text{-}24)$$

Where *cpCell* is the HV battery cell nominal capacity and *rBattSoCIni* is the HV battery initial SOC. While for negative (charge) current, the actual battery current is multiplied by the battery coulombic efficiency, which has been calibrated during the simulation of the different vehicles.

It is important to mention that these maps were also adopted for the calculation of the peak power during the charging and the discharging phase of the complete battery pack. To this extent, the HV battery controller block verifies that the power limits are fulfilled; hence, the battery power request is always compared to the nominal one, during peak and continuous operation. By acquiring current peaks during motoring and regeneration, the maximum power available was calculated according to the following equations:

$$P_{max,p,dch} = \left(OCV[V] - I_{max,p,dch}[A] \cdot \mathrm{R}_{Int,dch}[\Omega]\right) \cdot I_{max,p,dch} \quad (3\text{-}25)$$

$$P_{max,p,ch} = \left(OCV[V] - I_{max,p,ch}[A] \cdot \mathrm{R}_{Int,dch}[\Omega]\right) \cdot I_{max,p,ch} \quad (3\text{-}26)$$

$$P_{max,c,dch} = \left(OCV[V] - I_{max,c,dch}[A] \cdot \mathrm{R}_{Int,dch}[\Omega]\right) \cdot I_{max,c,dch} \quad (3\text{-}27)$$

$$P_{max,c,ch} = \left(OCV[V] - I_{max,c,ch}[A] \cdot \mathrm{R}_{Int}[\Omega]\right) \cdot I_{max,c,ch} \quad (3\text{-}28)$$

Where *Pmax,p,dch* is the maximum discharge peak power, *Pmax,p,ch* is the maximum charge peak power *Pmax,c,dch* is the maximum discharge continuous power, *Pmax,c,ch* is the maximum charge continuous power, OCV is the open circuit voltage, *Rint,dch* is the discharge internal resistance, *Rint,ch* is the charge internal resistance, *Imax,p,dch* is the maximum discharge peak current, *Imax,p,ch* is the maximum charge peak current, *Imax,c,dch* is the maximum discharge continuous current and *Imax,c,ch* is the maximum charge continuous current.

An example of the reported calculation is illustrated in Figure 75, where the maximum power under the pre-defined conditions are reported for the HV battery pack of Vehicle 3. It is worth to mention that the peak situation involves a higher power request, but for a shorter time due to thermal limitations. For the sake of simplicity, the absolute values of the discharge power are reported in the following picture, however, it is intended to be a negative power and it happens when a negative current flows out of the battery.

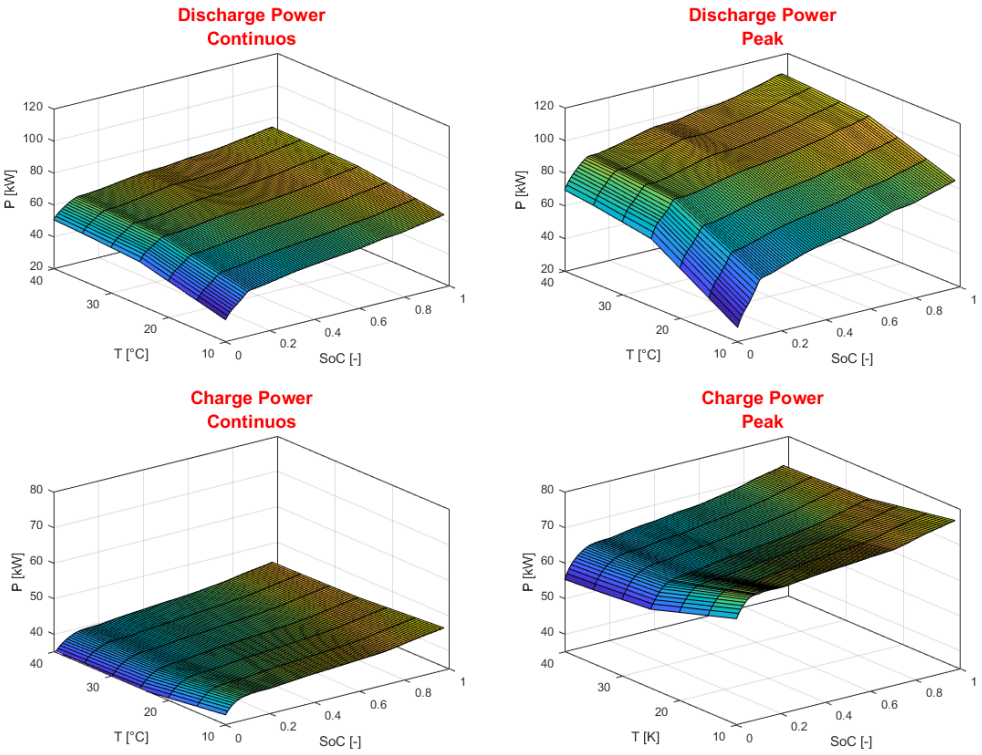


**Figure 75: HV battery power limit maps during discharge (top) and charge (bottom), both in Continuous (left) and Peak (right) operations**

### 3.2.7 Hybrid Control Unit model

The simulation platform is considered a comprehensive Hybrid Electric Vehicle model since it offers the capability to simulate various parallel hybrid configuration, as classified in Figure 60. The model allows the user to select the desired layout by defining some constant variables as simulation input. Figure 76 shows the different input variables that act as triggers for the layout definition, with an enlargement on the P0-P2 and P0 blocks. Once this has been decided, the respective HCU block is activated. In particular, the model is capable of simulating: P0, P0-P2, P2-P4 and P0-P4 configurations, while the pure P2 and P4 configurations can be simulated by disabling the belt starter/generator (i.e. the P0 contribution). In the following lines, the generic composition of the HCU model will be explained, since the behavior of the different powertrains presented in this activity is then summarized by the operating maps introduced in the previous chapter.

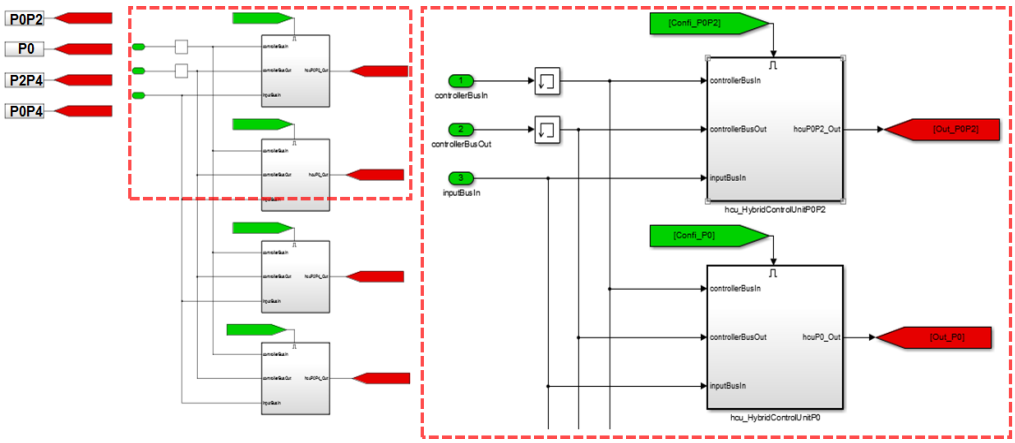


Figure 76: HCU model - layout switch

The Hybrid Control Unit (HCU) has to control the complete powertrain, acting as a master controller for all slave controllers such as the ICE, the EM and/or BSG controllers. The HCU is responsible for the driving mode request: whether it is E-Drive, ICE start/stop and so HEV mode. Besides that, it accounts for the battery charging/discharging strategy, not only controlling the driving mode selection as well as the torque split definition between the different powertrains components. A schematic representation of the hybrid control unit is shown in Figure 77: the driving mode decision is made in *Driving Mode Selection* block, which uses input signals such as wheel torque request, vehicle speed and HV battery SOC in order to select the most appropriate driving mode: E-Drive or Hybrid. Later, this request is forwarded to the *Torque Manager State*. This is responsible for the activation of the different mode dedicated functionalities, such as the EV or parallel HEV mode, the Engine start and Engine stop and the correct execution of the engine start and stop procedure. The sub-systems *E-Drive or parallel*, *Engine start* and *Engine stop* contain functionalities that control the torque for each driving mode separately and are activated by the *Torque Manager State* only; this means that only one state can be active at the same time.

The outputs of these three sub-systems are then merged in *Torque Manager Output*, which has the role to forward the torque request of the appropriate mode to the slave controllers, e.g. engine, motor and battery controller.

The *Driving mode selection* system controls the *'hcu_bHybReq'* and *'hcu_bEDrvReq'* outputs, for the request of the hybrid or E-Drive mode activation respectively, as shown in Figure 78. The driving mode rules will be later explained, in order to discern between the basic P0 and the more complex P2 logics.

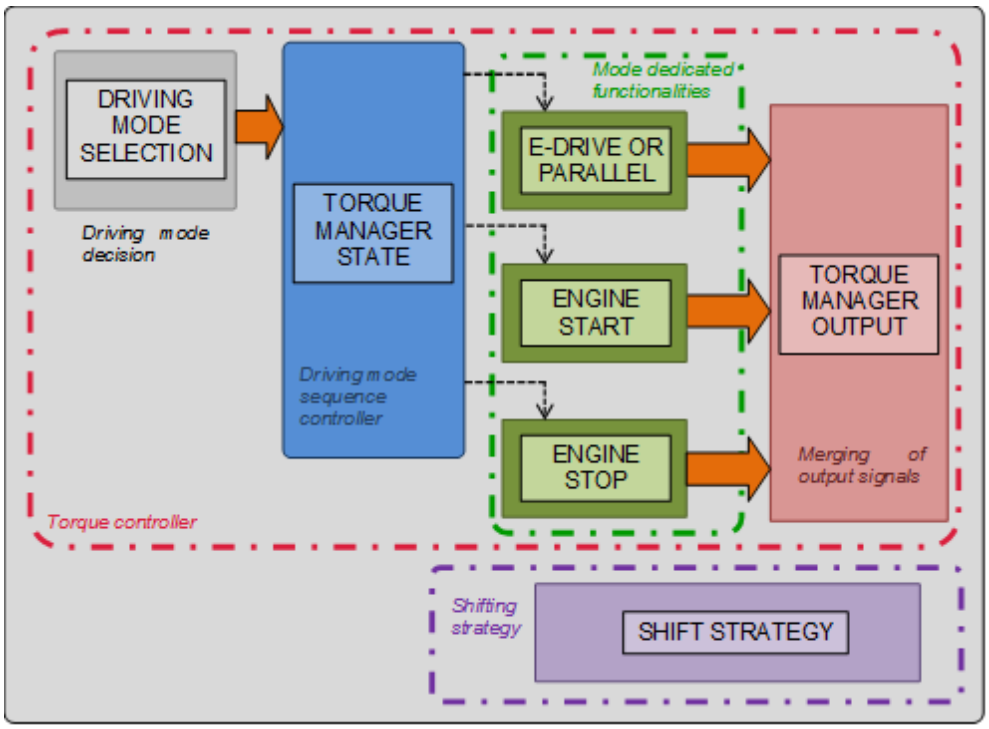


Figure 77: Hybrid control unit schematic representation

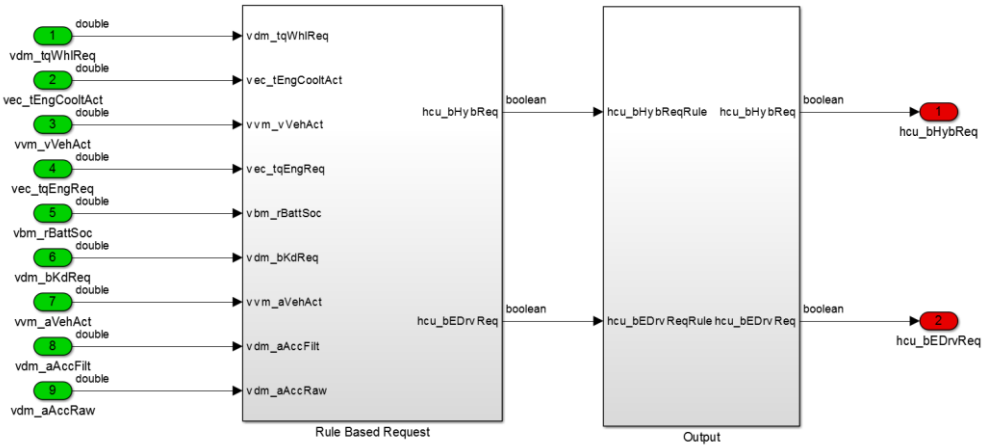


Figure 78: Driving Mode Selection block

Afterwards, the driving mode request goes into the *Torque Manager State* that is designed with the StateFlow® of Figure 79 and Figure 80. The state machine is divided in two de-compositions: *Hybrid mode selection* and *Hybrid mode extended*. Based on the input from the driving mode selection, the first de-composition *'Hybrid mode selection'* actives the appropriate sub-system for the correct torque split as well as the sequence which shall be applied during an engine start event. Possible modes are:

- E-Drive
- Engine start conventional/BSG
- Hybrid
- Engine stop

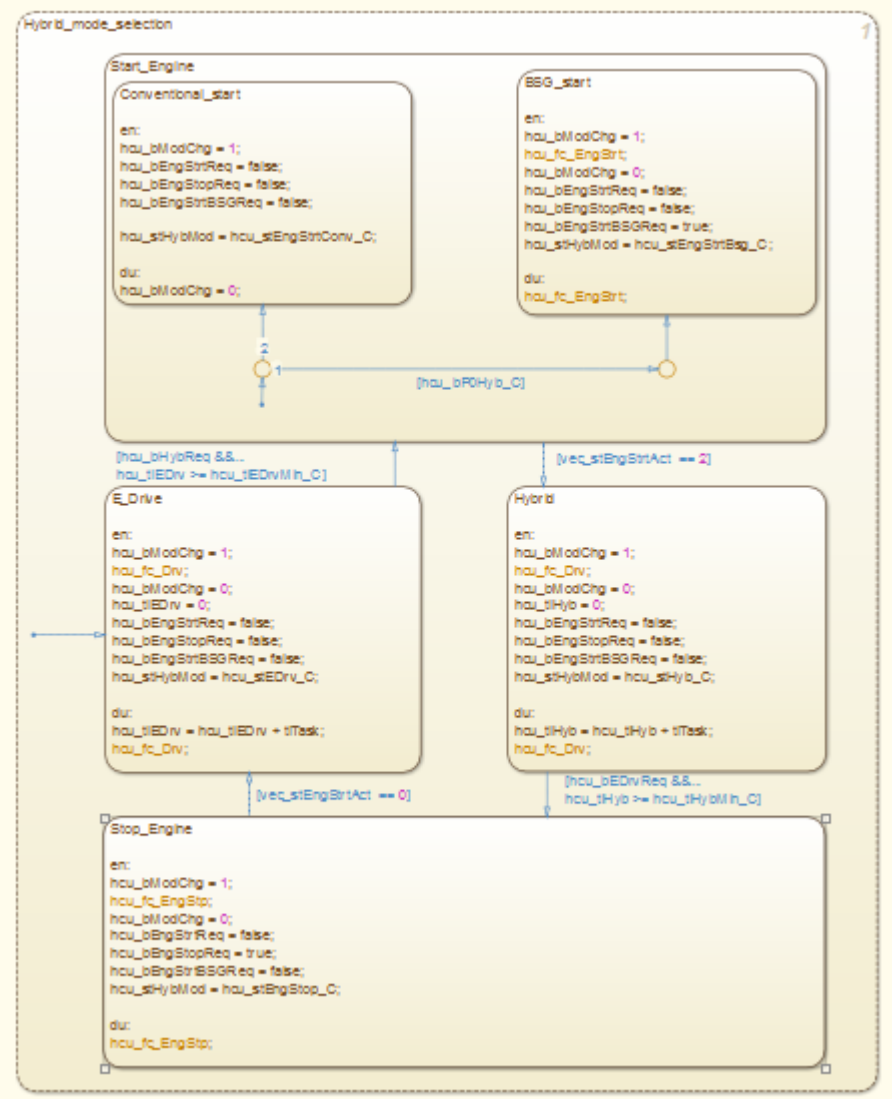


**Figure 79: Torque Manager State – Hybrid mode decompositions**

At the same time, decisions are made into the *Hybrid Mode Extended* decomposition, based on the input from the *Hybrid Mode Selection*. Other than the simple Electric Driving, this decomposition creates a status variable according to the specific driving mode and other boundary conditions, such as:

- E-Drive Propulsion
- Hybrid > Engine Only
- Hybrid > Load Point Shift
- Recuperation

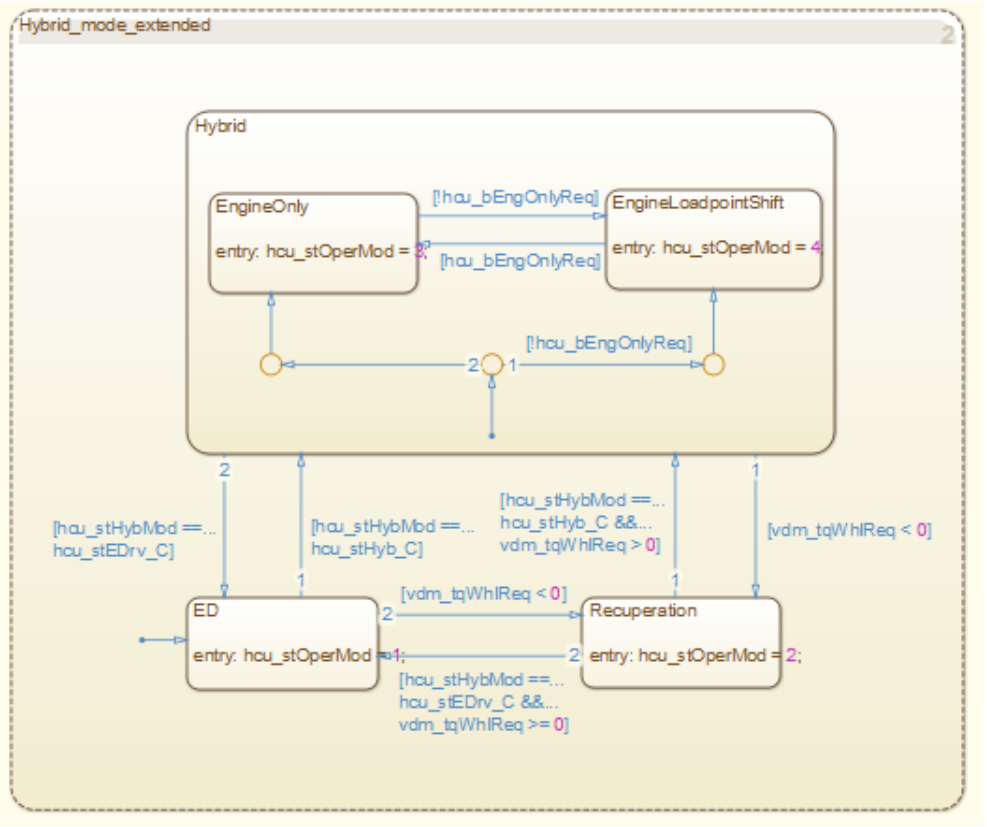


**Figure 80: Torque Manager State – Extended Hybrid Mode decomposition**

After a specific mode has been enabled, the desired functionalities are activated in the *E-Drive or parallel* block, where, other than pure electric driving, the torque split between the EM and ICE is actuated, based on the condition previously entered and characterized during the experimental campaign. As for the hybrid strategy, the block allows the engine to work in load point shift, resulting in charging or discharging the battery. The sub-system is shown in Figure 81 and it is a state machine that simultaneously defines the torque request for the different machines, such as the ICE, EM and BSG. As can be seen from the picture, the different hybrid driving conditions are taken into account, such as battery charging and boosting using either the EM or the BSG. More in details, the electric motor can be used to charge the battery absorbing the ICE torque, it can be in Zero Load conditions, which means not working, and it can be used to support the ICE during accelerations. On the engine side, it normally provides a higher torque than the requested one, to account for battery charging; moreover, pure ICE driving and catalyst heating operations are possible, but this were not simulated on the P2 hybrid vehicles. Similar to the EM, also the BSG can charge the battery, rotate in Zero Load operation and it can be used to provide additional boost. Later, the torque split modeling will be reported in details for the different powertrain layouts, based on the EMS analysis shown in the *Methodology* section.

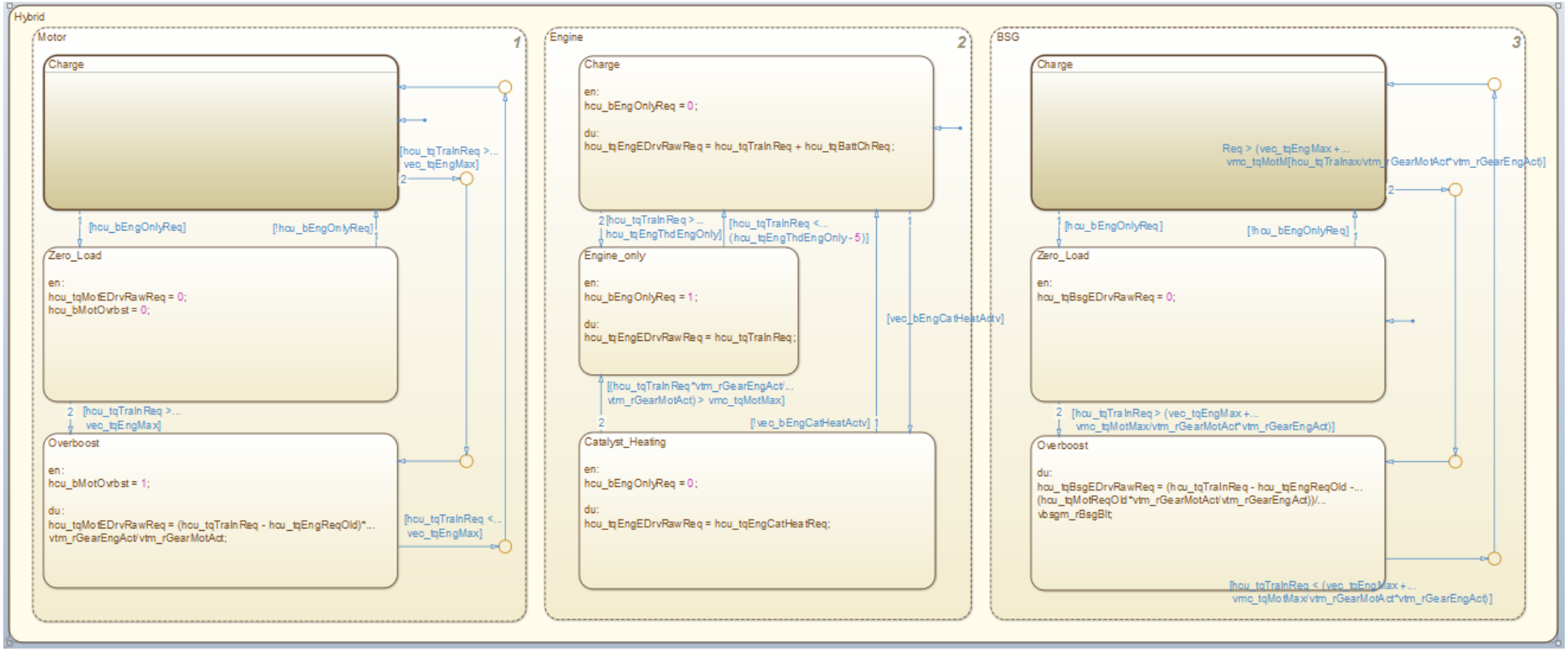


**Figure 81: Parallel hybrid operating mode decomposition**

For the sake of simplicity one can consider the following equation for motor torque request when the driving mode E-Drive is active:

$$tqMotDrvReq = \frac{tqWhlReq}{rGearMotAct} \tag{3-29}$$

Where: *tqMotDrvReq* is the motor torque request from the HCU model, *tqWhlReq* is the input driver wheel torque request and *rGearMotAct* is the actual driveline ratio, considering both gear and final drive. Moreover, the same equation is extended when hybrid mode is active:

$$tqMotDrvReq = \frac{tqWhlReq}{rGearMotAct} - tqEngReqOld \tag{3-30}$$

Where *tqEngReqOld* is the HCU engine torque request at the previous time step. The engine contribution is assessed by means of look up tables characterized during the experimental campaign, as shown in the vehicle analysis in the *Methodology* section. According to the driver request and the boundary conditions, three Hybrid driving mode can be defined:

$tqMotDrvReq < 0$ Charge Mode

$tqMotDrvReq > 0$ Boost Mode

$tqMotDrvReq = 0$ Engine-Only Mode

In addition to normal vehicle driving, a separate block is used to calculate the torque required for the engine start. According to the powertrain layout, the cranking torque can be provided by the traction motor (P2) or by the BSG (P0). The additional contribution due to the engine start accounts for the engine resistance and separation clutch torque capacity. On the other side, similar consideration can be done whenever there is a request for engine stop. In this sub-system the torque is calculated for the electric traction motor only. In this case, the motor torque request is equal to the torque requested at the wheels, scaled down by the driveline ratio:

$$tqMotStrtReq = \frac{tqWhlReq}{rGearMotAct} \tag{3-31}$$

Finally, the torque manager output merges the output of the different sub-systems, such as *E-Drive of parallel*, *Engine start* and *Engine stop* and limits the motor and engine torque requests to their physical limit, given as input for the simulation from technical datasheet. Afterwards, the HCU request is forwarded the respective slave controller to ensure the component operates within its limits for the next time-step.

The next sections will explore in details the different HCU characteristics for the tested powertrains.

**P0 EMS Modeling**

The P0 layout of Vehicle 1 represents the simplest test case of the prosed analysis, therefore, it was used as a starting point for the research activity. In the previous sections, the complete hybrid model has been explained; hereafter, more details are provided for the P0 logic modeling. In this regard, the 48V MHEV is not capable of pure electric driving or Load Point Shift Operations, hence, the *Torque Manager State* has to account for the standard BSG working conditions, such as: Boosting, Braking (so Recuperation) and finally the Sailing function. During Boosting, the BSG supports the ICE, while during decelerations it is used to regenerate electrical energy; under a calibrated vehicle speed threshold, the regenerations is off and the BSG acts as a pure brake. As one can see from Figure 82, all the working mode are reported in the state machines, including the double function of idle sailing and ICE-off sailing. The Pre-Sailing function is a time-based state used to prevent the ICE to go off/idle immediately, hence not being ready in case of a sudden driver change of mind.

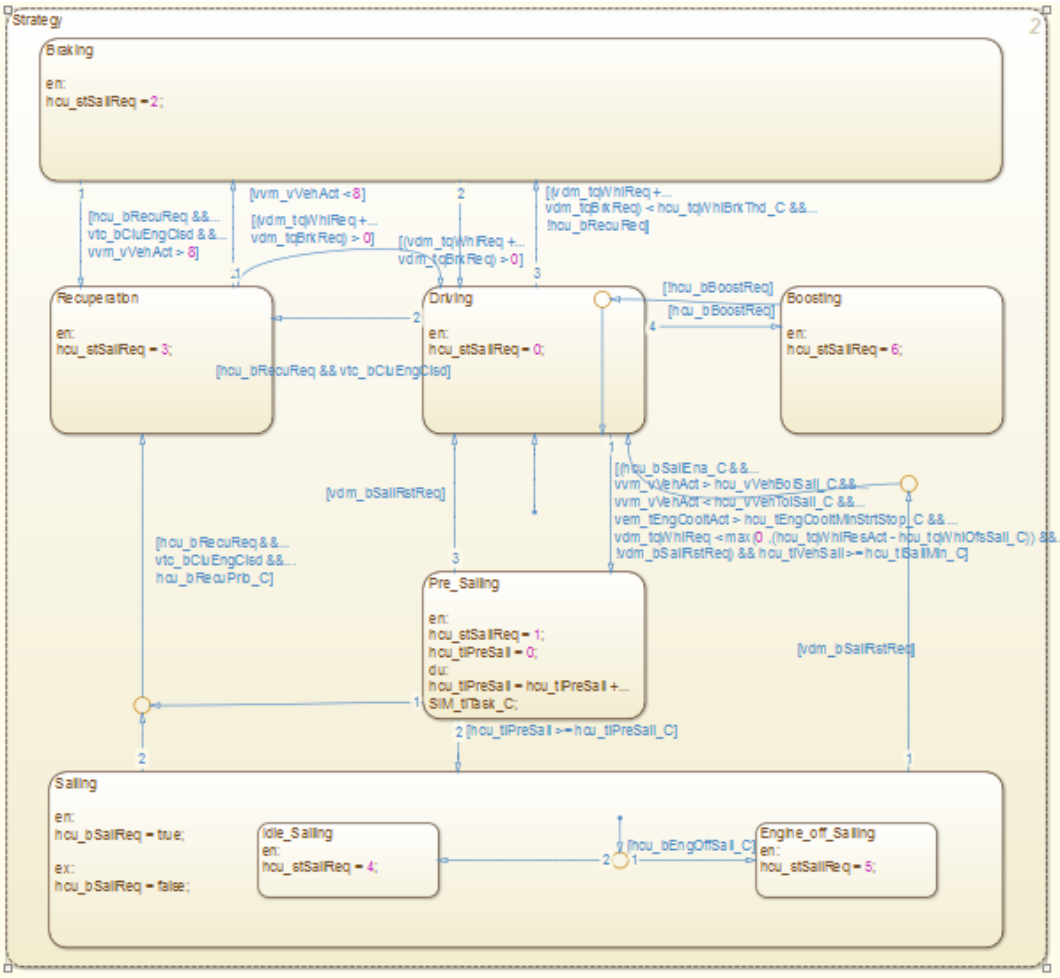


Figure 82: P0 hybrid operating mode decomposition

Once the operating mode status has been decided, the value activates the dedicated toque calculation block. To this extent, whenever the vehicle decelerates, the BSG is activated to provide a braking effect and recover electric

energy for the 48V battery. The BSG regenerative absorbed torque is calculated as follows:

$$tqBsgRegen = \frac{tqBrkReq}{\tau_{belt}} \tag{3-32}$$

Where *tqBsgRegen* is the requested torque absorbed by the BSG, *tqBrkReq* is the driver torque brake request and $\tau_{belt}$ is the belt ratio. On one side, the BSG is sometimes used to provide mechanical energy through the belt connection; in one case, it can be used for the sailing function. In this situation, if the torque request is below the maximum peak torque, the sailing contribution is calculated as follows:

$$tqBsgSail = \min\left(\frac{tqTraIn}{\tau_{belt}}, tqBsgMaxPeak\right) \tag{3-33}$$

Where *tqBsgSail* is the requested torque given by the BSG to move the vehicle, *tqTraIn* is the total transmission input torque and *tqBsgMaxPeak* is the BSG maximum peak torque allowed. On the other side, the BSG can support the ICE whenever there is the need of additional torque and the ICE contribution is already saturated. In this regard, the BSG support is computed according to the following equation:

$$tqBsgBoost = \frac{tqEngReq - tqEngMax}{\tau_{belt}} \tag{3-34}$$

Where *tqBsgBoost* is the addition torque given by the BSG to assist the ICE, *tqEngReq* is the ICE requested torque, *tqEngMax* is the maximum torque allowed by the engine in that particular situation, according to the target values gathered from literature. All these calculation are reported in the three blocks of Figure 83: in each block the previously equations are developed; later, the different contributions are summed up to obtain the final BSG torque request.

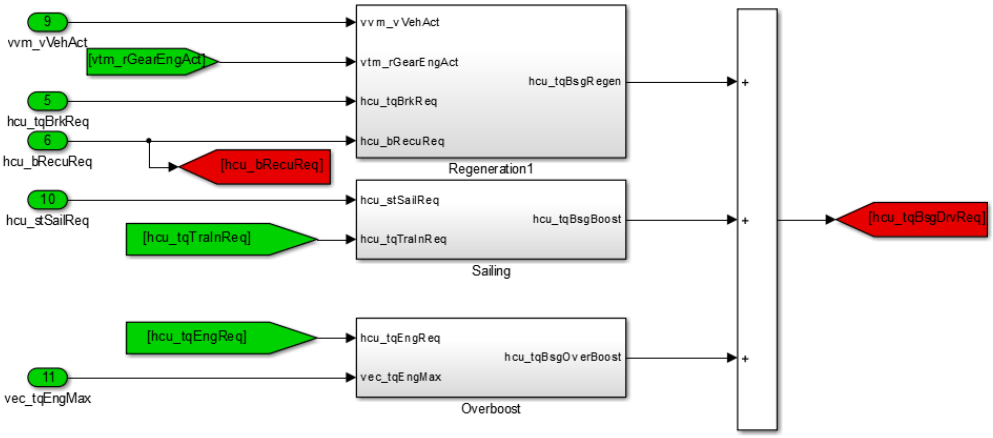


Figure 83: BSG Drive torque calculation

**P2 EMS Modeling**

The P2 case constitutes a more complex test case to investigate, due to the mechanical layout arrangement and the higher voltage and power involved at powertrain level, which results in advanced vehicle functionalities. Hence, this means that a P2 PHEV can operate either in pure electric mode or in hybrid mode, in the already explained LPS operation. To this regard, the content of Figure 78 has already been discussed; more in details, the following lines will explore the control logics behind the driving mode decision.

As depicted in Figure 84, the following rules shall be fulfilled for the hybrid mode request to become 'true':

- Alternatively, one of the following conditions is true:
  - The actual vehicle speed is above a calibrated threshold, that is a function of HV battery SOC and torque request at the wheels, as found out during the experimental campaign;
  - The actual power request at the wheels is above a calibrated threshold, that is a function of the product between vehicle speed and acceleration, gear engaged and HV Battery SOC;
- Driver wheel torque request shall be higher than 0, which means that the vehicle is not decelerating;
- The HV battery SOC is lower than a calibrated threshold, found to be the maximum level at which the CS mode can be activated;
- The vehicle speed is higher than a minimum value, since at very low speed the ICE is always shut off;
- When a kick-down request comes from the driver side, all the above listed conditions do not need to be verified.

On the other side, as depicted in Figure 85, the following rules shall be fulfilled for the E-Drive mode request to become 'true':

- Vehicle speed must be lower than a maximum allowed value;
- The HV battery SOC is higher than a calibrated threshold, found to be the minimum level at which the CD mode can be activated;
- The actual vehicle speed is below the previously calibrated threshold, scaled down by an arbitrary factor to avoid sudden change in driving mode request;
- The kick-down is not requested by the driver;
- Engine coolant temperature is above a certain threshold;

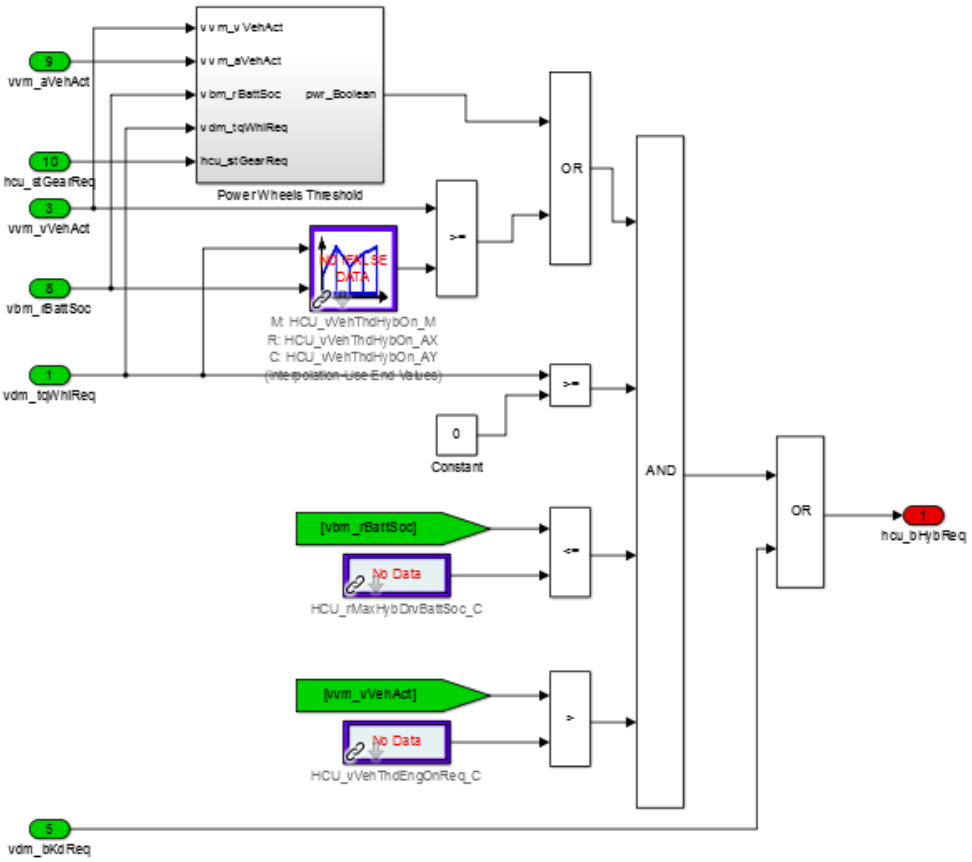


Figure 84: Rules for the hybrid mode request

Once the driving mode has been selected, the related status are activated for the torque calculation; it has already been explained that how the torque split between the motor and engine is actuated in the *E-Drive or parallel* block. For more details, Figure 86 and Figure 87 illustrates the input variables involved in the torque split calculation, for Vehicle 2 and Vehicle 3 respectively: as expected, the main signal is the transmission input torque, derived from the torque wheel request coming from the driver model, which has to be divided between the different "machines". At the same time, the ICE contribution is another relevant input to be considered in order to replicate the load point shift operation. Additionally, the torque provide by the ICE in pure ICE driving situation is considered by means of a map. Depending on the results coming from the experimental campaign, either the whole ICE torque or the specific charging contribution were mapped, as can be seen from the different logics described in the following pictures.

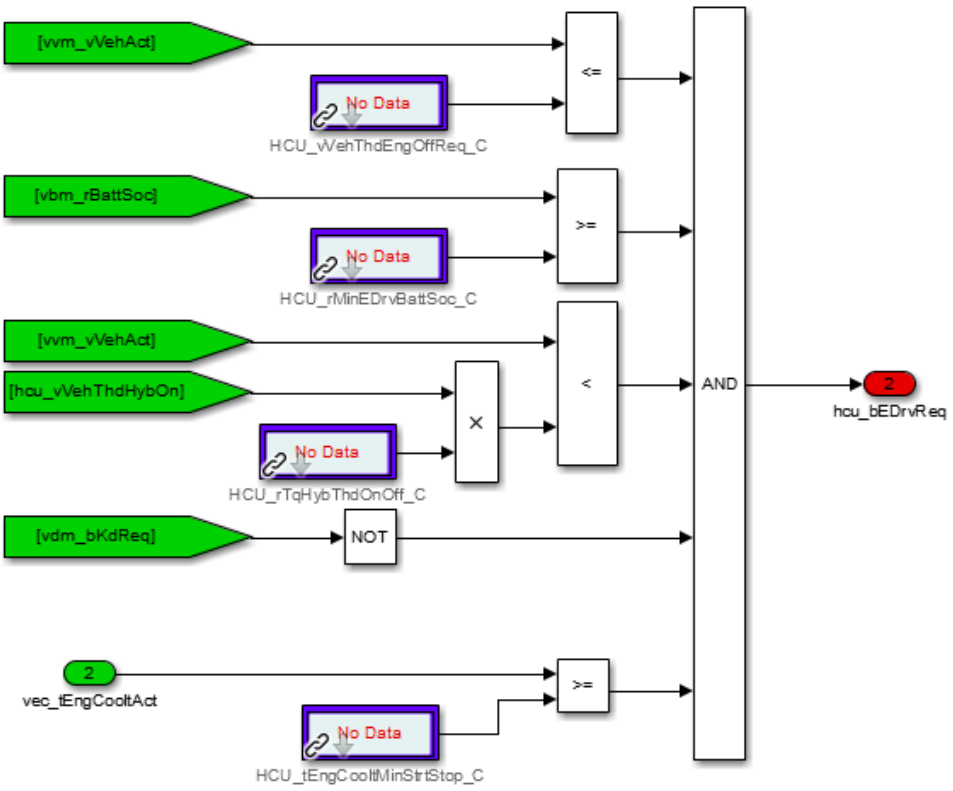


Figure 85: Rules for the E-drive request

In particular, Figure 86 shows the main input signals for the torque split calculation of Vehicle 2: from the experimental campaign (see Figure 47), the ICE behavior was mapped as a function of vehicle speed, gear engaged and driving mode (charge or boost), used as input for the *LPS or Boost* sub-system. For the sake of brevity, only the upper part of the state machine is shown, since the other variables involved in the block can be considered secondary variables. Similarly, Figure 87 shows the main input signals for the torque split calculation of Vehicle 3: from the experimental campaign (see Figure 58): the ICE charging torque was mapped, instead. In this case, the output of the look-up table depends on the gear engaged and the torque requested at the wheels and it is used whenever the boost request is not active, as illustrated in the switch block.

Hence, the output of the look-up tables is compared to the transmission input torque as in equation (3-35) for Vehicle 2, otherwise is later added in the state machine according to equation (3-36) for Vehicle 3:

$$tqBattChReq = tqEngLPSBoost - tqTraInReq \tag{3-35}$$

$$tqBattChReq = f(vVehAct, rBattSOC, stGear) \tag{3-36}$$

As it can be notice from both pictures, the other inputs of the state machine are the ICE, EM and BSG torque calculated at the previous time step of the simulation. As already mentioned, the possibility to run in pure ICE mode can be taken into account, based on the output of a calibrated torque threshold, function

of HV Battery SOC. However, this case was never found in real vehicle driving, thus, it was not included in the simulation cases.

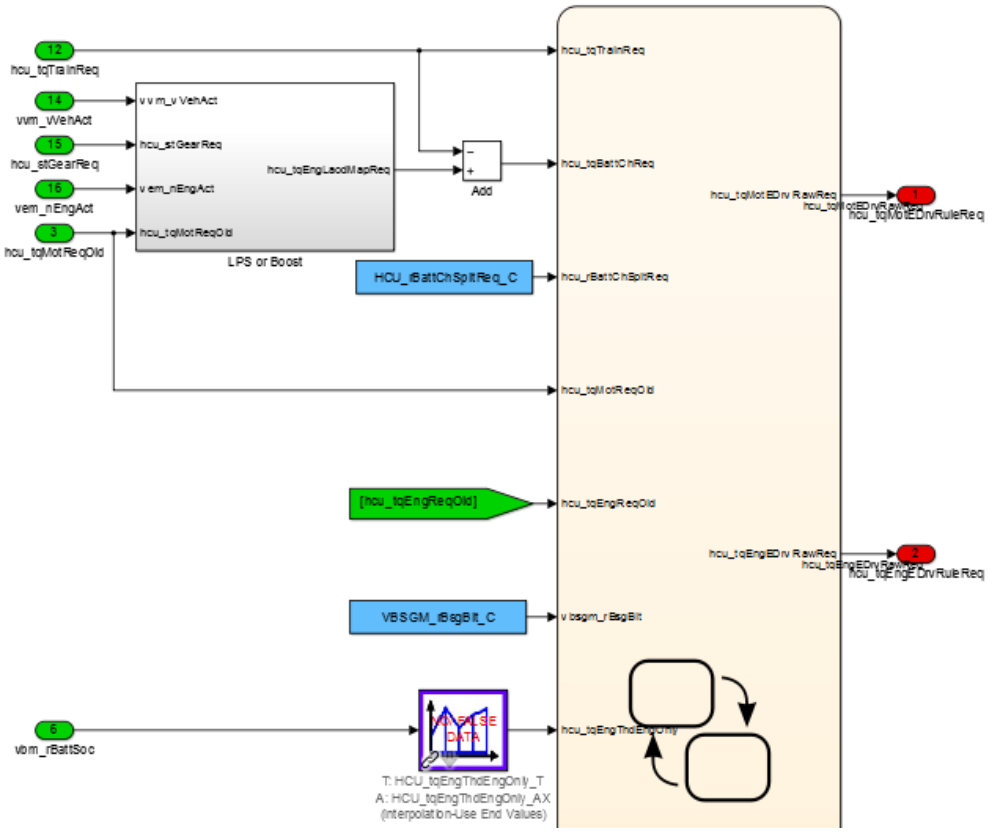


Figure 86: Vehicle 2 E-Drive or Parallel input layer

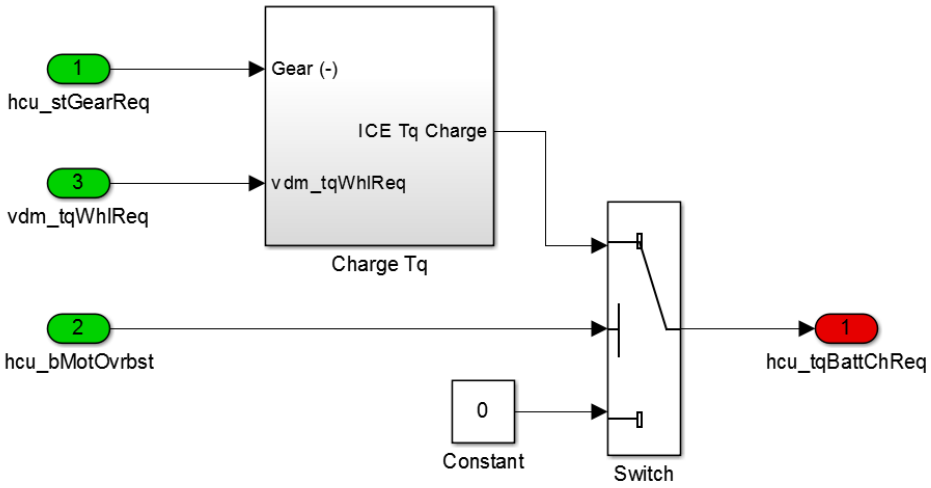


Figure 87: Vehicle 3 ICE charge torque request layer

# Chapter 4

# Results and Discussion

Part of the work described in this Chapter was previously published in the following publications:

- DiPierro, G., Millo, F., Scassa, M., and Perazzo, A., "An Integrated Methodology for 0D Map-Based Powertrain Modelling Applied to a 48 V Mild-Hybrid Diesel Passenger Car," SAE Technical Paper 2018-01-1659, 2018, https://doi.org/10.4271/2018-01-1659.
- DiPierro, G., Millo, F., Tansini, A., Fontaras, G. et al., "An Integrated Experimental and Numerical Methodology for Plug-In Hybrid Electric Vehicle 0D Modelling," SAE Technical Paper 2019-24-0072, 2019.

This chapter will present the results of the previously introduced comprehensive hybrid electric vehicle model calibration, based on the experimental data and powertrain reverse-engineering illustrated both in *The Integrated Methodology* and in *The Comprehensive xEV Model* chapters. In order to have a reliable simulation tool, the most important quantities involved in a hybrid electric powertrain will be simulated, such as the HEV mode request, the torque split between the ICE and the EM, the battery current and SOC. All these variables are important in fuel consumption, $CO_2$ and emission estimation.

In the first part, the calibration of the model for the three investigated vehicles will be presented considering the NEDC and the WLTC driving cycles. The focus is the EMS and the simulation of the instantaneous $CO_2$ emissions, which are relevant in the TA procedure. Moreover, a thorough analysis will be presented for Vehicle 3, considering both the CD and the CS tests. The core is represented by the correct detection of the EMS for the NEDC and WLC and on the simulation of the instantaneous CO2 emissions during the TA cycles.

In the second part, the predictive capabilities of the model will be proved over the WLTC, as for Vehicle 2; while Vehicle 3 functionalities will be tested along the more demanding and more realastic RDE procedure. The focus is to obtain a

reliable estimation of the energy management as well as of the fuel consumption and $CO_2$ emissions.

## 4.1 Driving Cycle Simulation

This section reports the results of the 0D map-based model calibration process, carried out via driving cycle simulation. The set of data collected during the experimental campaign will be used as a reference for accuracy assessment. It is preferred to perform the model calibration over a driving cycle in order to benefit from the standard and less dynamic characteristics, but mainly because the model itself is intended to be used for vehicle/powertrain potentialities estimation over TA driving cycles. Other than the EMS model calibration in terms of power split between the ICE and the electric machine (s), this section aims at calibrating the vehicle model also on the electrical request side, and for $CO_2$ and Fuel consumption calculation, whenever this is possible.

### 4.1.1 Vehicle 1 Simulation

Vehicle 1 was the first test case investigated with proposed methodology due to the relatively simple technological content. Hence, as a preliminary step, the vehicle and EMS models calibration was carried out by comparing the total power at the clutch between the engine and the DCT, calculated as the sum of the ICE and BSG contribution; the signals of torque and speed were acquired from the OBD network. Thus, total power was calculated as follows:

$$P_{TOT} = T_{ICE} \cdot \omega_{ICE} + T_{BSG} \cdot \omega_{BSG} \tag{4-1}$$

Where $T$ is torque and $\omega$ is the rotational speed. The reliability of the signal was cross-checked with the measured electrical power and considering suitable values for BSG and belt efficiencies. On the left side of Figure 89 the results for the simulated and measured power at the clutch over a WLTC are shown, divided into four subplots for the four cycle phases. As it can be noticed, the power calculation is in good agreement with the experimental data. In particular, the model sometimes overestimates the power request for the first 1000 seconds, especially in dynamic phases. This is true at low-medium speed, due to the approximation of the implemented BSG working strategy. However, the simulated power matches very well the experimental one, also during acceleration at low speed. In general, with a more accurate knowledge of BSG/Inverter/belt group losses and the transmission efficiency, the gap could be reduced. As for the second part of the cycle (high-load, high-speed), the power request captures very well the experimental trend, both during acceleration and steady phases, due to the main contribution given by the ICE. The almost-constant speed part form second 1200 to 1350 represents a good example of model capabilities.

Once the vehicle model, hence the torque split was calibrated in terms of power request at the clutch, the $CO_2$ emissions simulation was set as target, which represents a key parameter for vehicle classification. Since the engine-out emission probe of Vehicle 1 was not set, $CO_2$ produced was not available for the engine model. In this regard, the $CO_2$ map from another diesel engine (In-line 4 cylinders 1.6l Turbocharged Diesel) was used as baseline, and later tuned for model calibration. After the first-tentative WLTC baseline simulation, the tuned maps were re-implemented in the vehicle model and simulation was repeated. The process was run iteratively until an acceptable gap, both on the instantaneous and cumulative $CO_2$, was found, resulting in the $CO_2$ flow rate map illustrated in Figure 88, where the higher $CO_2$ production happens at high load and speed. It is worth to mention that both the CO2 map and the measured $CO_2$ were calculated from the fuel consumption available form CAN-bus network, applying the following equation:

$$CO_2[g/s] = \alpha \cdot FC[g/s] \tag{4-2}$$

Where alpha is a factor equal to 3.16, calculated considering the complete combustion of a diesel fuel that contains approximately 86% of Carbon and 16% of Hydrogen in mass, with a density of 835 g/l.

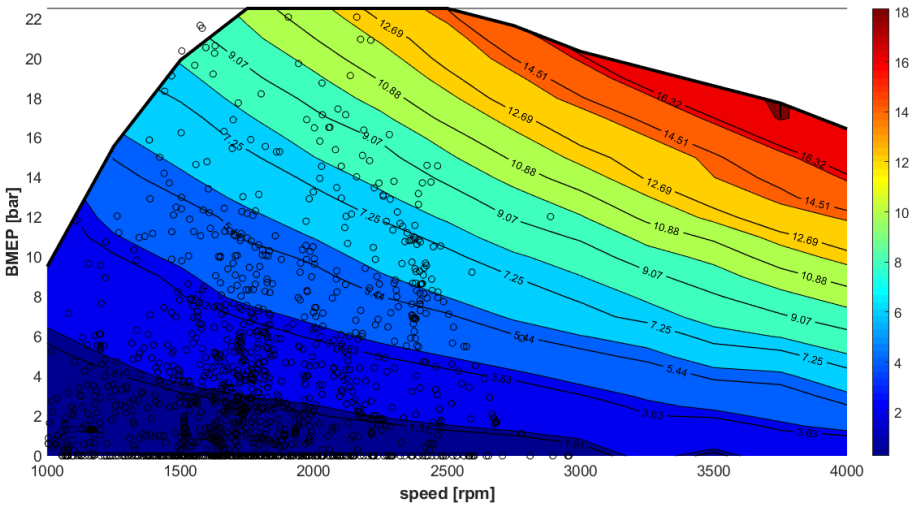


**Figure 88: Vehicle1 $CO_2$ flow rate [g/s] calibrated map and WLTC ICE operating points (black)**

Hence, on the right side of Figure 89 the instantaneous $CO_2$ flow rate is shown: the model prediction shows a good agreement with the experimental data, even though it overestimates it, especially during highly dynamic transients. On average, the simulated flow rate is within a ±5% range around the experimental values.

In addition to the WLTC, the NEDC cycle was carried out on the same chassis dyno and later simulated. In this case, the lower mass and the less aggressive speed profile characterize the smoother cycle. As a result, the model captures very well the power requested at the clutch, as shown on the left side of

Figure 90. Likewise, the $CO_2$ flow rate matches the experimental data, as shown on the right side of Figure 90. As for the total $CO_2$ production, the transient behavior is balanced by the calibrated EMS, hence, the $CO_2$ over the whole driving cycle is in good agreement with the experimental values. As a confirmation, Figure 91 reports the cumulated $CO_2$ emission over the WLTC (left) and the NEDC (right), as it can be noticed, the gap between the simulated and experimental data is 1.4% and 0.9% respectively. To summarize, with the steady-state map-based proposed approach, an estimation of the produced $CO_2$ is given, which is acceptable if low computational effort and time are required.

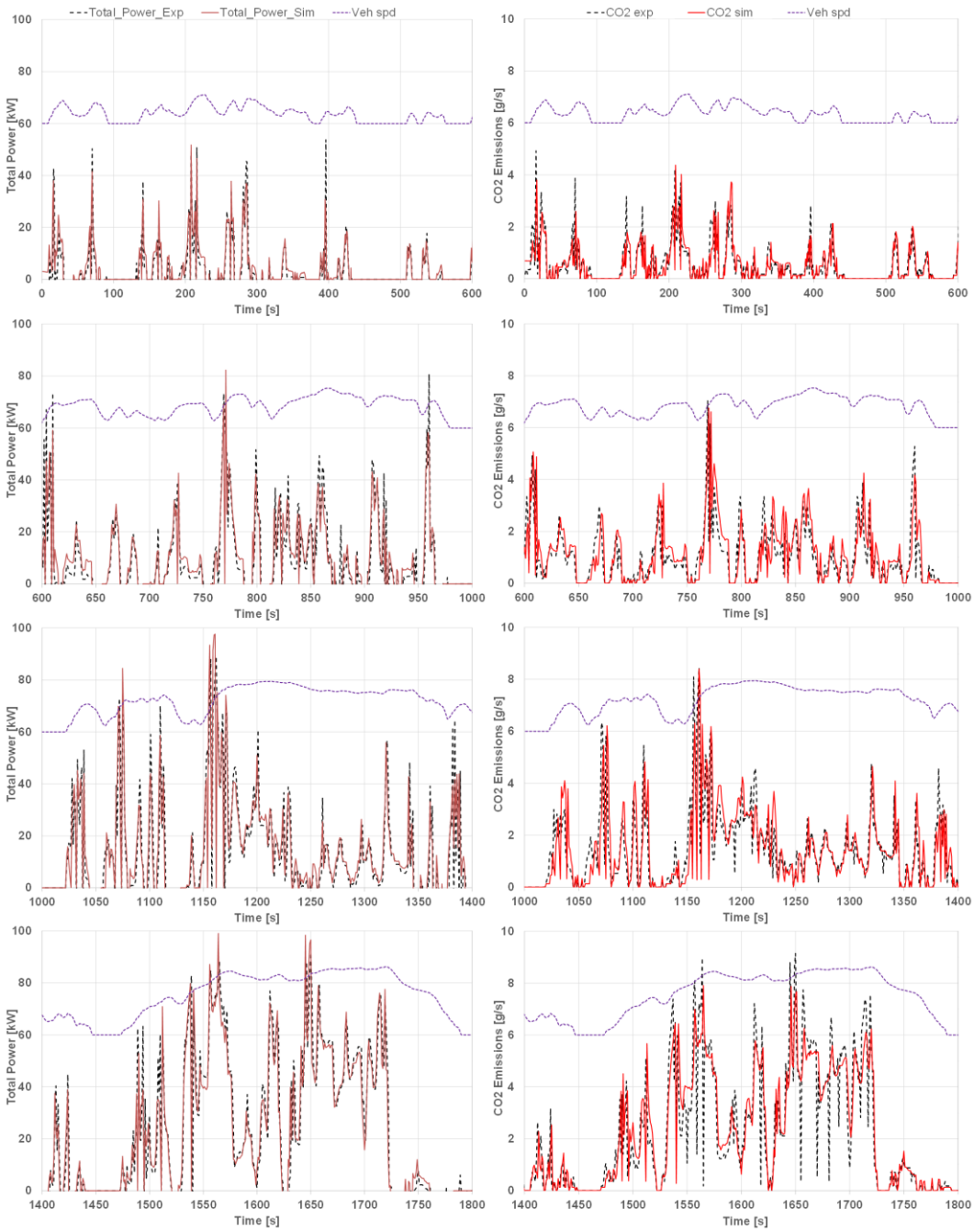


**Figure 89: Vehicle 1 - Experimental (black dashed) and simulated (red solid) power at the clutch (left), $CO_2$ flow rate (right) with vehicle speed profile (top dotted) over the four WLTC phases**

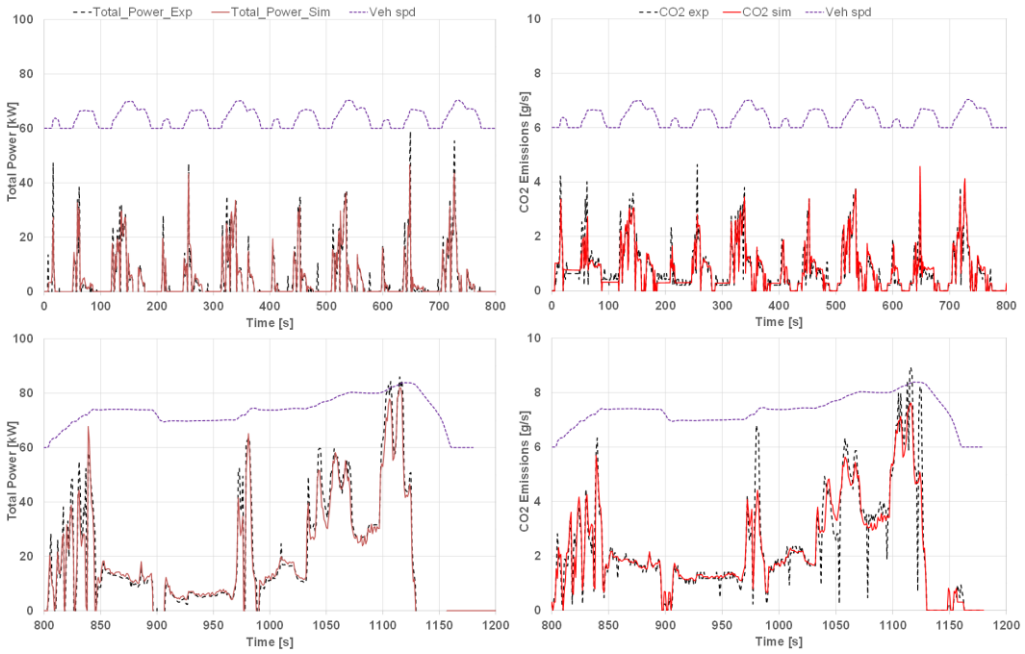


**Figure 90: Vehicle 1 - Experimental (black dashed) and simulated (red solid) power at the clutch (left), $CO_2$ flow rate (right) with vehicle speed profile (top dotted) over the urban (top) and extra-urban (bottom) NEDC phases**

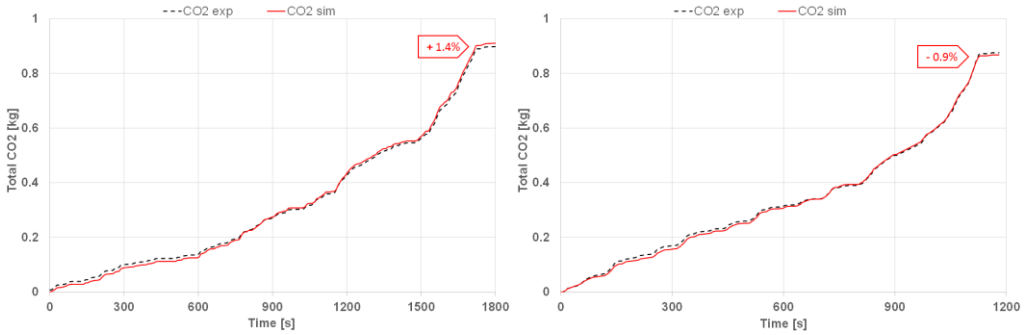


**Figure 91: Vehicle 1 - WLTC (left) and NEDC (right) experimental (black dashed) and simulated (red solid) cumulated $CO_2$ emissions**

### 4.1.2 Vehicle 2 Simulation

Vehicle 2 represents a further step into the development of the proposed methodology, especially on the modelling side due to the higher system complexity in comparison with Vehicle 1. Hence, as already illustrated in the *Methodology* section, the EMS was deeply investigated in order to properly predict the torque split and the related electrical consumption, for both the EM and the HV battery. Unfortunately, due to the requirements of the project, the engine-out side was not instrumented; moreover, fuel or $CO_2$-related signals were not available on the CAN-bus network. For this reason, Vehicle 2 simulation is strictly focused on the EMS re-engineering.

To this regard, the vehicle model was validated along the NEDC cycle; to be more specific, the whole process of powertrain characterization was based on the set of data collected during the entire experimental campaign, however, the

NEDC cycle was adopted to further fix the model parameters, due to its simplicity. As previously seen for Vehicle 1, the power at the clutch was calculated as the sum of the ICE, EM and HSG powers, reading torque and rotational speed from CAN. The following equation is used to compute the total power:

$$P_{TOT} = T_{ICE} \cdot \omega_{ICE} + T_{EM} \cdot \omega_{EM} + T_{HSG} \cdot \omega_{HSG} \quad (4\text{-}3)$$

Where $T_{ICE}$, $T_{EM}$ and $T_{HSG}$ are the ICE, the EM and the HSG torques respectively, while $\omega_{ICE}$, $\omega_{EM}$ and $\omega_{HSG}$ are the respective rotational speeds. To further confirm the CAN signals reliability, the EM mechanical power was compared to the electrical measured power, provided by the electrical sensor. It is worth to mention that the HSG contribution can be considered negligible over a driving cycle, because it is usually adopted for starting and stopping the engine. Hence, the presented analysis is focused on speed and torque signals from the ICE and EM, other than the HV battery.

The NEDC was carried out in hot condition at low initial battery SOC, applying the EMS logic reported in Figure 45 and Figure 47. To this regard, the vehicle speed (top) and the total power from the ICE, EM and HSG over the cycle (bottom) are illustrated in plot (a) of Figure 92; the total power at the clutch is well captured and the model prediction is accurate enough, both in EV mode and Hybrid mode. It is worth to mention that the experimental power at the clutch is derived from the power at the wheels, in order to compare the powertrain input with the request coming from the driver. The ICE torque (top) and speed (bottom) are shown in Plot (b): a good agreement with the experimental data can be highlighted for both signals. The NEDC is driven in pure EV mode for the 75% of the time, turning on the ICE in the high-speed area around 70 km/h, when battery SOC is at its minimum (~11%); later, the ICE goes off during deceleration. With the ICE on, the EM works as a generator; however, at higher speed, the powertrain alternatively operates in charge and boost mode. As noticed, the engine works at constant load in charge mode (EM torque<0), whereas the ICE torque raises linearly during acceleration on boost mode (EM torque>0). In plot (c) of Figure 92, the EM torque (top) and speed (bottom) are shown; the EM behavior is simulated accurately with positive and negative torque. The negative torque peaks are due to the deceleration phases, where the EM accounts for the regenerative braking. In the last plot (d), the HV side is investigated with the battery DC current (top), battery electric power (center) and battery SOC (bottom). Similarly to the EM output, both current and power (i.e. voltage) show good agreement with the measured quantities; as a consequence, the battery SOC is well predicted. To summarize, a good accuracy in the prediction of the power split and in the calculation of the related electrical quantities of the P0-P2 architecture is shown by the model.

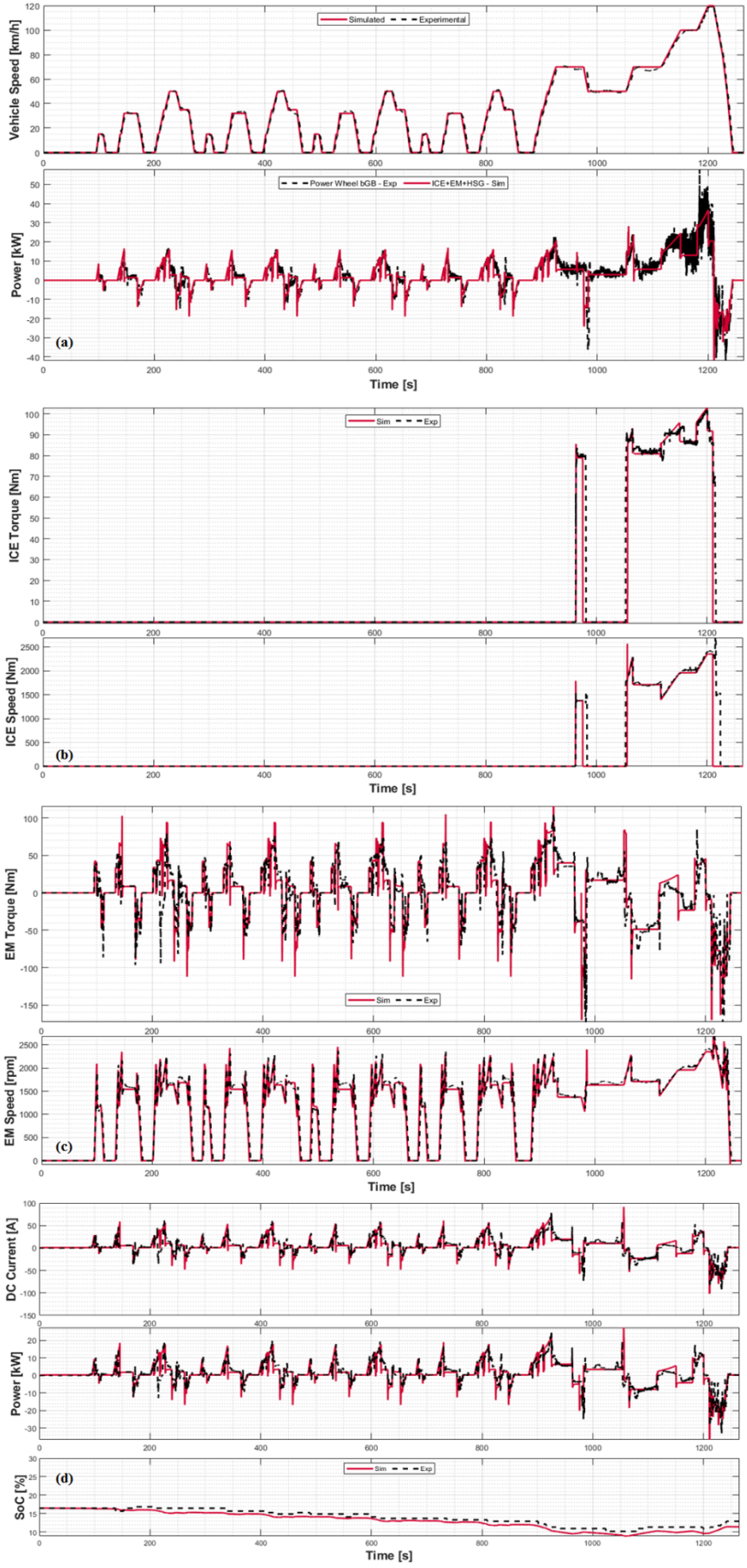


**Figure 92: Vehicle 2 - Experimental (black dashed) and simulated (red solid) results over the mid-SOC NEDC**

### 4.1.3 Vehicle 3 Simulation

Vehicle 3 represents the last step of the presented methodology, due to the high-level complexity coming from a state-of-the-art Diesel P2 PHEV. As introduced in the *Methodology* section, the powertrain components and the EMS were analyzed to assess the power split and the vehicle electrical consumption, related to the EM and the HV battery. As a further investigation, this vehicle was part of a bigger project within FEV, hence the engine-out side was instrumented and it was possible to characterize the fuel consumption and $CO_2$ emissions, as reported later in this section. For this reason, Vehicle 3 is clearly the activity that collects all the previous achievement in terms of EMS reverse-engineering and $CO_2$ emissions simulation.

In order to have a robust simulation tool, the vehicle model was validated along the NEDC and WLTC cycle performed in CD and CS conditions. As previously mentioned, the whole powertrain characterization was based on the set of data gathered during the entire experimental campaign, however, the two TA cycles were used as a proving ground for tuning the model parameters, Likewise, the power at the clutch was calculated as the sum of the ICE and EM powers, reading torque and rotational speed from CAN. The following equation is used to compute the total power:

$$P_{TOT} = T_{ICE} \cdot \omega_{ICE} + T_{EM} \cdot \omega_{EM} \tag{4-4}$$

Where $T_{ICE}$, and $T_{EM}$ are the ICE and the EM torques respectively, while $\omega_{ICE,}$ and $\omega_{EM}$ are the respective rotational speeds.

**CHARGE DEPLETING**

The first step of the model calibration was, as expected, the CD simulation with very high initial battery SOC, in order to accurately calibrate the powertrain and vehicle model without being affected from the ICE intervention. To this regard, the NEDC starts at 66% battery SOC, while the WLTC at 100% battery SOC; both cycles were performed in warm conditions after a pre-conditioning run. Similarly to the plot used for Vehicle 2, Figure 93 and Figure 94 illustrates the main output of the NEDC and WLTC in pure electric mode, respectively.

As far as the NEDC is concerned (Figure 93), plot (a) shows vehicle speed (top) and the total power over the cycle (bottom); the total power at the clutch shows good agreement with the experimental one, derived from power at the wheels as a further comparison of the reliability of the model. Good results are achieved both in steady and dynamic driving. Plot (b) shows that the EM torque (top) and speed (bottom) are accurately simulated both in motoring (positive) and generator (negative) mode; as it could be expected from the good results in terms

of total power at the clutch. Thanks to having mapped-out the regenerative contribution (see Figure 54), the negative torque is well captured, showing a small overestimation during regeneration. The HV side is investigated in the last plot (d), showing the battery DC current (top), battery electric power (center) and battery SOC (bottom). The current and power (i.e. voltage) have the same trend and they show a good match with the measurements; both in charging (negative current) and discharging (positive current) phases. As a results, the battery SOC estimation is accurately performed over the entire cycles, which starts at 66% and ends around 45%. As can be noticed, the current and power overestimation in the final seconds leads to a smaller deviation in the battery SOC signal, which is below 1%.

Moreover, the model calibration was also carried out on a hot-WLTC in CD conditions, as depicted in Figure 94. Using the same plots seen before, it can be noticed from plot (a) that the driver is capable of following the more aggressive speed profile and the powertrain total torque provided at the clutch (bottom) shows very good agreement with the experimental data, in all driving conditions. Also in the case where higher torque and power are involved, the EM model accurately calculates its power and speed as shown in plot (b). Again, a small overestimation of the regenerative contribution can be noticed for negative torque values, especially in the first deceleration where the battery is still full and the current gets limited, as shown in the third plot. As a matter of fact, plot (c) indicates that also the main variables on the HV side are simulated accurately, as for the battery current and power. As a consequence, the battery SOC trace matches very well the experimental one, both when charging and discharging, meaning that a thorough battery characterization leads to a good estimation of the main signals involved.

**CHARGE SUSTAINING**

The second step of the model calibration consisted in the NEDC and WLTC simulation in CS mode carried out at very low battery SOC, including the cold-start condition as required from TA regulation, for the implementation of the EMS logics reported in Figure 56 to Figure 58.

Starting with the NEDC in CS mode, plot (a) of Figure 95 illustrates the speed profile and the power requested at the clutch, which are accurately simulated as already proven in CD conditions. In this case, a new plot was added in order to analyze the ICE behavior due to the hybrid mode request, as shown in plot (b). As it can be noticed, both the ICE torque and rotational speed are well captured over the entire cycle; more in details, the model is capable of predicting not only the absolute torque values, but also it accurately replicates the instants for ICE on and off events, according to the maps extracted from the experimental campaign. Only around second 950 the model does not turn off the engine, as done in reality. However, the EMS characterization gives reliable results allowing the engine to be on only after vehicle start-up and at higher speeds during the extra-urban

phase. As noticed, the ICE is widely used across the CS NEDC cycle, mainly for battery charging, rather than for boosting in combination with the EM, as confirmed from plot (c) of Figure 95. Here, the EM signals are plotted, showing a good agreement with the experimental data as for torque and speed correlation. It can be seen that for the majority of the cycle, the EM torque is negative, hence, it is used as a generator by the ICE to recharge the battery under the so-called LPS mode. The torque peaks not captured are related to the ICE off events that are not foreseen by the model, thus the EM do not steps in for propulsion. The fourth plot (d) reports the main signals of the HV side: as the CD case, the current, power and SOC are accurately calculated by the battery model, resulting in a SOC difference at the end of the cycle of about 2%.

Furthermore, the warm WLTC cycle in CS conditions was simulated (see Figure 96), in order to better tune the model parameters for a robust EMS simulation. As already demonstrated, plot (a) shows that the driver model and vehicle model provide accurate results in calculating the vehicle speed and power at clutch, also in dynamic conditions experienced during a WLTC. Thanks to the characterization of both the HEV mode request and the torque split in LPS mode, the ICE behavior is well predicted in terms of torque and speed, as depicted in plot (b). Despite the numerous ICE on/off events and the numerous transients, the EMS model shows an accurate match with the experimental data in turning on and off the engine at the right time, according to the boundary conditions of speed, torque at the wheels and SOC. Only few times before second 1200, the ICE is kept on by the model, due to some conditions not met for activating the EV drive request. However, this was chosen as the best calibration according to the numerous variables that are taken into account when dealing with the EMS. Similarly, plot (c) shows the results of the model for the EM in terms of torque and speed; again, the trend and the torque values are well captured. The model does not overshoot the torque required for vehicle start-up or for boosting, as can be seen from the different spikes of the experimental data. The issue encountered at second 1200 results in operating the EM as a generator; thus, the positive spikes visible for the dashed line are not simulated. The last plot shows the main signal of the HV side, such as battery current, power and SOC. Similar to the EM simulation, the battery current and power well matches the measured values, except for the instants in which the ICE behavior is not captured. As seen for the EM, the positive spikes in high-transient conditions are not fully captured; as a result, the battery energy is depleted at a slower rate for the first 700 seconds of the cycle. However, the battery SOC trend and the final SOC of 16% are caught, with a maximum deviation within 2% over the entire cycle.

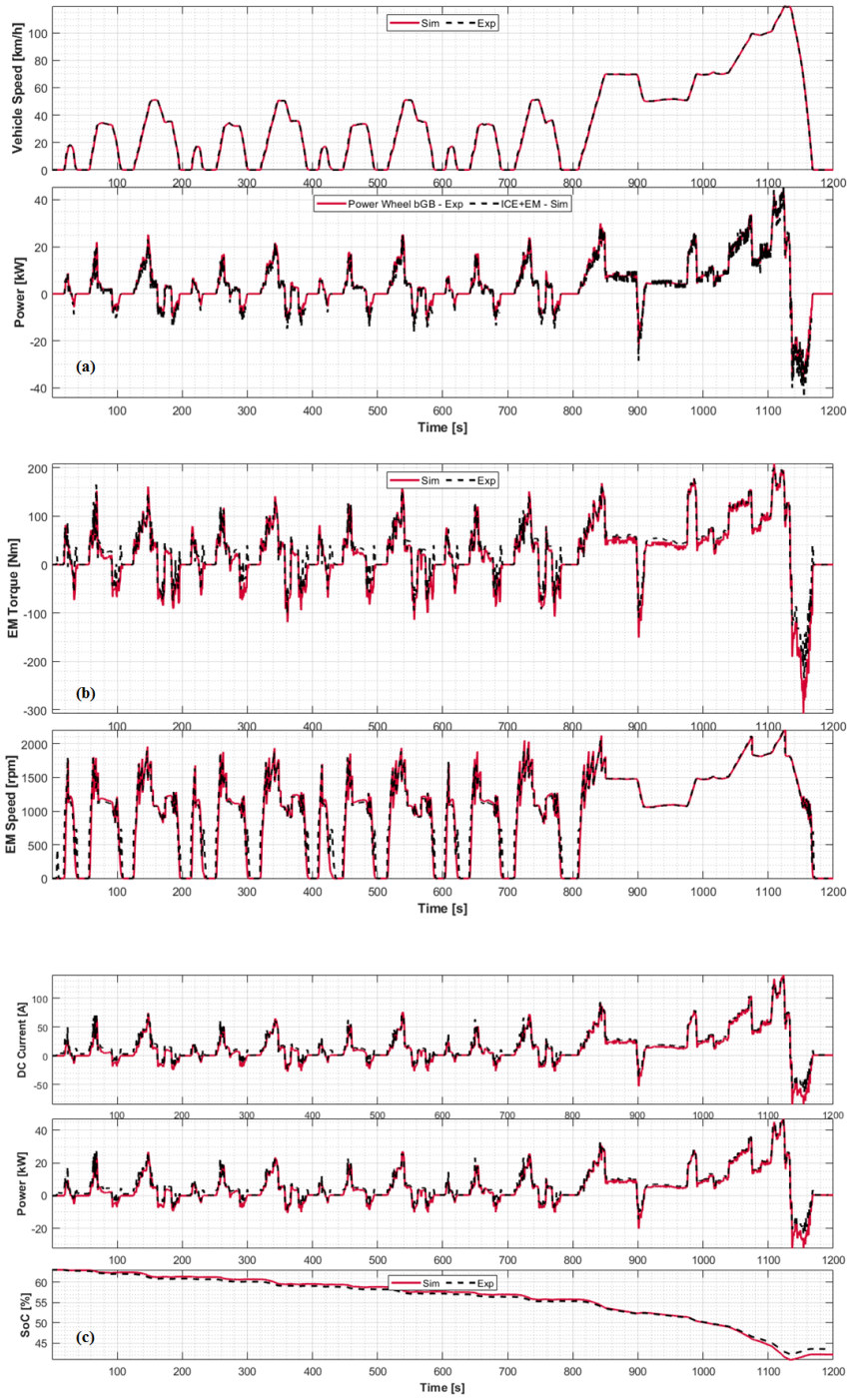


**Figure 93: Vehicle 3 - Experimental (black dashed) and simulated (red solid) results over the NEDC Charge Depleting CD**

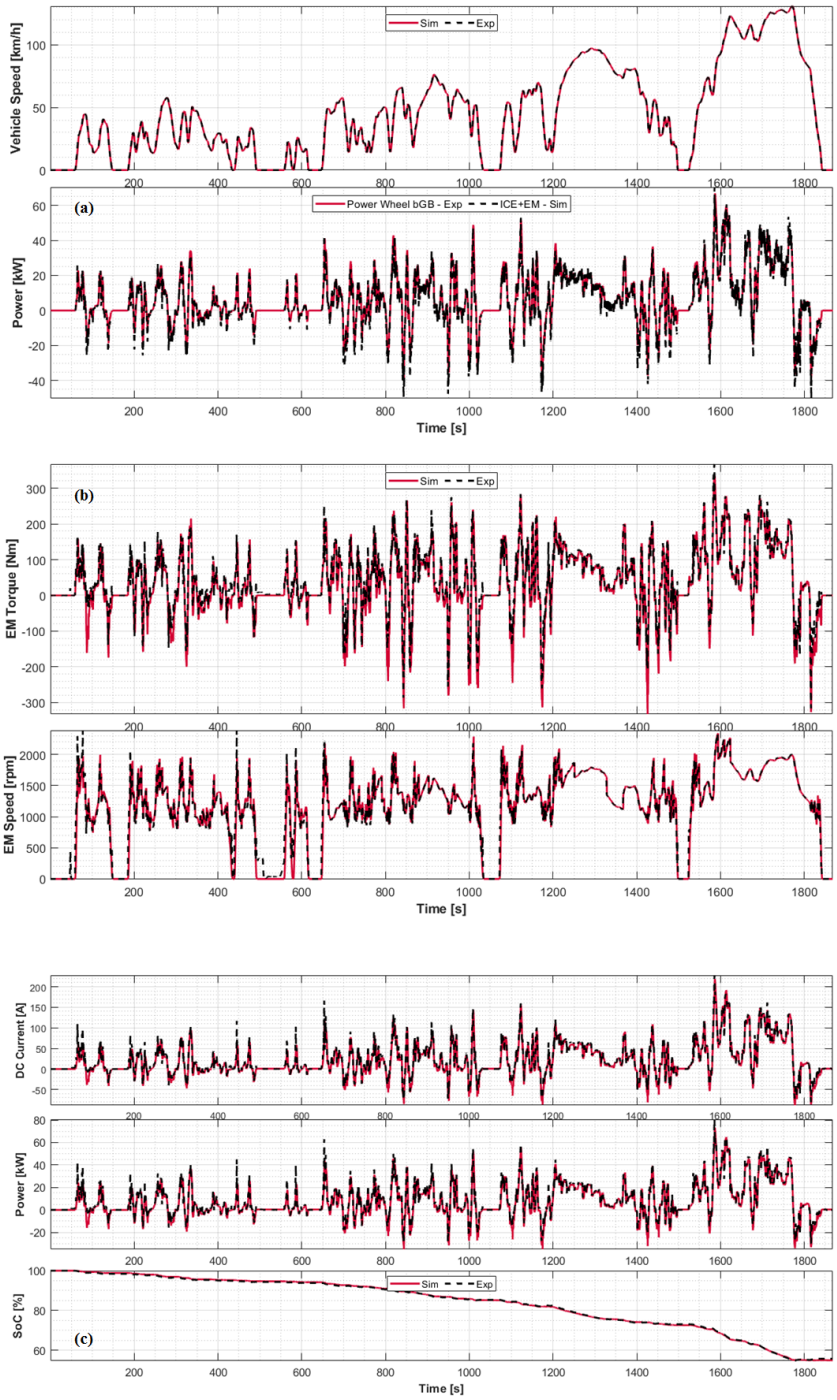


**Figure 94: Vehicle 3 - Experimental (black dashed) and simulated (red solid) results over the WLTC Charge Depleting CD**

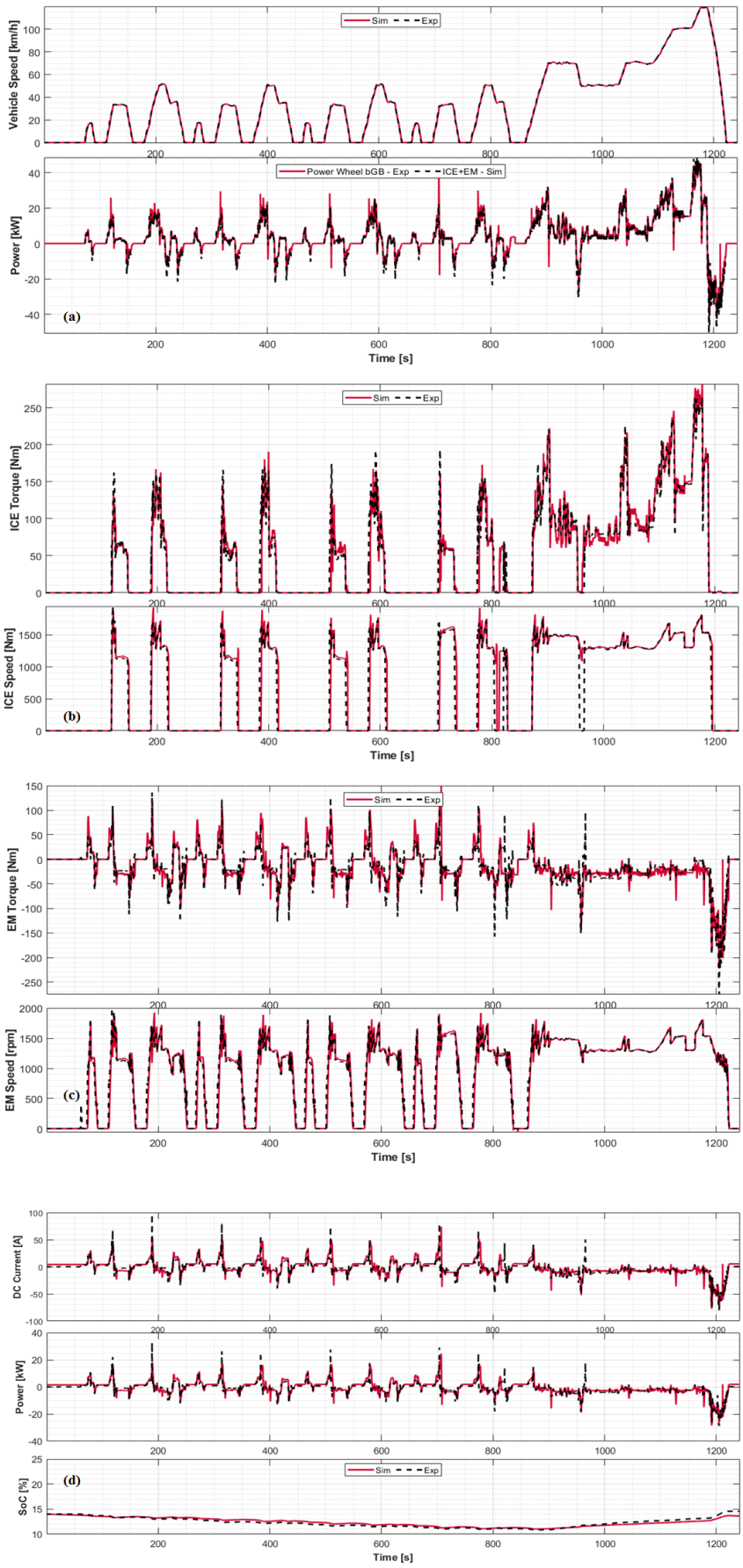


**Figure 95: Vehicle 3 - Experimental (black dashed) and simulated (red solid) results over the NEDC Charge Sustaining CS**

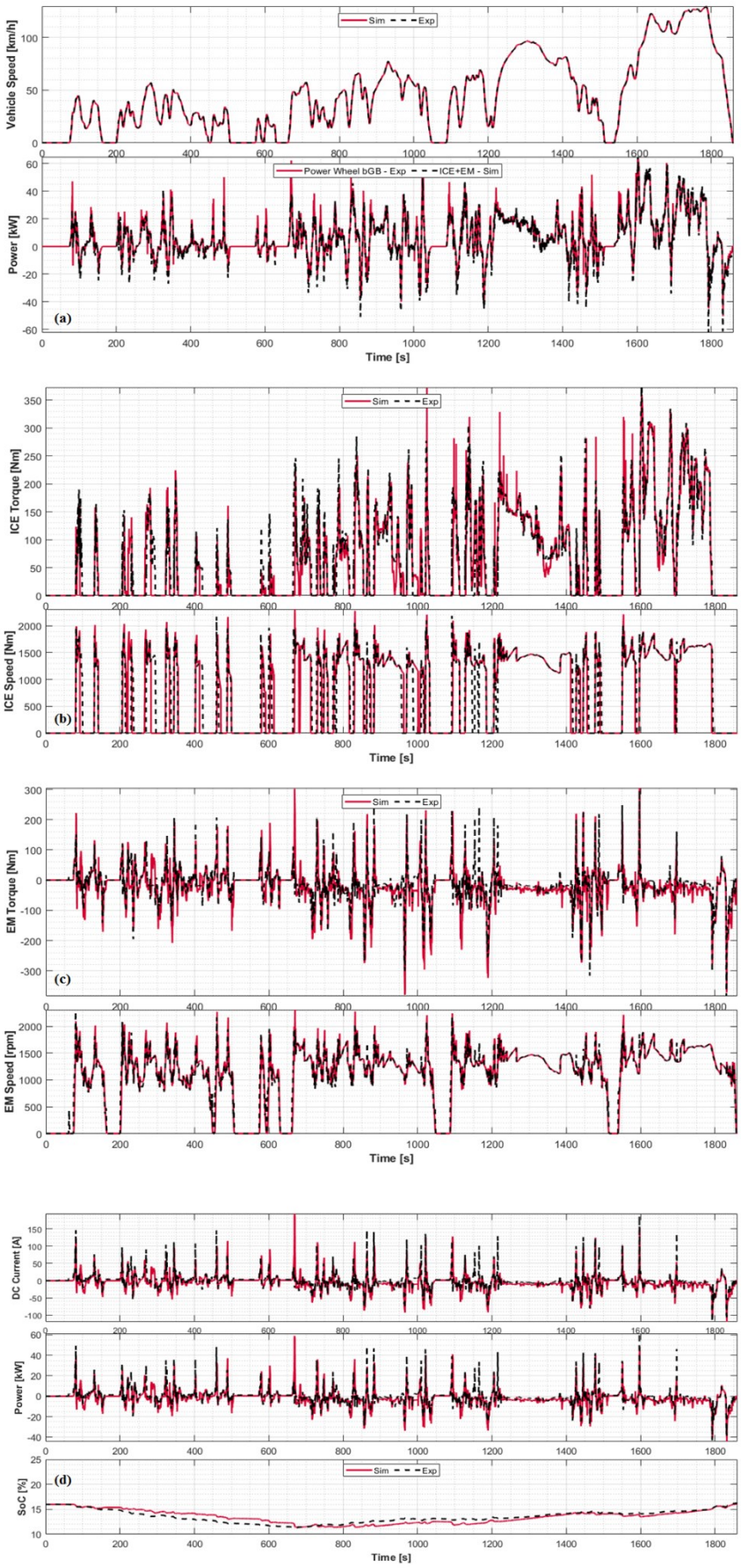


**Figure 96: Vehicle 3 - Experimental (black dashed) and simulated (red solid) results over the WLTC Charge Sustaining CS**

**CO2 EMISSIONS**

After the calibration of the EMS, the $CO_2$ emissions were evaluated over the two driving cycles, as already seen for Vehicle 1. In this regard, engine-out $CO_2$ produced was measured during the testing campaign on the chassis dyno; moreover, the fuel consumption map related to the Diesel engine were available. However, these maps were tuned in order to better fit the engine-out values with the same process introduced for Vehicle 1. As a result, the $CO_2$ flow rate maps shown in Figure 97 were adopted as a results of the fuel map conversion according to equation (4-2): the left side shows the $CO_2$ flow rate in cold conditions, hence with engine coolant temperature below 60°c, while the map on the left side shows the $CO_2$ flow rate in hot conditions.

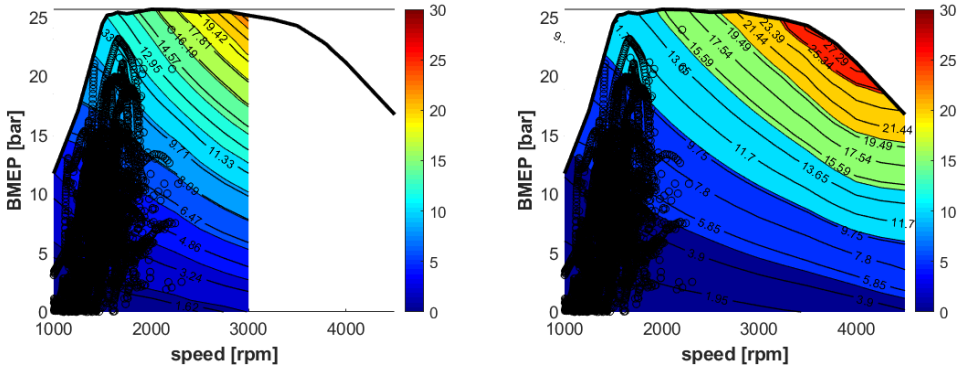


**Figure 97: Vehicle 3 $CO_2$ flow rate [g/s] calibrated cold (left) and hot (right) maps and WLTC ICE operating points (black)**

As one notice, the engine coolant temperature is relevant for $CO_2$ simulations, since it is used as a weight for interpolating between the two maps. Thus, the comparison between the simulated and experimental coolant temperature profiles is reported in Figure 98, showing the good predictive capabilities of the model both for a NEDC (left) and WLTC (right) simulation. These two pictures also show the simulated ICE block temperature (magenta solid line), which was not available on the experimental side. It can be noticed that for a cold-start cycle, the coolant temperature rises only after the block temperature has reached a value of around 50°C; this is due to the presence of a switchable water pump (see Figure 20) used to allow the coolant flowing after a cold-start. This feature was added to the engine thermal model in order to have a more accurate coolant simulation and $CO_2$ emission prediction.

Finally, the instantaneous and the cumulated $CO_2$ profiles are reported in Figure 99, for the NEDC (top) and WLTC (bottom) test cycles. The first sub-plot illustrates the instantaneous emissions and highlights the small overestimation during the cold portions (until 800s) of the NEDC, while the extra-urban driving portion is simulated more accurately. As shown in the second sub-plot, the cumulated CO2 mass has a good agreement with the experimental data, leading to an error of 4.2% or 6 g/km on the final value. As for the WLTC cycle, the instantaneous CO2 emissions are predicted accurately, both in the cold-start (until 80s) and in the warm phases. This results in a negligible underestimation of the

total amount of CO2 produced of about 2.3% or 3.6 g/km due to the engine load underestimation in some peak values in the first part of the cycle.

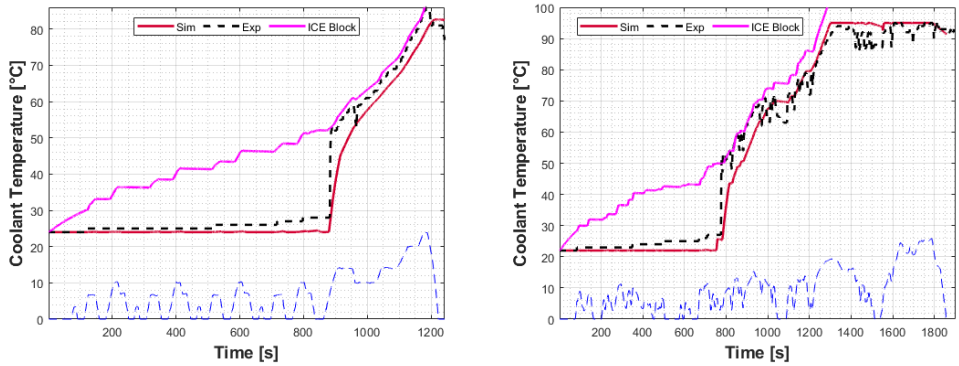


Figure 98: Vehicle 3 ICE block and coolant temperature profile along the NEDC (left) and WLTC (right) CS cycle

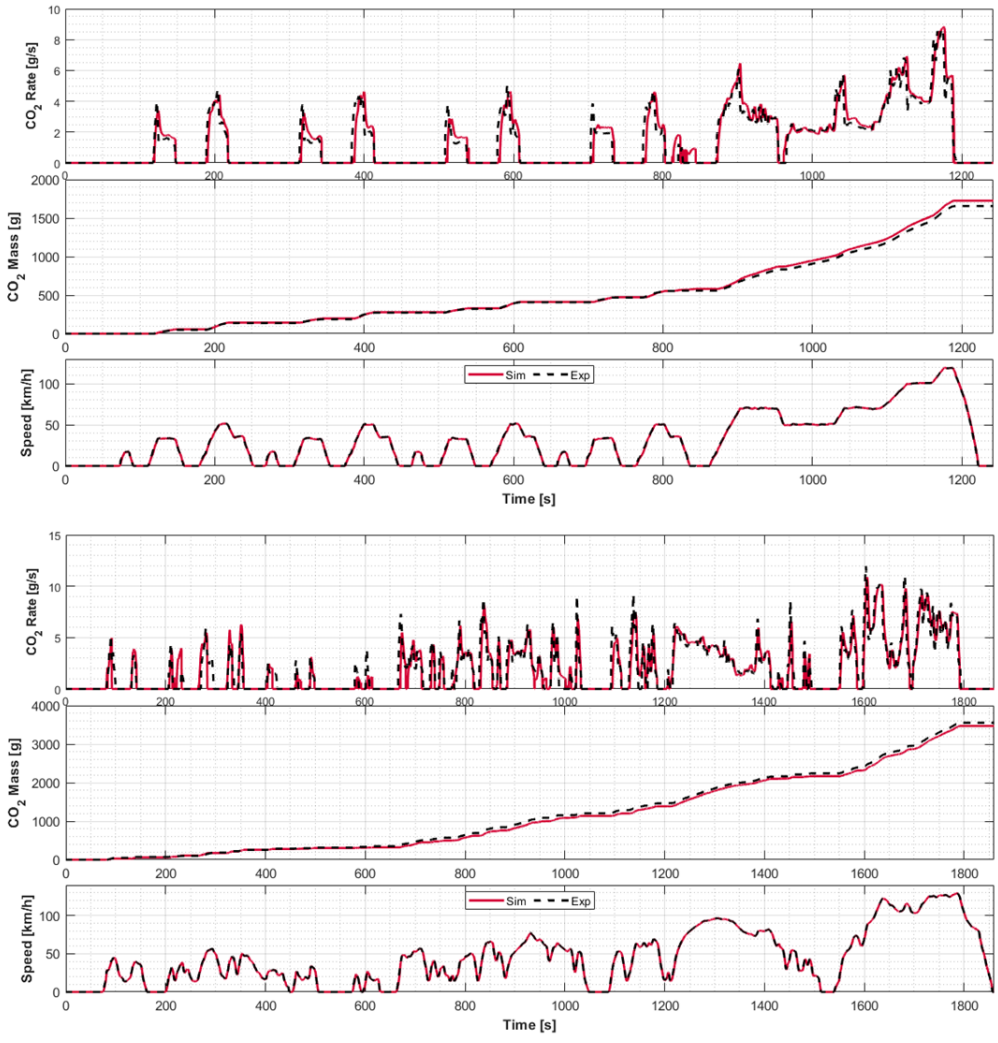


Figure 99: Vehicle 3 instantaneous and cumulated CO2 emissions over the NEDC (top) and WLTC (bottom) cycles

## 4.2 Model Validation

As a final assessment, the model predicting capabilities were evaluated over different driving scenarios, considering as test cases only Vehicle 2 and Vehicle 3 due to the higher powertrain complexity. As far as Vehicle 2 is concerned, the EMS model validation was carried out on a complete WLTC cycle in CS mode, while Vehicle 3 model validation was performed along the newly introduced RDE testing procedure, for the evaluation of both the torque split and $CO_2$ emissions, as already shown during model calibration.

### 4.2.1 Charge Sustaining WLTC

The model validation for Vehicle 2 was carried out along the WLTC cycle driven in CS mode, as reported in Figure 100. In this case, the power request is higher rather than on a NEDC, because of the higher mass and more aggressive speed profile. The total power requested at the clutch shows good agreement with the experimental data (top), meaning that the EM and the ICE torque are accurately simulated. The initial HV battery SOC was 14%, as illustrated in the second plot of Figure 100. Looking at the battery behavior, the DC current and the power well matches the measured data, both during charging and discharging phases. Transient phases are accurately predicted as well, even though a mismatch can be highlighted between 1200s and 1400s. To this extent, the difference in vehicle speed profile between simulation and experiments is due to the fact that a reference vehicle speed profile was chosen since the raw experimental profile was noisy signal. As a consequence, the speed gap results in a minor error in simulating current and power, thus the battery SOC is overestimated. However, the electrical quantities related to battery and the two electric machines are pretty well captured, although, the model is not able to fully simulate the transient phases because of its quasi-static nature. All things considered, the implemented EMS logics result in a good accuracy of the model in simulating the power split and the related electrical quantities.

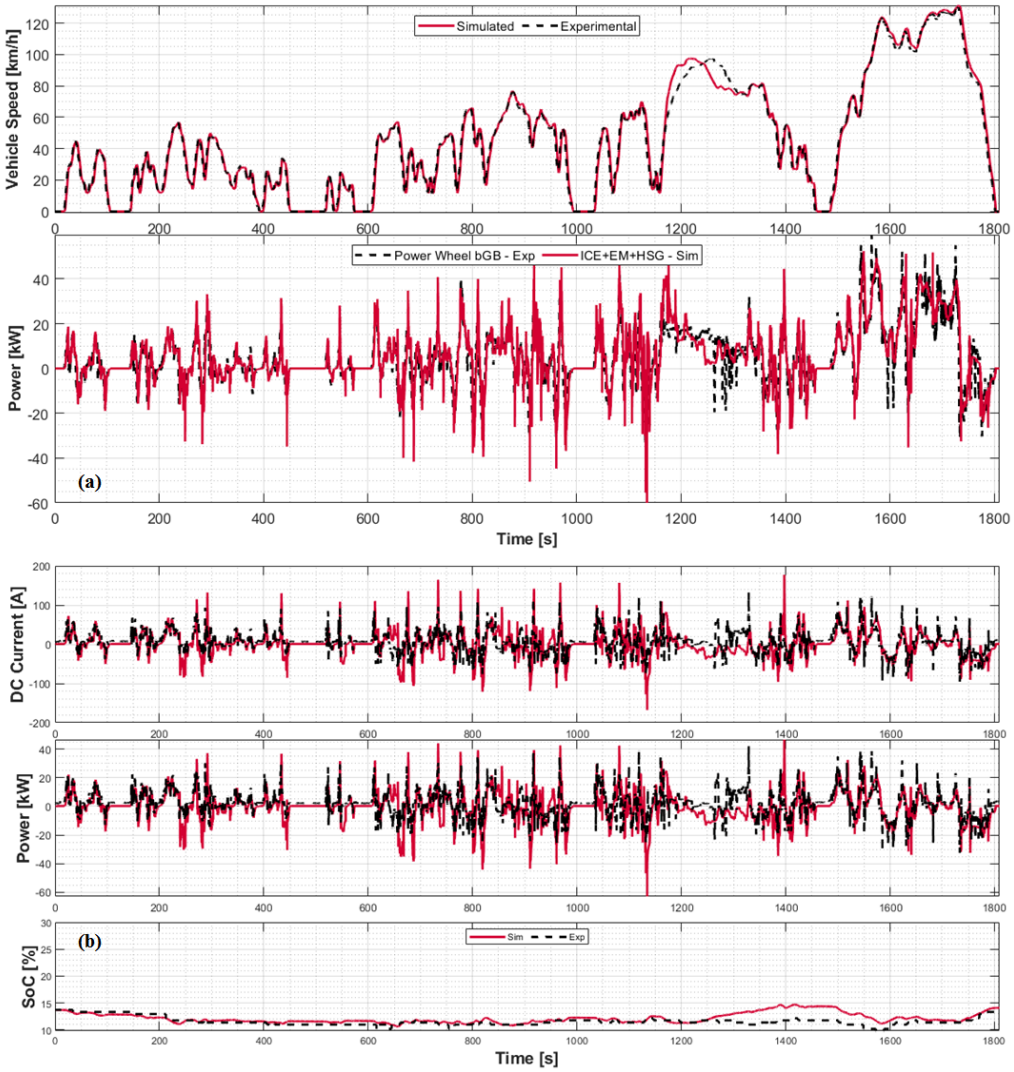


Figure 100: Vehicle 2 - Experimental (black dashed) and simulated (red solid) results over the WLTC Charge Sustaining CS

### 4.2.2 Real Driving Emissions Cycle

Finally, the model validation for Vehicle 3 was carried out along the RDE cycle with the aim of proving the predicting capabilities over a real-driving scenario. The driving mission used for vehicle simulation is the one depicted in Figure 28 , with a more aggressive and dynamic speed profile along with a change in altitude and road slope. All these information were used as input for vehicle simulation in order to account for the different torque request at the wheel due to the road gradient variation, and adjust the driver torque request accordingly. The results of cycle simulation have been divided into two parts (see Figure 101 and Figure 102) since the tests last almost two hours; moreover, the first part was carried out in pure electric mode (CD) while the second part was in hybrid mode (CS).

Figure 101 illustrates the first 3500s of the RDE cycle performed in EV mode, starting at 100% battery SOC. In this part, the maximum speed is below 100 km/h

and the total power requested at the clutch is in line with experimental data (a), hence, the EM operating points are well captured in terms of speed and load even though the cycle is highly transient (c). On the other side, the ICE was not used since the battery had enough energy content as depicted in sub-plot (b); as a consequence, the battery DC current and power show good agreement with the measured data, both during charging and discharging phases, resulting in an accurate estimation of the battery SOC profile shown in sub-plot(d).

The second part of the RDE cycle is shown in Figure 102: as already mentioned, this part of the cycle is performed in CS mode since the battery approximately consumes about 9.3kWh before turning on the ICE. As depicted in sub-plot (a), this part of the cycle is more power-demanding, reaching almost 90kWh in traction mode and maximum speed reached is about 130 km/h. Nevertheless, the power requested at the clutch is well predicted, especially in motor mode. As far as the torque split is concerned, the second sub-plot shows the engine operating torque and speed: the engine on request is controlled by the maps shown in the *Methodology* section and all the engine-on events are captured. It can be noticed that the model turns on the ICE more times than reality due to the highly transient and random nature of the RDE cycle. However, the trend of the torque and speed signals show a very good agreement with the experimental data. Likewise, the EM operating points are simulated with a good accuracy, except for the phases in which the ICE is on according to the model and so the EM is used to recover electric energy with negative absorbed torque. Finally, the simulated battery DC current and power well match the measured data, in charging and discharging the battery, giving a good estimation of the battery SOC also in CS mode, fluctuating around 13%.

To conclude with the RDE simulation, the $CO_2$ emissions were calculated over the real driving scenario, using the same maps reported in Figure 97. Due to the high initial battery SOC, only the second part of the cycle is responsible for $CO_2$ production since the ICE starts to work approximately in the middle of the rural phase. To this purpose, Figure 103 illustrates the instantaneous and the cumulated $CO_2$ simulated and experimental values collected over the RDE cycle. As already demonstrated for the ICE simulation, the model is capable of reproduction pretty well the instantaneous CO2 flow rate over the multiple engine-on events. However, the experimental $CO_2$ peaks are not fully captured together with the fact that the HCE model requires the ICE to be on few more times than reality. As a results, the total $CO_2$ produced is slightly over-estimated but the growing trend is well captured. This leads to an error of 3.1% or 2 g/km on the final cumulated value.

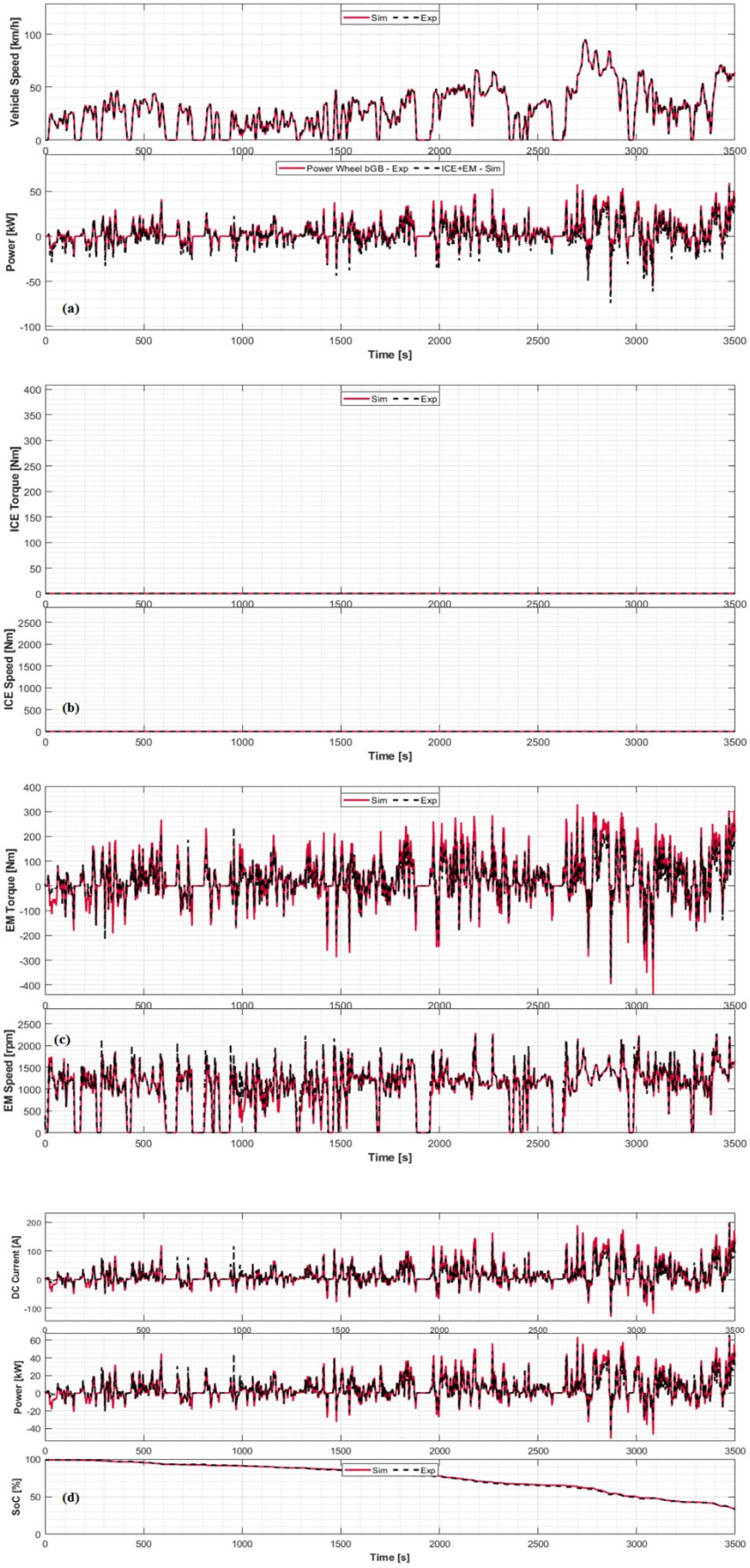


**Figure 101: Vehicle 3 - Experimental (black dashed) and simulated (red solid) results over the first part of RDE**

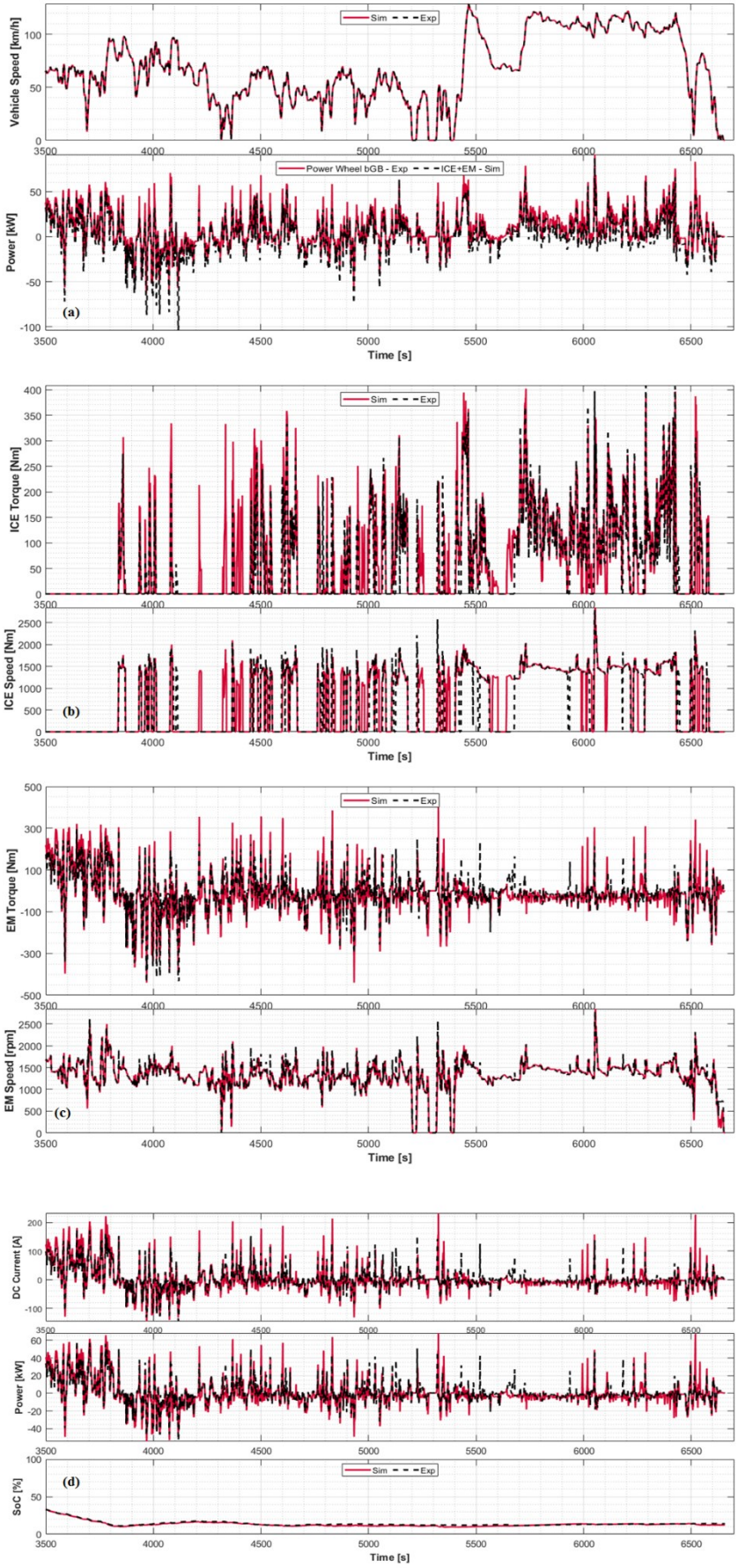


**Figure 102: Vehicle 3 - Experimental (black dashed) and simulated (red solid) results over the second part of RDE**

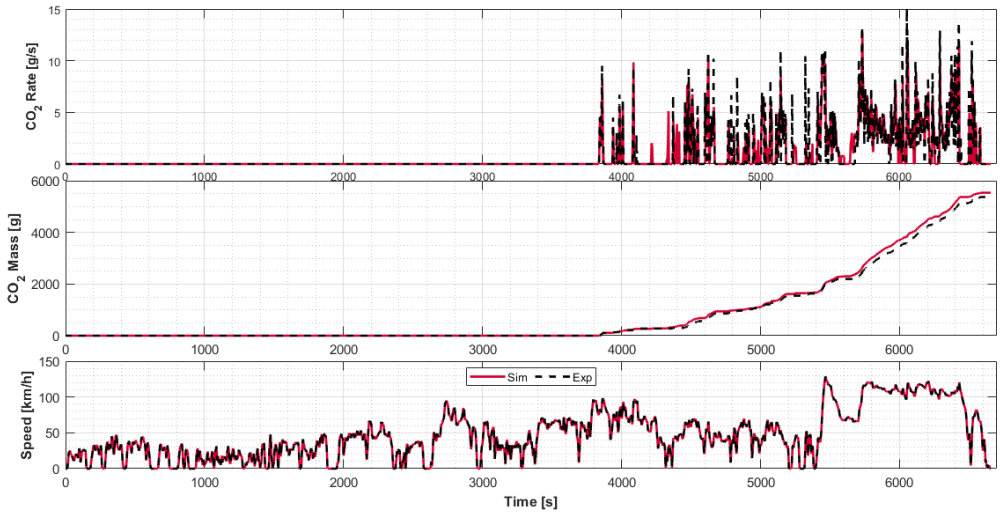


Figure 103: Vehicle 3 instantaneous and cumulated CO2 emissions over the RDE cycle

# Chapter 6

# Conclusions

Over the last two decades, the European Commission has been pushing towards policies for the protection of air quality and reduction of greenhouse gas emissions. In this scenario, powertrain electrification is believed to be one of the most relevant solution for OEMs in meeting both the mid-term and the long-term legislation targets. Regardless of the vehicle segment and volume, all the OEMs are continuously increasing the degree of electrification of their fleets.

In this framework, this research activity was developed to fill the gap between testing/benchmarking and simulation of different types of electrified vehicles. More in details, this work shows the quality in predicting the powertrain energy distribution, the vehicle behavior, as well as $CO_2$ and fuel consumption of various HEVs via a 0D map-based complete vehicle model. The proposed approach aims at providing a virtual test rig useful in the predevelopment phase of new automotive powertrains. The major issues have been handled with the proposed methodology, such as the intrusive and extensive experimental test campaign and the need of a tailored model according to the desired HEV topology. As a result, this research activity introduces an integrated approach between simulation and vehicle testing based on a simple and non-intrusive instrumentation and a reduced number of experimental tests. The limited amount of collected information are used to calibrate a Matlab/Simulink® model able to support various HEV architectures thanks to the separation of the control and the physical blocks.

As a starting point, three of the most representative hybrid electrified vehicles, were selected:

- a 48 V Mild-Hybrid (MHEV) P0 Diesel car, Euro 6 compliant, equipped with a six speed Manual Transmission (6-MT), hereafter referred to as Vehicle 1;

- a P0-P2 architecture gasoline Plug-in HEV, Euro 6 compliant, equipped with a six speed Dual-Clutch Transmission (6-DCT), hereafter referred to as Vehicle 2;
- a P2 architecture Diesel Plug-in HEV, Euro 6 compliant, equipped with a nine speed Automatic Transmission (9-AT), hereafter referred to as Vehicle 3.

Powertrain characterization was achieved with tests on the chassis-dyno and on the road. For the chassis dyno tests, measurements were performed following the TA procedure along the WLTP and NEDC cycles. Additionally, the Performance tests were used to investigate the powertrain behavior under medium-to-high power request, while the Critical Missions were adopted to emulate in real-life scenarios. In particular, test like standing-start acceleration, elasticity acceleration, constant speed driving, active braking, pedal release and sailing maneuvers were performed for powertrain characterization. Generally, these tests were carried out in the lab and on the road, according to the feasibility of the maneuver.

The characterization of Vehicle 1 was based on the experimental campaign useful to understand the P0 architecture behavior, via few experimental tests such as some on-road accelerations and elasticity tests and a NEDC and a WLTC. The instrumentation consisted in only five shunts sensors for electrical variables detection and in the use of an OBD scan tool to read signals from the vehicle communication system. It was found that the BSG is used as a support for the turbolag effect, in particular in the low speed – high load area to provide a quick response, reaching the maximum power with some restrictions above 40 km/h.

Vehicle 2 was characterized via the same experimental routine and with a NEDC performed on a chassis dyno. In this case, the higher energy available on board and the different architecture results in a more complex but accurate analysis of the capabilities of the P0-P2 topology. It was discovered that the P2 EM enable the EV mode over the entire speed range. An interesting finding is the map-characterization of the HEV mode request, via a threshold speed function of the torque requested at the wheels and of the battery SOC. To further investigate the EMS, the different driving modes were analyzed resulting in a frequent ICE operation during both the LPS and Boost mode, not only for vehicle start-up. Finally, the ICE power in Hybrid Mode was mapped showing a linear trend with vehicle speed for each gear, both in battery charging and in boosting.

Vehicle 3 represented the state of the art HEV in terms of powertrain technology; it was tested over a series of accelerations, constant driving and braking maneuvers. In addition, a repetition of NEDC and WLTC cycles in CD and CS mode was performed. As expected, the EM is widely used over the entire speed range for EV driving. On the EMS side, it was found that this vehicle operates in CD mode until the battery energy content is depleted and then switches to CS mode. Also in this case, the HEV mode request was characterized via a vehicle speed threshold and a power threshold. Moreover, the driving modes

were investigated showing that below 20 km/h only the EV drive and the regenerative braking are possible. For Vehicle 3, the ICE mainly works in LPS mode, while the boost mode is used for vehicle start-up. Finally, both the ICE and EM torque in LPS mode were analyzed, considering the different gears.

Later, the outcomes from the experimental campaign were used for the development of the comprehensive HEV model, which is intended to reproduce the logic of the EMS along the NEDC and WLTC driving cycles, after a calibration process. The simulations were performed for the three different test cases, both in CD and CS mode. As a result, the model shows good ability in identifying the power demand and its split between the ICE and the electric machines, along with an accurate prediction of the HV battery electrical flow which results in a reliable SOC estimation. Any discrepancy can be attributed to maps interpolation/extrapolation in transient phases. Additionally, for Vehicle 1 and Vehicle 3, it was possible to simulate the $CO_2$ emissions in a good agreement with the experimental data, with differences on the final value below 5%.

After this calibration process, the model was validated through simulation of the Vehicle 1 and Vehicle 3, on the WLTC and the RDE cycles. The WLTC for Vehicle 2 was performed at low battery SOC in order to assess the predictive capabilities of the model in matching the ICE-on events and the subsequent torque split regulation. In this case, an acceptable match between the powertrain behavior during both the propulsion and the charging phases was found. As for Vehicle 3, it was decided to test the skills of the model over a more complex and aggressive scenario such as the RDE driving cycle. Despite the fact that the model was calibrated based on the maps coming out of the experimental campaign, the model shows good predictive capabilities in both matching the torque split between the ICE and the EM and the battery behavior. To conclude, $CO_2$ emissions were simulated with a good accuracy, resulting in a 3% error on the final cumulated value.

The achieved results show that the integrated methodology provides reliable data that accurately represents the vehicle behavior and they can later be fitted into the 0D map-based model, which was built to be a valuable tool in vehicle virtual development. The author certainly believe that dealing with state-of-the-art hybrid technologies would benefit of measuring directly the AC 3-phase domain and this would represent a further step towards a complete experimental investigation. On the modeling side, the vehicle after-treatment system can be already implemented in the simulation platform if data coming from OEMs or suppliers are available, due to the complex nature of pollutants emissions simulation.

# References


1. International Transport Forum, “Is Low-Carbon Road Freight Possible?,” *Policy Br.*, 2018.
2. Live-Counter.com, “How Many Cars are There in the World?,” https://www.live-counter.com/number-of-cars/, doi:https://www.carsguide.com.au/car-advice/how-many-cars-are-there-in-the-world-70629.
3. International Transport Forum, “How to Make Urban Mobility Clean and Green,” 2018.
4. Tsakalidis, A. and Thiel, C., “Electric vehicles in Europe from 2010 to 2017: is full-scale commercialisation beginning?,” 2018, doi:10.2760/565748.
5. Directorate-General for Communication (European Commission), “A Resilient Energy Union with a Forward-looking Climate Change Policy,” (March), 2015, doi:10.1016/B978-0-12-802970-1.06001-0.
6. Commission, E., “CO2 emission standards for cars and vans,” https://www.consilium.europa.eu/en/press/press-releases/2019/01/16/co2-emission-standards-for-cars-and-vans-council-confirms-agreement-on-stricter-limits/.
7. Bolduc, D.A., Gibbs, N., Hetzner, C., Malan, A., and Sigal, P., “Automakers’ road maps to full-electric and plug-in hybrid cars,” https://europe.autonews.com/article/20181006/ANE/180929838/automakers-road-maps-to-full-electric-and-plug-in-hybrid-cars, 2018.
8. ICCT, “CO2 emissions from new passenger cars in the European Union: Car manufacturers’ performance in 2018,” 2018.
9. Mock, P., “CO2 Emission Standards for Passenger Cars and Light-Commercial Vehicles in the European Union,” *ICCT Policy Updat.* (January 2019):9, 2019.
10. Moultak, M., Lutsey, N., and Hall, D., “Transitioning to zero-emission heavy-duty freight vehicles,” *Int. Counc. Clean Transp.* (September), 2017.
11. Johnson, T. and Joshi, A., “Review of Vehicle Engine Efficiency and Emissions,” *SAE Tech. Pap.* 2017-March(March), 2017, doi:10.4271/2017-01-0907.
12. ICCT, “Chart library: Passenger vehicle fuel economy | International Council on Clean Transportation,” ISBN 964-7445-88-1, 2019.
13. ICCT, “Electric vehicles: Literature review of technology costs and carbon emissions,” (July):1–23, 2016, doi:10.13140/RG.2.1.2045.3364.
14. European Union, REGULATION (EC) No 443/2009 OF THE EUROPEAN PARLIAMENT AND OF THE COUNCIL of 23 April 2009 setting emission performance standards for new passenger cars as part of the Community’s integrated approach to reduce CO2 emissions from light-duty vehicles, *Off. J. Eur. Union* L140(05.06.2009):L140/1-L140/12, 2009.
15. Tsiakmakis, S., Fontaras, G., Anagnostopoulos, K., Ciuffo, B., and Marotta, A., “A simulation based approach for quantifying CO2 emissions of light duty vehicle fleets. A case study on WLTP introduction,” *Transp. Res. Procedia* 25:3902–3912, 2017, doi:10.1016/j.trpro.2017.05.308.
16. Duarte, G.O., Gonçalves, G.A., and Farias, T.L., “Analysis of fuel

consumption and pollutant emissions of regulated and alternative driving cycles based on real-world measurements," *Transp. Res. Part D Transp. Environ.* 44:43–54, 2016, doi:10.1016/j.trd.2016.02.009.
17. Zhang, P., Yan, F., and Du, C., "A comprehensive analysis of energy management strategies for hybrid electric vehicles based on bibliometrics," *Renew. Sustain. Energy Rev.* 48:88–104, 2015, doi:10.1016/j.rser.2015.03.093.
18. Reitz, R.D., "Grand Challenges in Engine and Automotive Engineering," *Front. Mech. Eng.* 1, 2015, doi:10.3389/fmech.2015.00001.
19. Galvagno, E., Velardocchia, M., and Vigliani, A., "Drivability enhancement and transient emission reduction for a mild hybrid diesel-electric truck," *Int. J. Powertrains* 2(2/3):262, 2013, doi:10.1504/ijpt.2013.054154.
20. Galvagno, E., Rondinelli, E., and Velardocchia, M., "Electro-Mechanical Transmission modelling for series-hybrid tracked tanks," *Int. J. Heavy Veh. Syst.* 19(3):256–280, 2012, doi:10.1504/IJHVS.2012.047916.
21. Galvagno, E., Vigliani, A., and Velardocchia, M., "Transient response and frequency domain analysis of an electrically variable transmission," *Adv. Mech. Eng.* 10(5), 2018, doi:10.1177/1687814018776182.
22. Galvagno, E., Morina, D., Sorniotti, A., and Velardocchia, M., "Drivability analysis of through-the-road-parallel hybrid vehicles," *Meccanica* 48(2):351–366, 2013, doi:10.1007/s11012-012-9606-6.
23. Tinelli, V., Galvagno, E., and Velardocchia, M., "Dynamic Analysis and Control of a Dual Mode Electrically Variable Transmission," *Mech. Mach. Sci.* 73:3731–3740, 2019, doi:10.1007/978-3-030-20131-9_368.
24. Axsen, J. and Kurani, K.S., "Hybrid, plug-in hybrid, or electric-What do car buyers want?," *Energy Policy* 61:532–543, 2013, doi:10.1016/j.enpol.2013.05.122.
25. Mock, P., "Auf der Zielgeraden. Die deutschen Automobilhersteller im Kontext der europäischen CO2-Vorgaben für 2021," 2019.
26. ICCT, "European vehicle market statistics - Pocketbook 2019/2020," 2019.
27. Gibbs, N., "EU electrified car push is driven by rules, not market demand," https://europe.autonews.com/article/20180922/ANE/180919747/eu-electrified-car-push-is-driven-by-rules-not-market-demand, 2018.
28. Koster, A., Kuhnert, F., and Stürmer, C., "Five trends transforming the Automotive Industry," 2018.
29. SCHAEFFLER, "Fact sheet XXL: Schaeffler symposium 2018 mobility for tomorrow," *Schaeffler*, 1–9, 2018.
30. ICCT, "European Vehicle Market Statistics - Pocketbook 2018/19," 64, 2018.
31. Hui, Z., Dongpu, C., and Haiping, D., "Modeling, Dynamics and Control of Electrified Vehicles," ISBN 978-0-12-812786-5, 2018, doi:10.1016/C2016-0-03862-7.
32. Emissions Analytics, "Hybrids are 14 times better than battery electric vehicles at reducing real-world carbon dioxide emissions," https://www.emissionsanalytics.com/news/hybrids-are-better, 2019.
33. Senecal, P.K. and Leach, F., "Diversity in transportation: Why a mix of propulsion technologies is the way forward for the future fleet," *Results Eng.* 4, 2019, doi:10.1016/j.rineng.2019.100060.
34. Singh, K.V., Bansal, H.O., and Singh, D., "A comprehensive review on hybrid electric vehicles: architectures and components," *J. Mod. Transp.*

27(2):77–107, 2019, doi:10.1007/s40534-019-0184-3.
35. Zanelli, A., Millo, F., and Barbolini, M., “Driving cycle and elasticity manoeuvres simulation of a small SUV featuring an electrically boosted 1.0 L gasoline engine,” *SAE Tech. Pap.* 2020:1–16, 2020, doi:10.4271/2019-24-0070.
36. Accurso, F., Zanelli, A., Rolando, L., and Millo, F., “Real Time Energy Management Control Strategies for an Electrically Supercharged Gasoline Hybrid Vehicle,” *SAE Tech. Pap.* 2020-April(April), 2020, doi:10.4271/2020-01-1009.
37. Zhang, Y., Miyakawa, S., Kasai, K., Okada-Shudo, Y., and Watanabe, M., “Efficient phase noise suppression of an external-cavity diode-laser by optical filtering and resonant optical feedback,” *Appl. Phys. B Lasers Opt.* 108(1):39–42, 2012, doi:10.1007/s00340-012-4918-8.
38. Khayyam, H. and Bab-Hadiashar, A., “Adaptive intelligent energy management system of plug-in hybrid electric vehicle,” *Energy* 69:319–335, 2014, doi:10.1016/j.energy.2014.03.020.
39. Zhang, S. and Xiong, R., “Adaptive energy management of a plug-in hybrid electric vehicle based on driving pattern recognition and dynamic programming,” *Appl. Energy* 155:68–78, 2015, doi:10.1016/j.apenergy.2015.06.003.
40. Cubito, C., Rolando, L., Millo, F., Ciuffo, B., Serra, S., Trentadue, G., Garcia Otura, M., and Fontaras, G., “Energy Management Analysis under Different Operating Modes for a Euro-6 Plug-in Hybrid Passenger Car,” *SAE Int.* 2017-March(March), 2017, doi:10.4271/2017-01-1160.
41. Kelly, J., Scanes, P., and Bloore, P., “Specification and design of a switched reluctance 48 v belt integrated starter generator (B-ISG) for mild hybrid passenger car applications,” *SAE Tech. Pap.* 1, 2014, doi:10.4271/2014-01-1890.
42. Vallur, A.R., Khairate, Y., and Awate, C., “Prescriptive Modeling , Simulation and Performance Analysis of Mild Hybrid Vehicle and Component Optimization Mild Hybrid System- Improvement of Fuel,” *SAE Int.*, 2015, doi:10.4271/2015-26-0010.Copyright.
43. Barel, G. Van, Huybrechts, T., Vanommeslaeghe, Y., Blontrock, D., and Hellinckx, P., “Automatic Reverse Engineering of CAN BusData Using Machine Learning Techniques,” 2017, doi:10.1007/978-3-319-69835-9_71.
44. Ripaccioli, G., Bemporad, A., Assadian, F., Dextreit, C., Cairano, S. Di, and Kolmanovsky, I. V., “Hybrid modeling, identification, and predictive control: An application to hybrid electric vehicle energy management,” *Lect. Notes Comput. Sci. (Including Subser. Lect. Notes Artif. Intell. Lect. Notes Bioinformatics)* 5469:321–335, 2009, doi:10.1007/978-3-642-00602-9_23.
45. Cardoso, D.S., Fael, P.O., and Espírito-Santo, A., “A review of micro and mild hybrid systems,” *Energy Reports*, 2019, doi:10.1016/j.egyr.2019.08.077.
46. A Comprehensive System Approach for Future Powertrain Electrification, *CTI Mag.*, 2018.
47. Synopsis, “Hybrid and Electric Vehicle Design,” 2019.
48. M.T.M. s.r.l. - Gas Equipment, “4WD Clima - Annex 1 Technical Addendum,” 2019.
49. Horiba, “VULCAN_Brochure_ENG,” ISBN 9788578110796, 2018, doi:10.1017/CBO9781107415324.004.

50. Millo, F., Engine Emissions Control - Lesson notes of Automotive Engineering course, 2015.
51. Horiba, “CVS-ONE_Brochure_English,” 2018.
52. Isabellenhütte Heusler GmbH & Co., “ISAscale® // High precision measurement,” 2015.
53. LEM Europe GmbH, “LEM - Product Catalogue,” https://www.lem.com/sites/default/files/products_datasheets/htr_50_500-sb.pdf.
54. EI Sensor Technologies, “No What is a Thermistor?,” https://www.ei-sensor.com/what-is-a-thermistor/, 2019.
55. Council of the European Union, “DIRECTIVE 98/70/EC OF THE EUROPEAN PARLIAMENT AND OF THE COUNCIL of 13 October 1998 relating,” *Off. J. Eur. Communities* (350):58–67, 1998.
56. ETAS, “ODX-LINK V7.2 ODX-FLASH V7.2 - User’s Guide,” 2019.
57. Posada, F. and German, J., “Review of Ldv Obd Requirements Under the European , Korean and Californian Emission Programs,” 2016.
58. International, S., “Diagnostic Connector Equivalent to ISO/DIS 15031-3: December 14, 2001,” doi:https://doi.org/10.4271/J1962_201207.
59. Wikipedia, “On-board diagnostics,” https://en.wikipedia.org/wiki/On-board_diagnostics#cite_note-2, Mar. 2020.
60. Corrigan, S., “Introduction to the controller area network (CAN),” *Appl. Report, Texas Instruments* (August 2002):1–15, 2002.
61. National Instruments, “FlexRay Automotive Communication Bus Overview,” 1–7, http://www.ni.com/white-paper/3352/en/, 2009.
62. Dipierro, G., Millo, F., Galvagno, E., Velardocchia, M., Mari, G., and Perazzo, A., “A Reverse Engineering Method for Powertrain Parameters Characterization Applied to a P2 Plug-In Hybrid Electric Vehicle with Automatic Transmission,” *SAE Tech. Pap.*, 2020.
63. Biondi, F.C., “Development of an integrated methodology for the experimental and numerical characterization of an automatic transmission with torque converter for a Plug-in hybrid vehicle,” Politecnico di Torino, 2020.
64. ETAS, “ETAS INCA v7.2 Product Page,” https://www.etas.com/en/products/inca_software_products-functions_v72_service_pack_13.php, 2019.
65. United Nations, Addendum 15 : Global technical regulation No . 15 - Worldwide harmonized Light vehicles Test Procedure, *Glob. Regist.* ECE/TRANS/:1–234, 2014.
66. UNECE, Regulation No. 101 Uniform provisions concerning the approval of passenger cars powered by an internal combustion engine only, or powered by a hybrid electric power train with regard to the measurement of the emission of carbon dioxide and fuel consumptio, 2013.
67. Cubito, C., “A policy-oriented vehicle simulation approach for estimating the CO2 emissions from Hybrid Light Duty Vehicles,” Politecnico di Torino, 2017.
68. Dipierro, G., Millo, F., Cubito, C., Ciuffo, B., and Fontaras, G., “Analysis of the Impact of the WLTP Procedure on CO2 Emissions of Passenger Cars,” *SAE Tech. Pap.* (October), 2019, doi:10.4271/2019-24-0240.
69. Dieselnet, “Worldwide Harmonized Light Vehicles Test Procedure (WLTP),” https://www.dieselnet.com/standards/cycles/wltp.php, 2016.
70. Commission Regulation (EU) 2016/646, “COMMISSION REGULATION

(EU) 2016/646 of 20 April 2016 amending Regulation (EC) No 692/2008 as regards emissions from light passenger and commercial vehicles (Euro 6)," *Off. J. Eur. Union* (L 109/1):1–22, 2016, doi:http://eur-lex.europa.eu/pri/en/oj/dat/2003/l_285/l_28520031101en00330037.pdf.
71. EU, "COMMISSION REGULATION (EU) 2016/427 of 10 March 2016 amending Regulation (EC) No 692/2008 as regards emissions from light passenger and commercial vehicles (Euro 6)," *Off. J. Eur. Union* II(May):20–30, 2016, doi:http://eur-lex.europa.eu/pri/en/oj/dat/2003/l_285/l_28520031101en00330037.pdf.
72. 2017/1151, C.R. (EU) N., "Commission Regulation (EU) 2017/1151 of 7 June 2017 supplementing Regulation (EC) No 715/2007 of the European Parliament and of the Council on type-approval of motor vehicles with respect to emissions from light passenger and commercial vehicles (Euro 5 a," *Off. J. Eur. Union* (692):1–643, 2017.
73. European Commission, "Regulation (EU) 2018/1832 of 5 November 2018 amending Directive 2007/46/EC of the European Parliament and of the Council, Commission Regulation (EC) No 692/2008 and Commission Regulation (EU) 2017/1151," *Off. J. Eur. Union* 1832(692):301, 2018.
74. AECC, "A NEW ERA FOR VEHICLE EMISSIONS CONTROL STARTS TODAY," 2017.
75. Concawe, "Recent studies on real driving emissions of diesel passenger cars," 2017.
76. Dipierro, G., Millo, F., Scassa, M., and Perazzo, A., "An Integrated Methodology for 0D Map-Based Powertrain Modelling Applied to a 48 V Mild-Hybrid Diesel Passenger Car," *SAE Tech. Pap.* 1–15, 2018, doi:10.4271/2018-01-1659.
77. ICCT, "Hybrid Vehicles Technology Development and Cost Reduction."
78. Dipierro, G., Tansini, A., Fontaras, G., and Commission, E., "An Integrated Experimental and Numerical Methodology for Plug-In Hybrid Electric Vehicle 0D Modelling," *SAE Tech. Pap.*, 2019, doi:10.4271/2019-24-0072.Abstract.
79. Chang, W.-Y., "The State of Charge Estimating Methods for Battery: A Review," *ISRN Appl. Math.* 2013:1–7, 2013, doi:10.1155/2013/953792.
80. Ng, K.S., Moo, C.S., Chen, Y.P., and Hsieh, Y.C., "Enhanced coulomb counting method for estimating state-of-charge and state-of-health of lithium-ion batteries," *Appl. Energy* 86(9):1506–1511, 2009, doi:10.1016/j.apenergy.2008.11.021.
81. Oracle, "Why TimetoMarket is More Critical Than Ever for Today's Automotive Supplier."
82. Bringmann, E. and Krämer, A., "Model-based Testing of Automotive Systems," *International Conference on Software Testing, Verification, and Validation*, 2008.
83. Ravet, F., "Crucial needs for efficient simulations in automotive industry," 2019.
84. Serrao, L., Onori, S., and Rizzoni, G., "A comparative analysis of energy management strategies for hybrid electric vehicles," *J. Dyn. Syst. Meas. Control. Trans. ASME* 133(3), 2011, doi:10.1115/1.4003267.
85. Guzzella, L. and Sciarretta, A., "Vehicle propulsion systems: Introduction to modeling and optimization," *Veh. Propuls. Syst. Introd. to Model. Optim.* 9783642359:1–409, 2013, doi:10.1007/978-3-642-35913-2.
86. Morel, T., Keribar, R., and Leonard, A., "'Virtual

Engine/Powertrain/Vehicle' Simulation Tool Solves Complex Interacting System Issues," *SAE Tech. Pap.*, 2003, doi:10.4271/2003-01-0372.
87. Gamma-Technologies, GT-Suite User Manual, 2015.
88. Millo, F., Rolando, L., and Andreata, M., "Numerical Simulation for Vehicle Powertrain Development," *Numerical Analysis - Theory and Application*, ISBN 978-953-307-389-7: 519–540, 2011, doi:10.5772/24111.
89. Vassallo, A., Cipolla, G., Mallamo, F., Paladini, V., Millo, F., and Mafrici, G., "Transient Correction of Diesel Engine Steady-State Emissions and Fuel Consumption Maps for Vehicle Performance Simulation," *Aachener Kolloquium Fahrzeug Und Mot.*, 2007.
90. Pettiti, M., Pilo, L., and Millo, F., "Development of a new mean value model for the analysis of turbolag phenomena in automotive diesel engines," *SAE Tech. Pap.*, 2007, doi:10.4271/2007-01-1301.
91. Firsching, P., Eckl, T., Rauch, M., Rohe, M., and Kohlhoff, J., "48-Volt-Hybridisation of the Drive Train," *25. Aachener Kolloquium Fahrzeug-Und Mot. 2016* 211–228, 2016.
92. Finesso, R., Spessa, E., and Venditti, M., "Cost-optimized design of a dual-mode diesel parallel hybrid electric vehicle for several driving missions and market scenarios," *Appl. Energy* 177:366–383, 2016, doi:10.1016/j.apenergy.2016.05.080.
93. Finesso, R., Spessa, E., and Venditti, M., "Layout design and energetic analysis of a complex diesel parallel hybrid electric vehicle," *Appl. Energy* 134, 2014, doi:10.1016/j.apenergy.2014.08.007.
94. Grondin, O., Thibault, L., and Quérel, C., "Energy Management Strategies for Diesel Hybrid Electric Vehicle," *Oil Gas Sci. Technol.* 70(1):125–141, 2015, doi:10.2516/ogst/2013215.
95. MILLO, F., ROLANDO, L., FUSO, R., and MALLAMO, F., "Real CO2 emissions benefits and end user's operating costs of a plug-in Hybrid Electric Vehicle," *Appl. Energy* 114:563–571, 2014, doi:10.1016/j.apenergy.2013.09.014.
96. UNECE, "Regulation No. 83: Uniform provisions concerning the approval of vehicles with regard to the emission of pollutants according to engine fuel requirements," 2011.
97. Gonçalo Viseu Vieira Sarrico, J., José da Costa Branco João Filipe Pereira Fernandes, P., Manuel Gameiro de Castro Supervisor, R., and José da Costa Branco, P., "Design and Implementation of a 20 kW, 12000 RPM Permanent Magnet Synchronous Motor (PMSM) for the IST Formula Student Powertrain Electrical and Computer Engineering Examination Committee," Instituto Superior Técnico Lisboa, 2017.
98. Chapman, P.L., "Permanent-magnet synchronous machine drives," *Power Electron. Handb. Ind. Electron. Ser.* 12-1-12–10, 2001, doi:10.1002/9781119260479.ch9.
99. Eriksson, S., "Permanent magnet synchronous machines," 2019, doi:10.3390/en12142830.
100. Chin, Y.K. and Soulard, J., "A permanent magnet synchronous motor for traction applications of electric vehicles," *IEMDC 2003 - IEEE Int. Electr. Mach. Drives Conf.* 2:1035–1041, 2003, doi:10.1109/IEMDC.2003.1210362.
101. Zhang, C., Jiang, J., Zhang, L., Liu, S., Wang, L., and Loh, P.C., "A generalized SOC-OCV model for lithium-ion batteries and the SOC estimation for LNMCO battery," *Energies* 9(11), 2016,

doi:10.3390/en9110900.
102. Kim, B.G., Patel, D.D., and Salameh, Z.M., "Circuit Model of 100 Ah Lithium Polymer Battery Cell," *J. Power Energy Eng.* 01(06):1–8, 2013, doi:10.4236/jpee.2013.16001.
103. Samad, N.A., Siegel, J.B., and Stefanopoulou, A.G., "Parameterization and validation of a distributed coupled electro-thermal model for prismatic cells," *ASME 2014 Dyn. Syst. Control Conf. DSCC 2014* 2, 2014, doi:10.1115/DSCC2014-6321.
104. Samad, N.A., Kim, Y., Siegel, J.B., and Stefanopoulou, A.G., "Influence of Battery Downsizing and SOC Operating Window on Battery Pack Performance in a Hybrid Electric Vehicle," *2015 IEEE Veh. Power Propuls. Conf. VPPC 2015 - Proc.*, 2015, doi:10.1109/VPPC.2015.7352966.
105. Cleary, T., Kunte, H., and Kreibick, J., "Electrical and Thermal Modeling of a Large-Format Lithium Titanate Oxide Battery System | MNTRC," 2015, doi:10.13140/RG.2.1.4182.3126.